

**STRUCTURE AND MAGNETIC PROPERTIES OF CeO_2
AND $\text{Ce}_{1-x}\text{TM}_x\text{O}_2$ (TM = Mn AND Co)
NANOSTRUCTURES PREPARED BY EGG-WHITE
SOLUTION ROUTE**



Panwit Sangkhaoartyon

A Thesis Submitted in Partial Fulfillment of the Requirements for the

Degree of Master of Science in Physics

Suranaree University of Technology

Academic Year 2017

โครงสร้างและสมบัติทางแม่เหล็กของ CeO_2 และ $\text{Ce}_{1-x}\text{TM}_x\text{O}_2$ (TM = Mn
และ Co) โครงสร้างนาโนที่เตรียมโดยวิธีสารละลายจากไข่ขาว

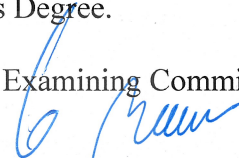


วิทยานิพนธ์นี้เป็นส่วนหนึ่งของการศึกษาตามหลักสูตรปริญญาวิทยาศาสตรมหาบัณฑิต
สาขาวิชาฟิสิกส์
มหาวิทยาลัยเทคโนโลยีสุรนารี
ปีการศึกษา 2560

**STRUCTURE AND MAGNETIC PROPERTIES OF CeO₂ AND
Ce_{1-x}TM_xO₂ (TM = Mn AND Co) NANOSTRUCTURES PREPARED
BY EGG-WHITE SOLUTION ROUTE**

Suranaree University of Technology has approved this thesis submitted in partial fulfillment of the requirements for a Master's Degree.

Thesis Examining Committee



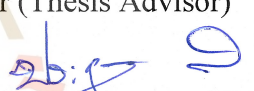
(Assoc. Prof. Dr. Worawat Meevasana)

Chairperson



(Prof. Dr. Santi Maensiri)

Member (Thesis Advisor)



(Assoc. Prof. Dr. Prayoon Songsiriritthigul)


Member



(Assoc. Prof. Dr. Chatchai Jothityangkoon)

Vice Rector for Academic Affairs

and Quality Assurance



(Prof. Dr. Santi Maensiri)

Dean of Institute of Science

ปริญญ์ แสงขาวอาทิวร : โครงสร้างและสมบัติทางแม่เหล็กของ CeO_2 และ $\text{Ce}_{1-x}\text{TM}_x\text{O}_2$ (TM = Mn และ Co) โครงสร้างนาโนที่เตรียมโดยวิธีสารละลายจากไข่ขาว (STRUCTURE AND MAGNETIC PROPERTIES OF CeO_2 AND $\text{Ce}_{1-x}\text{TM}_x\text{O}_2$ (TM = Mn AND Co) NANOSTRUCTURES PREPARED BY EGG-WHITE SOLUTION ROUTE)

อาจารย์ที่ปรึกษา : ศาสตราจารย์ ดร.สันติ แม่นศิริ, 88 หน้า.

วิทยานิพนธ์นี้มุ่งศึกษาโครงสร้างนาโนและคุณสมบัติแม่เหล็กของ CeO_2 และ $\text{Ce}_{1-x}\text{TM}_x\text{O}_2$ (TM = Mn, Co) เตรียมโดยวิธีสารละลายจากไข่ขาว แคลไซน์ที่อุณหภูมิ 500 600 และ 700 องศาเซลเซียส เป็นเวลา 2 ชั่วโมง ตัวอย่างถูกตรวจสอบโครงสร้างและสัณฐานวิทยา โดยใช้เทคนิค X-ray diffraction (XRD), transmission electron microscopy (TEM), scanning electron microscopy (SEM) และ UV-visible spectroscopy (UV-vis) ศึกษาสถานะประจุของ Ce Mn และ Co โดยใช้เทคนิค X-ray absorption near-edge structure spectroscopy (XANES) จากนั้นศึกษาคุณสมบัติทางแม่เหล็กของอนุภาคนาโนด้วยเทคนิค vibrating sample magnetometry (VSM) ผลการศึกษาโครงสร้างและลักษณะของอนุภาคนาโน CeO_2 และ $\text{Ce}_{1-x}\text{TM}_x\text{O}_2$ พบว่า มีโครงสร้างผลึกแบบลูกบาศก์ของสารประกอบออกไซด์ของ CeO_2 และพบเฟสเจือปนในโครงสร้างประกอบด้วย Mn_3O_4 MnO_2 Co_3O_4 และ $\text{Co}(\text{NO}_3)_2$ จากการคำนวณขนาดของผลึกโดยใช้สมการของ Scherrer พบว่าขนาดผลึกเฉลี่ยอยู่ในช่วง 10.0 ± 3.2 ถึง 35.4 ± 2.8 นาโนเมตร และตัวอย่างมีลักษณะเป็นเม็ดทรงกลมเกาะกันเป็นแผ่นบาง ขนาดของอนุภาคเฉลี่ยประมาณ 5 - 60 นาโนเมตร จากการศึกษาด้วยเทคนิค UV-Vis พบว่าอนุภาคที่เตรียมได้แสดงพฤติกรรม red shift โดยมีสาเหตุมาจากการเจือของโลหะทรานซิชัน (TM) และจากการศึกษา สถานะประจุขององค์ประกอบของตัวอย่างพบว่าเป็นทั้ง Ce^{3+} Ce^{4+} Mn^{2+} Mn^{3+} Mn^{4+} Co^{2+} และ Co^{3+} เมื่อศึกษาสมบัติแม่เหล็กของอนุภาคนาโนของตัวอย่าง พบว่า ตัวอย่าง CeO_2 แสดงสมบัติแม่เหล็กแบบไดอา และตัวอย่าง CeO_2 เจือ Mn แสดงสมบัติแม่เหล็กแบบเฟอร์โรและแบบพารา โดยมีค่าแมกเนไทน์เซชัน (M) เพิ่มขึ้นตามค่า x ซึ่งค่า M สูงสุดเท่ากับ 0.00035 emu/g สำหรับตัวอย่าง CeO_2 เจือ Co ที่ $x = 0.05$ และ 0.10 แสดงสมบัติแม่เหล็กแบบไดอา ขณะที่ $x = 0.075$ แสดงสมบัติแม่เหล็กแบบเฟอร์โรและแบบพารา โดยค่า M เท่ากับ 0.00015 emu/g จากการศึกษาพบว่าความเป็นแม่เหล็กแบบเฟอร์โรของ CeO_2 ที่เจือด้วยโลหะ

ทรานซิสชัน เกิดจากหลายสาเหตุ เช่น ผลของการเจือ การฟอร์มโครงสร้างแม่เหล็กของสาร และรวมไปถึงการเกิดช่องว่างของออกซิเจน ซึ่งเป็นตัวกลางของการเกิดอันตรกิริยาการแลกเปลี่ยนประจุของไอออน นอกจากนี้ผลของสถานะประจุไอออนที่มีความเป็นแม่เหล็ก (Mn และ Co) ยังมีบทบาทที่สำคัญในการแสดงพฤติกรรมแบบเฟอร์โรของสารกลุ่มนี้ด้วย



สาขาวิชาฟิสิกส์
ปีการศึกษา 2560

ลายมือชื่อนักศึกษา

ป. งาม

ลายมือชื่ออาจารย์ที่ปรึกษา

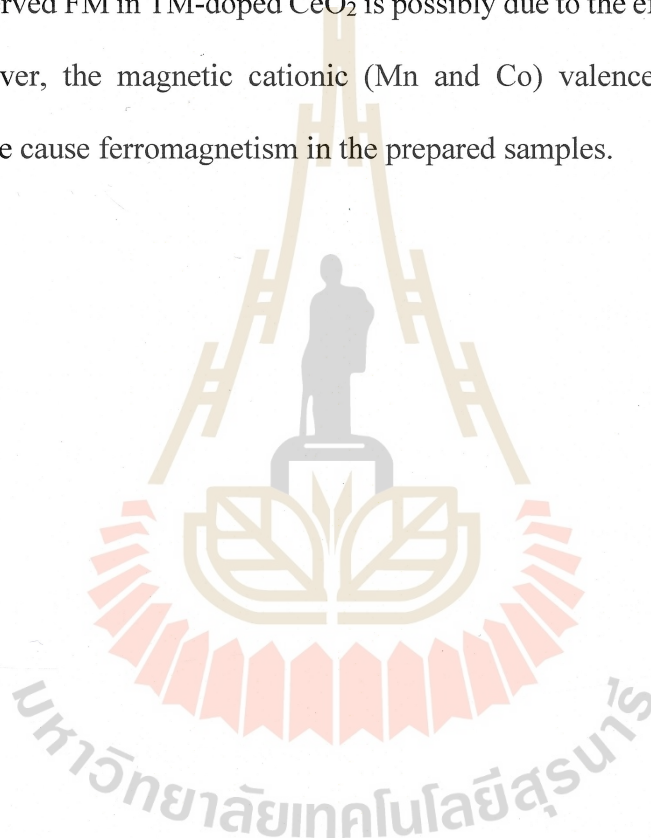
ป. งาม

PANWIT SANGKHAOARTYON : STRUCTURE AND MAGNETIC
PROPERTIES OF CeO₂ AND Ce_{1-x}TM_xO₂ (TM = Mn AND Co)
NANOSTRUCTURES PREPARED BY EGG-WHITE SOLUTION ROUTE.
THESIS ADVISOR : PROF. SANTI MAENSIRI, D. Phil. 88 PP.

CeO₂/EGG-WHITE SOLUTION/DILUTE MAGNETIC OXIDES/
FERROMAGNETISM/OXYGEN VACANCIES

This study reports the structure and magnetic properties of CeO₂ and Ce_{1-x}TM_xO₂ (TM = Mn and Co) nanostructures prepared by egg-white solution route. These samples were calcined at 500, 600 and 700 °C for 2h to obtain TM-doped CeO₂ nanoparticles. The prepared samples were studied using X-ray diffraction (XRD), transmission electron microscopy (TEM), scanning electron microscopy (SEM) and UV-visible spectroscopy (UV-vis). The valence states of Ce, Mn and Co ions in Ce_{1-x}TM_xO₂ structure were determined by using X-ray absorption near edge structure spectroscopy (XANES). The magnetic properties of the samples were studied using vibrating sample magnetometry (VSM). The XRD results indicated that all samples have a cubic structure with impurity phases consisting of Mn₃O₄, MnO₂, Co₃O₄ and Co(NO₃)₂. The average crystallite sizes of the samples calculated by Scherrer's formula were found to be in the range of 10 ± 3.2 to 35.4 ± 2.8 nm. The morphology of the samples consists of thin platelike clusters of networked nanoparticles and average particles size of ~ 5 - 60 nm UV-vis spectra showed a redshift of the band gap energy due to TM substitution. The valence state of TM ions were in the Ce⁴⁺, Ce³⁺, Mn²⁺, Mn³⁺, Mn⁴⁺, Co²⁺ and Co³⁺. The CeO₂ samples exhibited diamagnetism. The Mn-doped

CeO₂ samples showed ferromagnetism (FM) and paramagnetic component at room temperature (RT). The magnetization values (M) of samples increased with increasing Mn content, having the highest M values of 0.00035 emu/g. The Co-doped CeO₂ with Co contents of 0.05 and 0.10 samples exhibited diamagnetism, whereas Co-doped CeO₂ with Co content of 0.075 showed FM and paramagnetic with M of 0.00015 emu/g at RT. The observed FM in TM-doped CeO₂ is possibly due to the effect oxygen vacancies (V_o). Moreover, the magnetic cationic (Mn and Co) valence states may play an important role cause ferromagnetism in the prepared samples.



School of Physics

Academic Year 2017

Student's Signature

Advisor's Signature

ACKNOWLEDGEMENTS

I am very grateful to my advisor Prof. Dr. Santi Maensiri for his great advisory, kind patience, guidance, supports, helps and inspiration on me to become a good researcher. I would like to thank the examination committee, Dr. Nuanwan Sanguansak, Assoc. Prof. Dr. Prayoon Songsiriritthgul, Assoc. Prof. Dr. Worawat Meevasana for their suggestion and correction of the thesis. I also would like to thank Dr. Unchista Wongpratrat for giving advice on VSM, XANES results, and everything for her help, and thank you Dr. Somchai Sonsupap for giving advice and great support on my thesis.

This work would not be completed without supports and helps from my team of Advanced Materials Physics Laboratory (AMP) and the Center for Scientific and Technological Equipment, Suranaree University of Technology for great support, encouragement. Thank you, Department of Physics Faculty of Science, Khon Kaen University, and Synchrotron Light Research Institute, Thailand for their helps in operating equipment during measurements.

Finally, I would like to my express appreciation to my parents, sister and my friends for great support, encouragement, and good advice to me throughout my studies.

Panwit Sangkhaoartyon

CONTENTS

	Page
ABSTRACT IN THAI.....	I
ABSTRACT IN ENGLISH	III
ACKNOWLEDGEMENTS	V
LIST OF TABLES	IX
LIST OF FIGURES	XII
CHAPTER	
I INTRODUCTION.....	1
1.1 Principle and reason.....	1
1.2 Objectives of the dissertation.....	3
1.3 Scope and limitation of the study.....	4
1.4 Anticipated outcomes	4
II LITERATURE REVIEW	5
2.1 Spintronics.....	5
2.2 Diluted magnetic semiconductors.....	6
2.3 Cerium oxide (CeO ₂).....	7
2.4 Magnetic properties in dilute magnetic oxides	10
2.5 Mechanism of magnetism in dilute magnetic oxide	12
2.5.1 The double exchange model.....	12
2.5.2 The F-center exchange	13

CONTENTS (Continued)

		Page
III	RESEARCH METHODOLOGY	16
3.1	Materials.....	16
3.2	Preparation and method	17
3.3	Phase identification, structural characterization and morphology.....	19
3.3.1	The thermogravimetric analysis and differential scanning calorimetry (TGA/DSC).....	19
3.3.2	X-Ray diffraction (XRD).....	19
3.3.3	Transmission electron microscopy (TEM) and High-resolution transmission electron microscopy (HR-TEM).....	21
3.3.4	Field-emission scanning electron microscopy (FE-SEM).....	21
3.4	Optical properties and valence state determination	22
3.4.1	UV-visible spectroscopy (UV-Vis).....	22
3.4.2	X-ray absorption near-edge structure (XANES).....	23
3.5	Magnetic measurements	24
3.5.1	Vibrating sample magnetometry (VSM)	24
IV	RESULTS AND DISCUSSION.....	26
4.1	CeO ₂ nanoparticles	26
4.1.1	Structural characterization, morphology, and absorption of CeO ₂ nanoparticles.....	26
4.1.2	Magnetic properties of CeO ₂ nanoparticles.....	38
4.2	Mn-doped CeO ₂ nanoparticles.....	39

CONTENTS (Continued)

	Page
4.2.1 Structural characterization, morphology, and absorption of Mn-doped CeO ₂ nanoparticles	39
4.2.2 Magnetic properties of Mn-doped CeO ₂ nanoparticles.....	55
4.3 Co-doped CeO ₂ nanoparticles.....	58
4.3.1 Structural characterization, morphology, and absorption of Co-doped CeO ₂ nanoparticles	59
4.3.2 Magnetic properties of Co-doped CeO ₂ nanoparticles.....	75
V CONCLUSIONS AND SUGGESTIONS.....	79
5.1 Conclusions.....	79
5.2 Suggestions.....	80
REFERENCES.....	81
CURRICULUM VITAE.....	88

LIST OF TABLES

Table	Page
2.1	Physical properties of cerium oxide.....8
2.2	Synthesized methods of CeO ₂ -based nanostructures9
2.3	An example of transition metals with their charges, electron configurations and ions certain radius (Adapted from Coey (2006)).....11
3.1	List of the materials used for CeO ₂ and Ce _{1-x} TM _x O ₂ nanoparticle preparation16
4.1	Summary of crystallite size and cubic lattice parameter of CeO ₂ calcined samples.....27
4.2	Particle sizes from TEM bright field images and band gap energy (E_g) from UV-vis spectra of CeO ₂ calcined samples.....29
4.3	The mixed percentage between Ce(NO ₃) ₃ and CeO ₂ of CeO ₂ samples were calculated by linear combination fitting of Athena program.....37
4.4	Calculated valence state of Ce according to the edge energy shift positions of CeO ₂ samples.....38
4.5	Summary of crystallite size and cubic lattice parameter of Mn-doped CeO ₂ nanoparticles calcined for in air at 600 °C42
4.6	Particle sizes from TEM bright field images and band gap energy (E_g) from UV-vis spectra of Mn-doped CeO ₂ calcined samples43

LIST OF TABLES (Continued)

Table		Page
4.7	The mixed percentage between $\text{Ce}(\text{NO}_3)_3$ and CeO_2 standard of Mn-doped CeO_2 samples were calculated by linear combination fitting of Athena program	51
4.8	Calculated valence state of Ce according to the edge energy shift positions of Mn-doped CeO_2 samples.....	52
4.9	The mixed percentage between Mn_3O_4 and MnO_2 of Mn-doped CeO_2 samples were calculated by linear combination fitting of Athena program	55
4.10	Calculated valence state of Mn according to the edge energy shift positions of Mn-doped CeO_2 samples.....	55
4.11	Summary of magnetization (M) of CeO_2 and Mn-doped CeO_2 nanoparticles calcined at $600\text{ }^\circ\text{C}$ for 2h	57
4.12	Summary of crystallite size and cubic lattice parameter of Co-doped CeO_2 nanoparticles calcined for in air at $600\text{ }^\circ\text{C}$	61
4.13	Particle sizes from TEM bright field images and band gap energy (E_g) from UV-vis spectra of Co-doped CeO_2 calcined samples	63
4.14	The mixed percentage between $\text{Ce}(\text{NO}_3)_3$ and CeO_2 standard of Co-doped CeO_2 samples were calculated by linear combination fitting of Athena program.....	71

LIST OF TABLES (Continued)

Table	Page
4.15	Calculated valence state of Ce according to the edge energy shift positions of Co-doped CeO ₂ samples.....71
4.16	The mixed percentage between Co ₃ O ₄ and Co(NO ₃) ₂ of Co-doped CeO ₂ samples were calculated by linear combination fitting of Athena program74
4.17	Calculated valence state of Co according to the edge energy shift positions of Co-doped CeO ₂ samples.....75
4.18	Summary of magnetization (<i>M</i>) of CeO ₂ and Mn-doped CeO ₂ nanoparticles calcined at 600 °C for 2h77

LIST OF FIGURES

Figure		Page
2.1	Technologies of spintronics.....	5
2.2	Schematic representation of (a) a non-magnetic, and (b) a dilute Magnetic Oxide	7
2.3	Crystal structure of Cerium oxide (CeO ₂).....	8
2.4	Ferromagnetic coupling of nearby Mn ³⁺ -O-Mn ⁴⁺ ions via double exchange exchange interaction.....	13
2.5	A schematic energy level diagram for a ferromagnetic coupling between two Co ions via a donor electron trapped in the oxygen vacancy.....	15
2.6	Representation of bound magnetic polarons. Cation sites are shown by small circles. Oxygen is not shown, the unoccupied oxygen sites are represented by squares	15
3.1	A schematic view of the preparation of the samples by egg-white solution route.....	18
3.2	A schematic view of the experimental procedures.....	18
3.3	(a) The Bragg reflection from a particular set of the lattice Planes separated by a distance d and θ is a half of the total angle by which the incident beam is detected (b) A Schematic diagram of the XRD.....	20
3.4	Diagram of the FE-SEM.....	22
3.5	(a) Schematic diagram of the XAS (b) Schematic measured of the XANES...24	24

LIST OF FIGURES (Continued)

Figure	Page
3.6	Schematic diagram of the VSM.....25
4.1	XRD patterns of CeO ₂ nanoparticles calcined in air at 500, 600 and 700 °C for 2h28
4.2	TEM bright field images with corresponding SAED patterns of CeO ₂ nanoparticles prepared at (a) 500 °C, (b) 600 °C, (c) 700 °C for 2h.....30
4.3	Room temperature optical absorbance spectra of the CeO ₂ (a) calcined in air at 500, 600 and 700 °C for 2h.....32
4.4	The correlated band gaps are 3.63, 3.60 and 3.59 eV for the CeO ₂ samples calcined at 500 (b), 600 (c) and 700 °C (d), respectively.....33
4.5	XANES spectra at the Ce L ₃ absorption edge for Ce(NO ₃) ₃ , CeO ₂ standard, and CeO ₂ samples.....35
4.6	XANES spectra and linear combination fit of CeO ₂ 500 °C, Ce(NO ₃) ₃ /CeO ₂ standard, reference metal and compound at L-edge.....36
4.7	XANES spectra and linear combination fit of CeO ₂ 600 °C, Ce(NO ₃) ₃ /CeO ₂ standard, reference metal and compound at L-edge.....36
4.8	XANES spectra and linear combination fit of CeO ₂ 700 °C, Ce(NO ₃) ₃ /CeO ₂ standard, reference metal and compound at Ledge.....37
4.9	Magnetic properties of CeO ₂ nanoparticles calcined at various temperatures for 2h in air39

LIST OF FIGURES (Continued)

Figure	Page
4.10	TGA/DSC curves of thermal decomposition of Mn-doped CeO ₂ powder precursor at a heating rate of 10 °C/min in static air40
4.11	XRD patterns of CeO ₂ and Mn-doped CeO ₂ with content 0.05, 0.075 and 0.10 nanoparticles calcined for in air at 600 °C41
4.12	TEM and HRTEM bright field images with corresponding SAED patterns of the Ce _{1-x} Mn _x O ₂ (x = 0.05(a), x = 0.075(b), x = 0.10(c)) samples calcined in air at 600 °C for 2h.....44
4.13	SEM images of Ce _{1-x} Mn _x O ₂ (x = 0.05(a), x = 0.075(b), x = 0.10(c)) calcined in air at 600 °C for 2h.....45
4.14	Room temperature optical absorbance spectra of CeO ₂ and Ce _{1-x} Mn _x O ₂ (x = 0.05, x = 0.075, x = 0.10) samples calcined in air at 600 °C for 2h46
4.15	The correlated band gaps are 3.60, 3.50, 3.53 and 3.61 eV for the CeO ₂ (a) and Ce _{1-x} Mn _x O ₂ (x = 0.05(b), x = 0.075(c), x = 0.10(d)), respectively.....47
4.16	XANES spectra at Ce L ₃ absorption edge for CeO ₂ , Cerium nitrate standard and XANES spectra of CeO ₂ , Mn-doped CeO ₂ samples49
4.17	XANES spectra and linear combination fit of Mn-doped CeO ₂ x = 0.05, Ce(NO ₃) ₃ /CeO ₂ standard.....50
4.18	XANES spectra and linear combination fit of Mn-doped CeO ₂ x = 0.075, Ce(NO ₃) ₃ /CeO ₂ standard.....50

LIST OF FIGURES (Continued)

Figure	Page
4.19	XANES spectra and linear combination fit of Mn-doped CeO ₂ x = 0.10, Ce(NO ₃) ₃ /CeO ₂ standard.....51
4.20	XANES spectra at Mn K absorption edge for Mn ₃ O ₄ , MnO ₂ standard and XANES spectra of Mn-doped CeO ₂ nanoparticles samples.....53
4.21	XANES spectra and linear combination fit of Mn-doped CeO ₂ x = 0.05, Mn ₃ O ₄ /MnO ₂ , reference metal and compound at K-edge53
4.22	XANES spectra and linear combination fit of Mn-doped CeO ₂ x = 0.075, Mn ₃ O ₄ /MnO ₂ , reference metal and compound at K-edge.....54
4.23	XANES spectra and linear combination fit of Mn-doped CeO ₂ x = 0.10, Mn ₃ O ₄ /MnO ₂ , reference metal and compound at K-edge.....54
4.24	Magnetic properties of Mn-doped CeO ₂ nanoparticles calcined at various temperatures for 2h in air at 600 °C.....56
4.25	Ferromagnetic coupling of nearby Mn ³⁺ -O-Mn ⁴⁺ ions via double exchange interaction.....58
4.26	TGA/DSC curves of thermal decomposition of Co-doped CeO ₂ powder precursor at a heating rate of 10 °C/min in static air.....60
4.27	XRD patterns of CeO ₂ and Co-doped CeO ₂ with content 0.05, 0.075 and 0.10 nanoparticles calcined for in air at 600 °C61

LIST OF FIGURES (Continued)

Figure	Page
4.28	TEM and HRTEM bright field images with corresponding SAED patterns of the $Ce_{1-x}Co_xO_2$ ($x = 0.05$ (a), $x = 0.075$ (b), $x = 0.10$ (c)) samples calcined in air at 600 °C for 2h.....64
4.29	SEM images of $Ce_{1-x}Co_xO_2$ ($x = 0.05$ (a), $x = 0.075$ (b), $x = 0.10$ (c)) calcined in air at 600 °C for 2h.....65
4.30	Room temperature optical absorbance spectra of CeO_2 and $Ce_{1-x}Co_xO_2$ ($x = 0.05$, $x = 0.075$, $x = 0.10$) samples calcined in air at 600 °C for 2h.....66
4.31	The correlated band gaps are 3.60, 3.45, 3.52 and 3.57 eV for the CeO_2 (a) and $Ce_{1-x}Co_xO_2$ ($x = 0.05$ (b), $x = 0.075$ (c), $x = 0.10$ (d)), respectively67
4.32	XANES spectra at Ce L_3 absorption edge for CeO_2 , Cerium nitrate standard and XANES spectra of CeO_2 , Co-doped CeO_2 nanoparticles samples.....69
4.33	XANES spectra and linear combination fit of Co-doped CeO_2 $x = 0.05$, $Ce(NO_3)_3/CeO_2$ standard.....69
4.34	XANES spectra and linear combination fit of Co-doped CeO_2 $x = 0.075$, $Ce(NO_3)_3/CeO_2$ standard.....70
4.35	XANES spectra and linear combination fit of Co-doped CeO_2 $x = 0.10$, $Ce(NO_3)_3/CeO_2$ standard.....70
4.36	XANES spectra at Co K absorption edge for Co_3O_4 , $Co(NO_3)_2$ standard and XANES spectra of Mn-doped CeO_2 nanoparticles samples.....72

LIST OF FIGURES (Continued)

Figure		Page
4.37	XANES spectra and linear combination fit of Co-doped CeO_2 $x = 0.05$, $\text{Co}_3\text{O}_4/\text{Co}(\text{NO}_3)_2$, reference metal and compound at K-edge.....	73
4.38	XANES spectra and linear combination fit of Co-doped CeO_2 $x = 0.075$, $\text{Co}_3\text{O}_4/\text{Co}(\text{NO}_3)_2$, reference metal and compound at K-edge.....	73
4.39	XANES spectra and linear combination fit of Co-doped CeO_2 $x = 0.10$, $\text{Co}_3\text{O}_4/\text{Co}(\text{NO}_3)_2$, reference metal and compound at K-edge.....	74
4.40	Magnetic properties of Co-doped CeO_2 nanoparticles calcined at various temperatures for 2h in air at 600 °C.....	76
4.41	A schematic energy level diagram for a ferromagnetic coupling between two Co ions via a donor electron trapped in the oxygen vacancy.....	78

CHAPTER I

INTRODUCTION

1.1 Principle and reason

Oxide-based diluted magnetic semiconductors (O-DMSs) have attracted much attention in recent years since O-DMSs can exhibit magnetism and semi conductivity in a single device. It is important accessory of the new microelectronic technology that use both the charge carriers to control the logic and spin of the electron to control ferromagnetic (FM), which can be regulated by an external magnetic field for magnetic data storage devices. This new technology known as “spintronic” will spawn new devices in electronic technology, computer technology and other technology (Coey, Douvalis, Fitzgerald, and Venkatesan, 2004; Matsumoto et al., 2001). Possible advantages of spintronic devices include higher data processing speed, lower power consumption, lower data volatility, higher data process density, and higher data storage density than presently available. However, the problem of a resistance mismatch at metal/semiconductor interfaces will need to be overcome due to an effective spin injection of spin-polarized current from a FM material into a semiconductor is hindered. Additionally, much interest is now concentrated on the development of ferromagnetism at room temperature (RT) with a Curie temperature (T_C) above RT and understand the physical properties of these O-DMSs materials. Recently, these O-DMSs such as ZnO, TiO₂, SnO₂, and In₂O₃ could exhibit FM at RT with a T_C above RT. RT-FM in the materials can be introduced by doping with just a few percent of 3d transition metal

(TM) ions, such as V, Cr, Mn, Fe, Co or Ni (Coey, 2006). Several models of FM have been proposed for these O-DMSs, including a new exchange mechanism involving donor electrons in an impurity (Coey, Venkateshan, and Fitzgerald, 2005), the carrier (electron) mediated exchange mechanism (Ueda, Tabata, and kawai, 2001) and F-center exchange (FCE) as on defect mediated mechanism, especially oxygen vacancies (V_O) (Coey et al., 2005). The V_O has been proposed to play an important role in the magnetic origin for O-DMSs. However, many studies indicate that the RT- FM may come from precipitation of magnetic clusters or from secondary magnetic phases (Ramachandran, Tiwari, and 2 Narayan, 2004). These mechanisms are far from being understood. Therefore, the exact mechanism of FM is interesting in these systems and a unified framework for this explaining is needed. TM-doped CeO_2 have been also reported to exhibit ferromagnetism at and above RT (Tiwari et al., 2006; Song, Zhang, Wen, Li, and Xiao, 2007; Wen et al., 2007; Brito, Santos, Duque, and Macêdo, 2010). Unlike other O-DMSs, CeO_2 has a cubic structure with lattice parameter $a = 0.54113$ nm that will facilitate the integration of spintronic components with conventional Si-based microelectronic devices. The CeO_2 is often used as storage medium because V_O can be easily formed in CeO_2 without changing its fluorite structure. Early work on CeO_2 -based O-DMSs was focused on thin films (Tiwari et al., 2006; Song et al., 2007) and only a few works have been carried out on powders, bulk, or nanocrystalline form (Wen et al., 2007; Brito et al., 2010). For example, single-phase, Co-doped CeO_2 thin films were reported by Tiwari et al. (2006) and Song et al. (2007) to exhibit FM above RT with large magnetic moments, and these films were transparent in the visible spectrum. The authors also showed that the films could be deposited on glass but with smaller magnetic moment and coercivity. These results suggested that the FM in Co-

doped CeO₂ depends not only on the doping concentration of transition element but also on the microstructure of film, including its crystallization, defects, vacancies, etc. Wen et al. (2007) also found RT-FM exists in undoped and Co-doped CeO₂ powders. RT-FM in undoped CeO₂ originated from V_O while a slight Co doping in CeO₂ caused a nearly two orders enhancement of magnetism to 0.47 emu/g in comparison to the undoped sample. The author suggested that the large RT-FM observed in Co-doped CeO₂ powder originated from a combination effect of V_O and Co doping. The same behavior was found in nanoparticles of Fe-doped CeO₂ with a M_s value of 0.0062 emu/g in 3 at % Fe prepared by a sol-gel method (Brito et al., 2010). Both TM doping and V_O were investigated to be key factors in introducing magnetic ordering based on FCE.

This work reported ferromagnetism observed in undoped CeO₂ and Ce_{1-x}TM_xO₂ (TM = Mn, Co with $0.05 \leq x \leq 0.10$) nanostructures prepared by egg white solution route. The prepared CeO₂ and Ce_{1-x}TM_xO₂ nanostructures are characterized by various techniques including the thermogravimetric analysis and differential scanning calorimetry (TGA/DSC), transmission electron microscopy (TEM), X-ray diffraction (XRD), X-ray absorption spectroscopy (XAS). Magnetic properties of CeO₂ and Ce_{1-x}TM_xO₂ nanostructures are investigated by vibrating sample magnetometer (VSM). The origin of magnetism observed in the prepared samples is discussed.

1.2 Objectives of the study

The objectives of this dissertation are as follows:

1. To characterize dilute magnetic oxide CeO₂-based systems prepared by egg-white solution route.

2. To investigate the effects of TM concentration, TM dopant type, and surface defects on the magnetic properties of CeO₂-based.

3. To study the origin of ferromagnetism in CeO₂-based for further study on spintronic devices.

1.3 Scope and limitation of the study

1. Fabrication of CeO₂-based DMOs by egg white solution route of CeO₂ and Ce_{1-x}TM_xO₂ with TM = Mn, Co ions with $0.05 \leq x \leq 0.10$.

2. Characterization of the fabricated samples by XRD, FE-SEM, TEM, HRTEM, UV-vis, XANES, VSM

3. Study on the effect of TM concentration and TM dopant type on magnetic properties of dilute magnetic oxide CeO₂-based systems.

4. Investigation of the origin of ferromagnetism in dilute magnetic oxide CeO₂-based systems.

1.4 Anticipated outcomes

1. Understanding the synthesis and physical properties of dilute magnetic oxide materials, especially undoped CeO₂ and TM-doped CeO₂.

2. Opening the door to dilute magnetic oxide materials at the nano-scale, which is useful for future technology.

3. Publication of research articles.

CHAPTER II

LITERITURE REVIEW

This chapter reviews the background of spintronics, dilute magnetic semiconductors and dilute magnetic oxides in different forms, including the models and some theoretical mechanisms which can explain the observed ferromagnetism in these systems. Moreover, this chapter reviews the origin of ferromagnetism in TM-doped CeO₂ materials.

2.1 Spintronics

Spintronics, also known as fluxtronics, is the study of the intrinsic spin of the electron and its associated magnetic moment, in addition to its fundamental electronic charge, in solid-state devices. Technology of spintronics is shown in Figure 2.1.

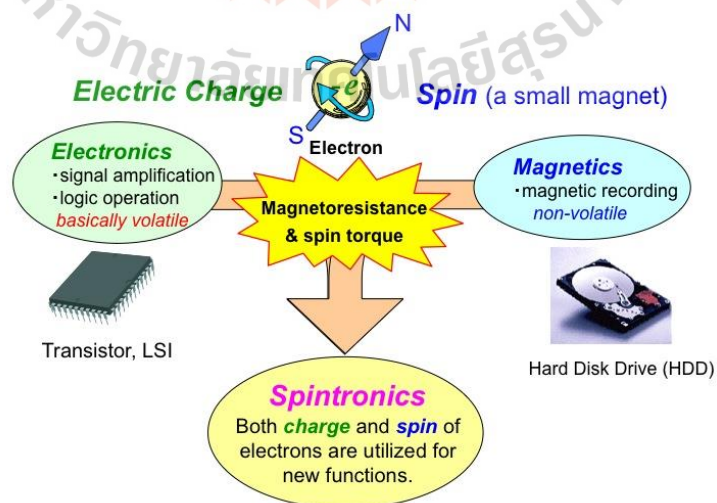


Figure 2.1 Technologies of spintronics (from www.unit.aist.go.jp).

The simplest method of generating a spin-polarized current in a metal is to pass the current through a ferromagnetic material. The most common applications of this effect involve giant magnetoresistance (GMR) devices.

2.2 Diluted magnetic semiconductors

Diluted magnetic semiconductors (DMSs) are one of the most promising candidates for spintronic applications, which take advantage of the charge and spin of electrons in a single material system. A DMS is a nonmagnetic semiconductor (or alloy of nonmagnetic semiconductors) (see Figure 2.2(a)) that is doped with a magnetic element which is usually 3d transition metal (TM) ions such as V, Mn, Fe, Co or Ni, which induce ferromagnetism in the semiconductor host (see Figure 2.2(b)). Therefore, a number of different semiconductor hosts have been investigated to test their magnetic properties. In the past most attention has been paid to Mn-doped GaAs (Ohno et al., 1996; Tanaka et al., 1997; Nagai et al., 2001) and Mn-doped InAs systems (Ohno et al., 1989; Oiwa et al., 2001). However, due to their reported highest Curie temperatures which are around 170 K for Mn-doped GaAs (Ohno, 1998) and 35 K for Mn-doped InAs (Ohno, 2000; Ohno et al., 2002), they are not suitable for practical applications as their T_C are quite low. Therefore, there is a large incentive for developing new DMS materials which are ferromagnetic above room temperature. Some theoretical works predicted room temperature ferromagnetism in TM doped oxide semiconductors.

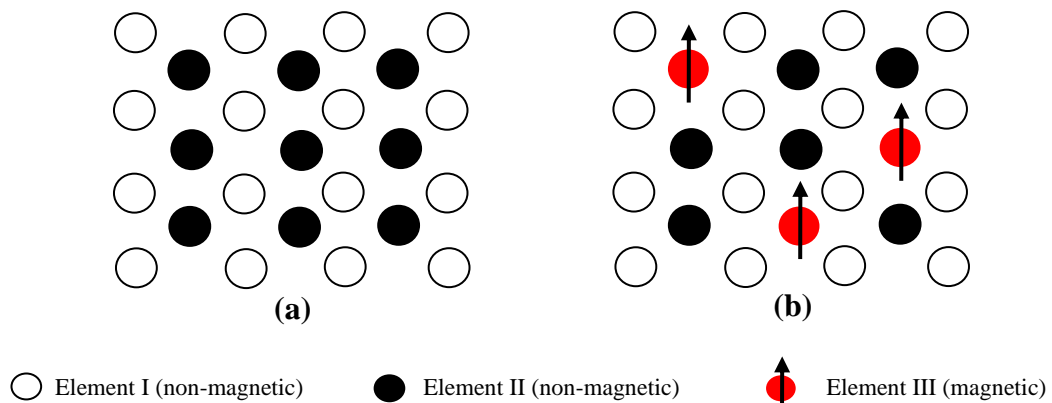


Figure 2.2 Schematic representation of (a) a non-magnetic, and (b) a dilute Magnetic oxide (Ohno, 1998).

2.3 Cerium oxide (CeO₂)

Cerium oxide (CeO₂), also known as ceric oxide, ceria, cerium oxide or cerium dioxide, is an oxide of the rare earth metal cerium. CeO₂ has a cubic fluorite structure ($a = 0.5411$ nm). In unit cell contain atoms of Ce arrange in face centered cubic (FCC) form and a compact oxygen atom in centered unit cell was catch by each Ce atom 4 bond. The crystal structure of cerium oxide is shown in Figure 2.3 The physical properties of CeO₂ are listed in Table 2.1. This structure has a good adhesion with silicon substrate. Therefore, appropriate use combines with spintronics devices (silicon microelectronic devices). CeO₂ have many interest properties due to CeO₂ has a wide band gap ($E \approx 3.4$ eV), good UV absorption, high dielectric value ($\epsilon = 26$), stable with high temperature. CeO₂-based materials have been extensively used in a wide variety of applications such as solid oxide fuel cells (SOFCs), catalysis, luminescence materials, gas sensors, etc.

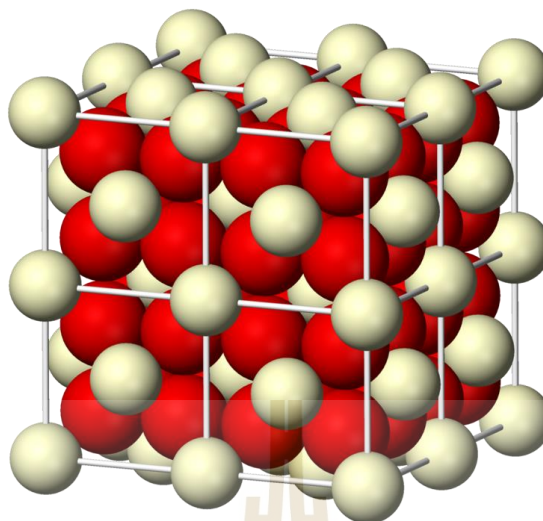


Figure 2.3 Crystal structure of Cerium oxide (CeO_2). ([http://en.wikipedia.org/wiki/Cerium\(IV\)_oxide](http://en.wikipedia.org/wiki/Cerium(IV)_oxide) /media/File: Ceria3D-ionic.png).

Table 2.1 Physical properties of cerium oxide (Wen et al., 2007).

Property	Value
Appearance	Yellow powder
Melting point	2500 °C
Specific gravity	7.3 g/cm ³
Solubility	Insoluble in water, moderately soluble in strong mineral acids.
Stability	Slightly hygroscopic, will absorb small amount of moisture and CO ₂ from the atmosphere.
Crystal structure	Cubic, face centered
Space group	Fm3m
Lattice parameter	0.5411 nm

In recent years, nanometer-sized particles have attracted much attention because of their unique physical and chemical properties significantly different from their bulk counterparts as well as their potential applications in industry. Various types of nanostructures can be synthesized by many methods such as gas evaporation, laser vaporization, ionized beam deposition, sol-gel processing, freeze drying, etc. So far, various types of CeO₂ nanostructures can be synthesized by many methods as summarized in Table 2.2.

Table 2.2 Synthesized methods of CeO₂-based nanostructures.

Route, Synthesis methods	Materials	Nanostructures	Interest	References
So-gel Processing	- Cerium(III) acetate hydrate - Egg-white	- Nanoparticles - Size 6-30 nm	- Cheapness - Good control of the sized - Good optical properties	Maensiri et al. (2007).
Homogeneous precipitation	- Cerium nitrate - Alcohol/ Water solution - Ethylene glycol	- Nanoparticles - Size about 15 nm	- The mechanism of crystal	Chu et al. (1993).

Table 2.2 Synthesized methods of CeO₂-based nanostructures (Continued).

			- Solid	
Microemulsion method	- Cerium nitrate - Cationic surfactant	- Nanocrystal - Size 6-8 nm	electrolyte - Control surface and size	Zhang et al. (2002).
Decomposition method	- Cerium (III) acetate hydrate - Chitosan	- Nanoparticles - Size 7-62 nm	- Magnetic properties - Oxygen vacancy	Phokha (2008).

2.4 Magnetic properties in dilute magnetic oxides

Magnetism of oxide material has been a subject of intense study for long time. In 2000, Dietl et al., theoretically predicted that the FM at high temperature could be obtained in many semiconductors such as ZnO, GaAs, GaN by doping with Mn (Dietl, Ohno, Matsukura, Cibert and Ferrand, 2000). Later, the room temperature ferromagnetism (RTFM) was observed on TiO₂ (Matsumoto et al., 2001) and ZnO (Ueda, Tabata and Kawai, 2001) doped with a few percent of a transition metal such as, Co, Mn, Cr and Ni. Much attention has been paid to study the ferromagnetism in thin films including TiO₂ with V, Cr, Fe, Co or Ni, SnO₂ with V, Cr, Mn, Fe or Co and ZnO with Ti, V, Cr, Mn, Fe, Co, Ni or Cu (Coey, 2006). The 3d dopant concentrations are generally below 10% (Coey et al., 2005). Nanoparticles of some of these systems are also reported to be ferromagnetic, but well-crystallized, bulk material does not order magnetically. Previous studies on the dilute magnetic oxides,

dopants and their Curie temperatures (T_c) and magnetic moment are reported in Table 2.3. Despite the many studies, the basic principles, and mechanisms of the magnetism of DMOs are still unclear. There is no clear understanding whether the magnetic oxide is originated from the electron in the 3d orbital or 4f orbitals of transition metal, and the rare earth metal cation which is the source of the magnetic moment will exhibit room temperature ferromagnetism (RTFM) or higher than room temperature ferromagnetism. Many models of FM have been proposed, including an exchange mechanism related to donor electrons in an impurity (Coey et al., 2005), a superexchange or double exchange interaction (Zener, 1951, Spaldin, 2003), and a 13 defect mediated mechanism like Bound Magnetic Polaron model (BMP) (Coey, Venkatesan and Fitzgerald, 2005).

Table 2.3 An example of transition metals with their charges, electron configurations and ions certain radius (Adapted from Coey, 2006).

Ions	Charge	Configuration	Radius (nm)
Ti	3+ / 4+	3d1 / 3d0	0.069/0.061
Cr	3+	3d3	0.064
Mn	2+ / 3+ / 4+	3d5 / 3d4 / 3d3	0.083/0.065/0.053
Fe	2+ / 3+	3d6 / 3d5	0.082/0.065
Co	2+ / 3+	3d7 / 3d6	0.082/0.061
Ni	2+ / 3+	3d8 / 3d7	0.078/0.069
Cu	2+	3d9	0.072

2.5 Mechanism of magnetism in dilute magnetic oxide

A fundamental understanding of ferromagnetic behavior in dilute magnetic semiconductors and 3d TM ions-doped dilute magnetic oxides is still far from clear. There exist some theoretical models which explain the observed ferromagnetism at RT in these systems.

2.5.1 The double exchange model

Double exchange is a related magnetic coupling interaction and has important implications for whether materials are ferromagnetic, AFM, or neither. It was proposed by Kramers (1934) when he noticed in crystals like MnO, there are Mn atoms that manage to interact with one another despite having nonmagnetic oxygen atoms between them. Anderson (1950) later refined Kramers' model in 1950. The double exchange interaction is explained by hopping of electrons between two neighbor TM ions. In the DMS materials, the 3d levels of TM ions are split by the crystal field into lower energy triplet t_{2g} and higher energy doublet e_g levels. The spin-up (\uparrow) and spin-down (\downarrow) states are also split by the exchange splitting. For example, consider the 180 degree interaction of Mn-O-Mn in which the Mn " e_g " orbitals are directly interacting with the O " $2p$ " orbitals. The kinetic energy of the system is lowered if the magnetic moments align parallel in order to conform with Hund's rules, all unpaired electrons within each atom or ion will be aligned parallel, since parallel alignment allows electrons hop from Mn^{3+} to Mn^{4+} . Hence the overall energy saving can lead to ferromagnetic alignment of neighboring ions, as shown in Figure 2.4.

This model is similar to superexchange. However, in superexchange, a ferromagnetic or AFM alignment occurs between two metal with the same valence (number of electrons) and the electrons do not actually move between the two metal

cations, the occupancy of the d-shell of the two metal ions is the same or differs by two while in double-exchange, the interaction occurs only when one atom has an extra electron compared to the other and the electrons actually move between the cations ions via the intermediate ligand (e.g. oxygen); this results in a material displaying double exchange ferromagnetic or AFM coupling also displaying metallic conductivity behavior.

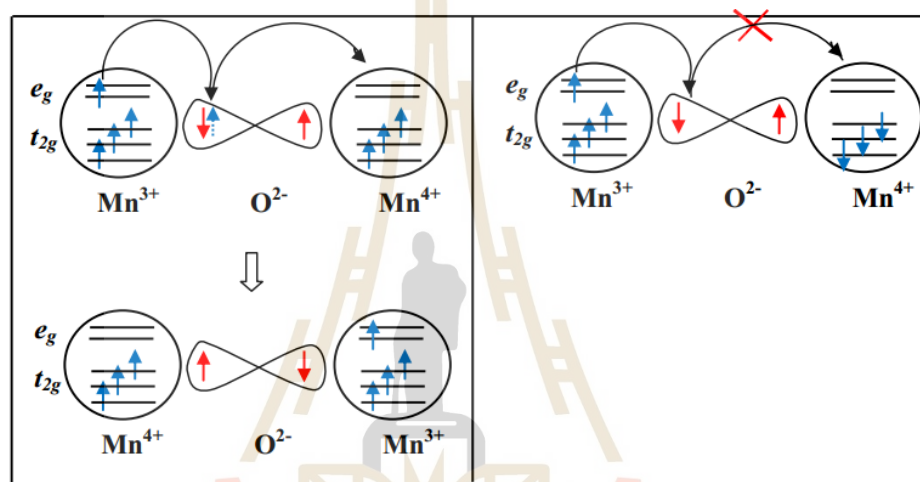


Figure 2.4 Ferromagnetic coupling of nearby Mn^{3+} -O- Mn^{4+} ions via double exchange interaction (Anderson, 1950).

2.5.2 The *F*-center exchange

The ferromagnetic ordering of TM ions in O-DMS materials is often reported by the FCE. This direct ferromagnetic coupling is a type of crystallographic defect in which an anionic (for e.g. O^{2-} in case of oxides) vacancy by a crystal is filled by one or more electrons in the oxide host. The ferromagnetic exchange occurs between defects and surrounding TM. The origin of vacancy, when the compound is heated to a high temperature the electrons get excited and get displaced from their crystal structure, but while doping so, these electrons leave behind by some electrons in the vacated

spaces. This leads to the existence of F -center implied the formation of one electron trapped in a V_O is called F^+ center. It formed lie/band deep in the gap and support strong FM ground state reported by Shah et al. (2009). In contrast of this, two trapped electrons occupied vacancies (F^0 center) formed lie above the conduction band edge. This can only mediate weak AFM exchange between magnetic dopants, or in some cases very weak FM. The calculations obtained here provide evidence that the interaction of the F^+ center can induce strong FM more than F^0 center, due to large density of states at the fermi level, leading to these F -center overlap in the samples. The radius of the electron trapped orbital, overlaps the d shells of both TM ion neighbors, is of the order $a_0\varepsilon$ where a_0 is the Bohr radius and ε is the dielectric constant of the material. Recently, the electronic structure calculations of Patterson (2005) indicated that the V_O with a spin half strongly promote ferromagnetic coupling of Co ions in Co-doped ZnO, as schematically presented in Figure 2.5. A ferromagnetic ground state occurs between two Co ions through the V_O spin, in agreement with the impurity band model of Coey et al. (2005).

This F -center leads to the form BMP (Berciu and Bhat, 2001; Bhat, Berciu, Kennett and Wan, 2002; Dietl et al., 2002; Sharma, Hwang, and Kaminiski, 2003) and neighboring BMPs can overlap and result in the long-range TM-TM ferromagnetic coupling with almost all TM ions exhibit the same spin direction. In this model, the formation of BMP is explained by the exchange interaction between many localized TM ion spins via much lower number of weakly localized charge carriers. The overlap of neighboring magnetic polarons leads to a long-range ferromagnetic state and the ferromagnetic transition occurs when the polaron size is

equal to the sample size. Recently, Coey et al. (2005) applied this model to diluted magnetic oxides. They proposed that the ferromagnetic exchange coupling of TM ions in n-type diluted magnetic oxides is mediated by the shallow donor electrons trapped by the oxygen vacancy that tend to form bound magnetic polarons within their hydrogenic orbits (see Figure 2.6).

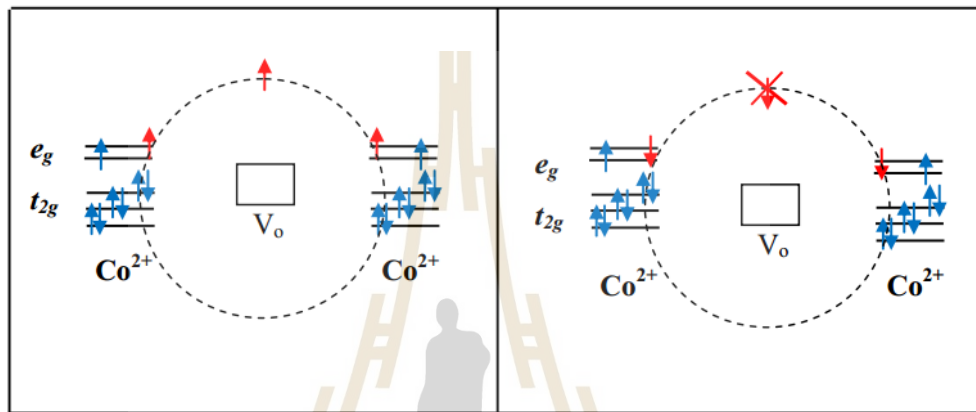


Figure 2.5 A schematic energy level diagram for a ferromagnetic coupling between Two Co ions via a donor electron trapped in the oxygen vacancy (Reproduced from Patterson, 2005).

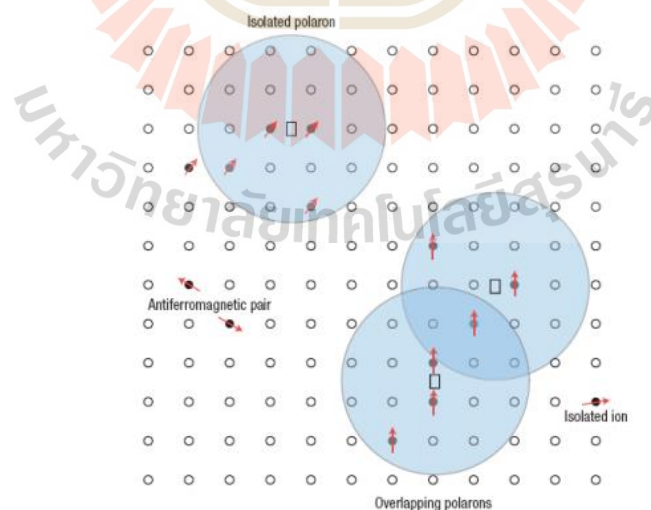


Figure 2.6 Representation of bound magnetic polarons. Cation sites are shown by small circles. Oxygen is not shown, the unoccupied oxygen sites are represented by squares (Coey et al., 2005).

CHAPTER III

RESEARCH METHODOLOGY

This chapter describes the methods and techniques used to synthesize and characterize the undoped CeO₂ and the CeO₂ doped with Mn, Co nanoparticles by egg-white solution method. The prepared samples were characterized by XRD, FE-SEM, TEM, HRTEM, UV-vis, XANES and VSM, respectively.

3.1 Materials

The materials used in this research are shown in Table 3.1.

Table 3.1 List of the materials used for CeO₂ and Ce_{1-x}Tm_xO₂ nanoparticle preparation.

Material	Source	Purity
Cerium(III)nitrate (Ce(NO ₃) ₃ ·6H ₂ O)	Kento	99.99 %
Cobalt(II)nitrate (Co(NO ₃) ₂ ·6H ₂ O)	Sigma-Aldrich	99.999 %
Manganese (II)nitrate (Mn(NO ₃) ₂ ·H ₂ O)	Kento	99.99 %
Deionized water		
Egg-White		

3.2 Preparation method

A mix of freshly extracted egg white with 50 mL and 50 mL of deionized water (pH 10) was stirred at room temperature (27 °C) until homogenized. Cerium(III) nitrate hexahydrate, $\text{Ce}(\text{NO}_3)_3 \cdot 6\text{H}_2\text{O}$ (99.99 % purity; Kanto Corporation, Portland, OR, USA) was added slowly to the egg white-DI water mixer. In this study 2.5016 g (5 % by weight) of $\text{Ce}(\text{NO}_3)_3 \cdot 6\text{H}_2\text{O}$ was added to 90 g of freshly extracted egg white-DI water. The $\text{Ce}_{1-x}\text{TM}_x\text{O}_2$ (TM = Co, Mn) ($x = 0.05, 0.075$ and 0.10) structures, calculated amounts of $\text{Ce}(\text{NO}_3)_3 \cdot 6\text{H}_2\text{O}$, cobalt (II) nitrate hexahydrate ($\text{Co}(\text{NO}_3)_2 \cdot 6\text{H}_2\text{O}$), manganese (II) nitrate hydrate ($\text{Mn}(\text{NO}_3)_2 \cdot \text{H}_2\text{O}$) and dopants are stirring at room temperature (27 °C) until obtain a homogeneous solution. At this step, the extract egg white was acting as a matrix for entrapment of cerium ion, generating a gel precursor (Maensiri et al., 2007; Maensiri et al., 2009). Throughout the whole process described above, no pH adjustment was made. The pH of ovalbumin-DI water mix changed from the initial value of 10 to 7 after addition and mixing of cerium nitrate hexahydrate. The mix solution was dried by heating on a hot plate at 80 °C under vigorous stirring for 12h. The dried precursor was crushed into powder using a mortar and pestle. The CeO_2 crushed powder was calcined in a box-furnace at 500, 600 and 700 °C for 2h in air and the CeO_2 doped samples were calcined in air at 600 °C. The sample preparation of egg-white solution route and characterization are schematically shown in figures 3.1 and 3.2.

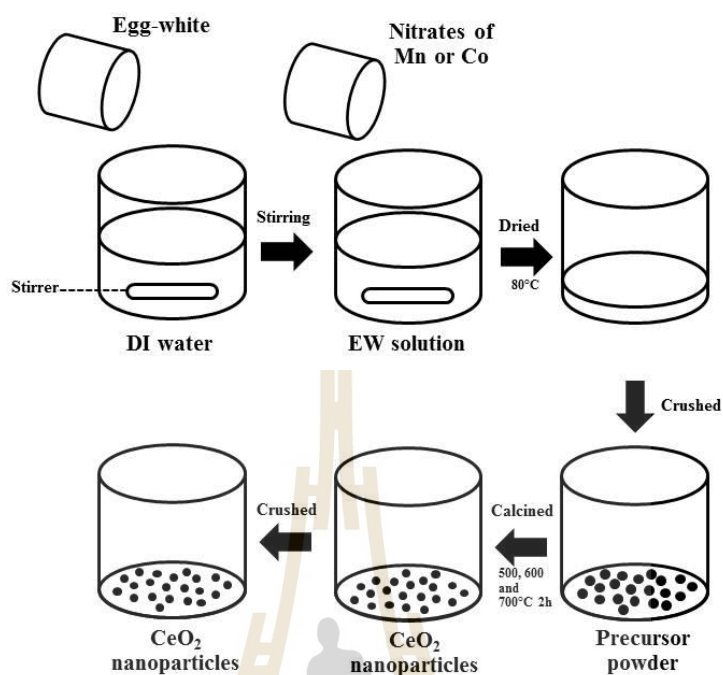


Figure 3.1 A schematic view of the preparation of the samples by egg-white solution route.

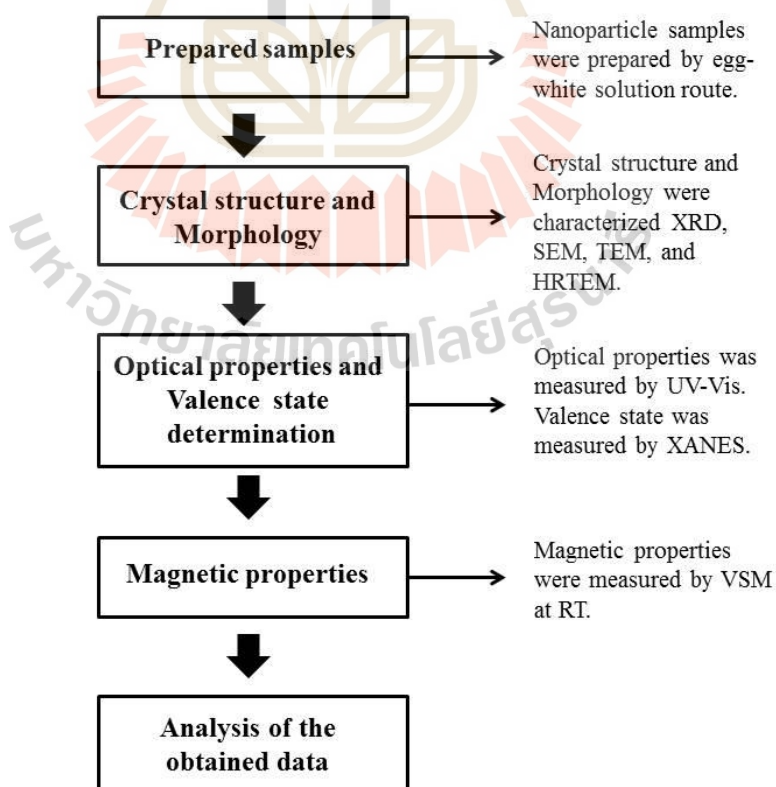


Figure 3.2 A schematic view of the experimental procedures.

3.3 Phase identification, structural characterization and morphology

This part studied the TGA/DSC, XRD, TEM, HRTEM, and SEM measurements.

3.3.1 The thermogravimetric analysis and differential scanning calorimetry (TGA/DSC)

TGA and DSC are the techniques used to measure the change in mass of the sample when it is subjected to a heating rate (10 °C/min) and under flowing gas (e.g., dried air, Ar or N₂) in controlled atmosphere. The measurement of changes in the mass of the sample as a function of temperature shows the purity, crystallization, and decomposition behavior. These techniques are widely used to study the thermal characteristics of substances, natural polymer (egg-white). The weight losses of the sample during heat treatment are evidence of polymer structure deformation or decomposition which is useful for consideration of the proper calcination temperature.

In this work, the thermal stability and exothermic reaction of metal oxides were carried out in air for samples in the temperature range of 50-800 °C with a heating rate of 10 °C min⁻¹ using Perkin Elmer (TGA-7) at the center for scientific and technological equipment, SUT.

3.3.2 X-Ray diffraction (XRD)

All of the samples investigated in the study were thoroughly characterized using X-Ray diffraction (XRD). XRD is used to determine the crystallographic structure and chemical composition of materials. In 1915, William L. Bragg and his father, Sir William H. Bragg, were awarded the Nobel Prize in physics for their mathematical description of x-ray diffraction and for their determination of crystal

several structures. Bragg's law, the condition for constructive interference, is given in Equation 3.1.

$$n\lambda = 2d \sin \theta \quad (3.1)$$

Where n is an integer, λ is the wavelength of the X-ray radiation and θ is angle of incidence and d is the distance between lattice planes. The Bragg's Law conditions are satisfied by different d -spacings in polycrystalline and single crystalline materials. Plotting the angular positions and intensities of the resultant diffracted peaks of the radiation produces a pattern, which is characteristic of the sample. XRD patterns of samples were obtained using a Philips X'Pert PW3040 θ - 2θ X-Ray Diffractometer using a Cu-K α source and the optimum scan rate for 2θ was 20-80°. The Bragg reflection from a particular set of the lattice planes and a schematic diagram of the XRD are shown in figures 3.3(a) and 3.3(b) respectively.

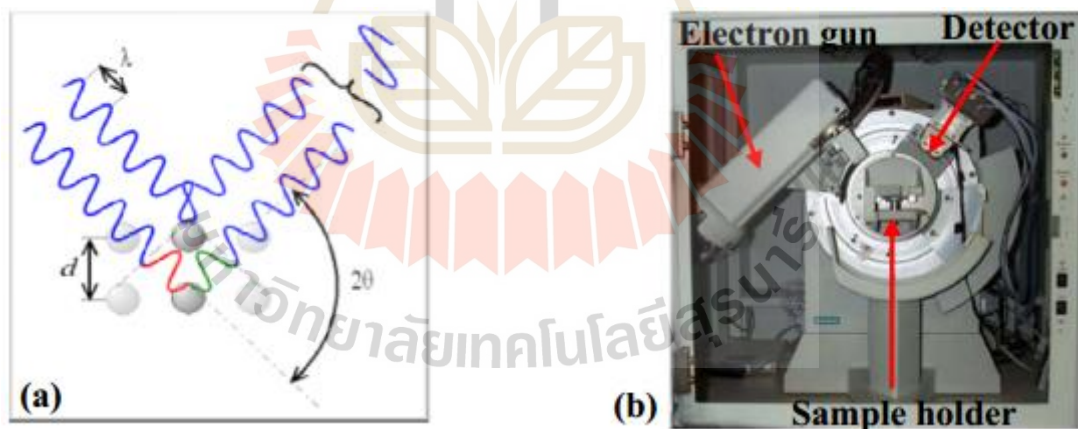


Figure 3.3 (a) The Bragg reflection from a particular set of the lattice planes separated by a distance d and θ is a half of the total angle by which the incident beam is detected (b) A Schematic diagram of the XRD (Speliotis, n.d.).

3.3.3 Transmission electron microscopy (TEM) and High-resolution transmission electron microscopy (HR-TEM)

Transmission electron microscopy (TEM) was used to study the morphology and structure of prepared samples. TEM is a microscopy technique whereby a beam of electrons is transmitted through an ultra-thin specimen, interacting with the specimen as it passes through it. An image is formed from the electron transmitted through the specimen, magnified and focused by an objective lens and appearing on an imaging screen. The morphology and crystal structure of the fine nanoparticles were characterized by transmission electron microscopy (JEOL JEM 200kV conventional, Japan and FEI, TECNAI G₂ 20), equipped with High-resolution transmission electron microscopy (HR-TEM) for the investigation of the d spacing of the lattice fringe in the samples using a JEOL JEM 2010 (200 kV, Japan).

3.3.4 Field-emission scanning electron microscopy (FE-SEM)

Sample morphology was examined using field emission scanning electron microscopy (FE-SEM). The processing of FE-SEM operates under a vacuum, and electrons generated by a field emission source are accelerated in a field gradient. The beam passes through electromagnetic lenses, focusing onto the specimen. As a result of this bombardment different types of electrons are emitted from the specimen. A detector catches the secondary electrons, and an image of the sample surface is constructed by comparing the intensity of these secondary electrons to the scanning primary electron beam. Finally, the image is displayed on a monitor (see Figure 3.4). This morphology of samples was obtained using field emission scanning electron microscopy (JEOL JSM-6335F).

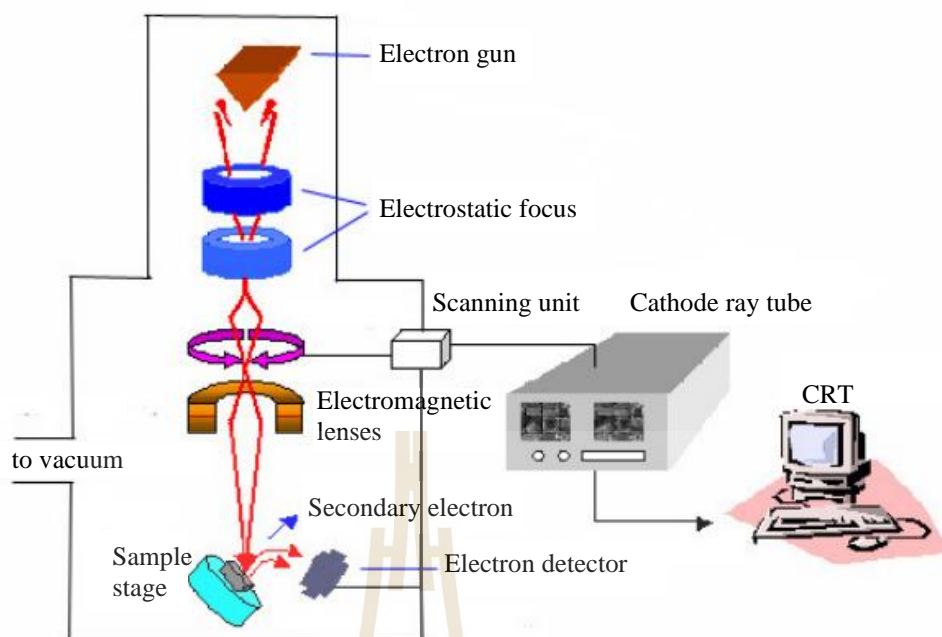


Figure 3.4 Diagram of the FE-SEM (New Mexico Tech., n.d.).

3.4 Optical properties and valence state determination

3.4.1 UV-visible spectroscopy (UV-vis)

Ultraviolet-visible spectroscopy or ultraviolet-visible spectrophotometry (UV-vis or UV/vis) refers to absorption spectroscopy or reflectance spectroscopy in the ultraviolet-visible spectral region. This means it uses light in the visible and adjacent (near-UV and near-infrared (NIR)) ranges. The absorption or reflectance in the visible range directly affects the perceived color of the chemicals involved. In this region of the electromagnetic spectrum, molecules undergo electronic transitions. This technique is complementary to fluorescence spectroscopy, in that fluorescence deals with transitions from the excited state to the ground state, while absorption measures transitions from the ground state to the excited state. UV-vis spectroscopy is routinely used in analytical chemistry for the quantitative determination of different analysis, such as transition metal ions, highly conjugated organic compounds, and biological

macromolecules. Spectroscopic analysis is commonly carried out in solutions, but solids and gases may also be studied. The absorption spectra of dilute magnetic oxide CeO₂-based samples were measured in the range of 200-800 nm using a UV-3101PC UV-Vis-NIR scanning spectrometer (Shimadzu, Japan).

3.4.2 X-ray absorption near-edge structure (XANES)

XAS is an element specific technique and is broken into 2 regimes consisting of x-ray absorption near-edge structure (XANES) and extended x-ray absorption fine-structure (EXAFS), which contain related but slightly different information about an element is local coordination and chemical state. An x-ray is absorbed by an atom when the energy of the x-ray is transferred to a core-level electron (K, L, or M shell) which is ejected from the atom. The atom is left in an excited state with an empty electronic level (a core hole). Any excess energy from the x-ray is given to the ejected photo-electron (see Figure 3.5(a)). XAS measures the energy dependence of the x-ray absorption coefficient $\mu(E)$ at and above the absorption edge of a selected element. $\mu(E)$ can be measured two ways. First way is Transmission mode as shown in Equation 3.2. The absorption is measured directly by measuring what is transmitted through the sample. Second way is Fluorescence mode (see Equation 3.3). The re-filling of the deep core hole is detected. Typically, the fluorescent x-ray is measured (see Figure 3.6(b)).

$$\mu(E)t = -\ln(I / I_0) \quad (3.2)$$

$$\mu(E) \propto I_f / I_0 \quad (3.3)$$

where I_0 is the x-ray intensity hitting, I is the intensity transmitted, $\mu(E)$ is absorption coefficient, t is a material of thickness, and I_f is the fluorescence intensity.

The Ce L_3 edge and Co and Mn K edge were studied using XANES in transmission and fluorescence mode at the BL5 Station at Siam Photon Laboratory (Synchrotron Light Research Institute (Public Organization), SLRI) in Nakhon Ratchasima, Thailand.

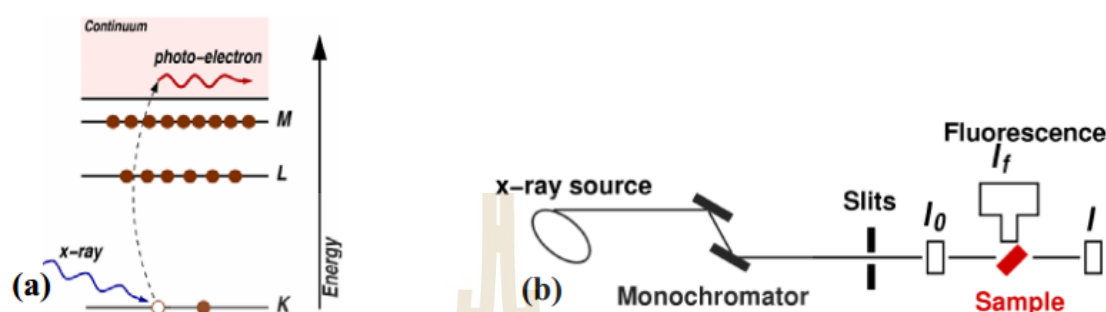


Figure 3.5 (a) Schematic diagram of the XAS (b) Schematic measured of the XANES (from xafs.org, 2008).

3.5 Magnetic measurements

3.5.1 Vibrating sample magnetometry (VSM)

A vibrating sample magnetometer (VSM) measures the magnetic properties of a large variety of materials including diamagnetics, paramagnetics, ferromagnetics, and superparamagnetics. The VSM employs an electromagnet which provides the magnetizing field, a vibrator mechanism to vibrate the sample in the magnetic field, and pick-up coils which generate signal voltage due to the changing flux emanating from the vibrating sample as shown schematically in Figure 3.6. The sample is vibrated parallel to the field direction. Powders were weighed, and then placed in a small sample holder located at the end of a sample rod mounted in an electromechanical transducer for measurement. The output measurement displays the magnetic moment as a function of a magnetic field. The measurement can be made at 293 K in a field of 10,000 Oe (7403, Lakeshore, USA)

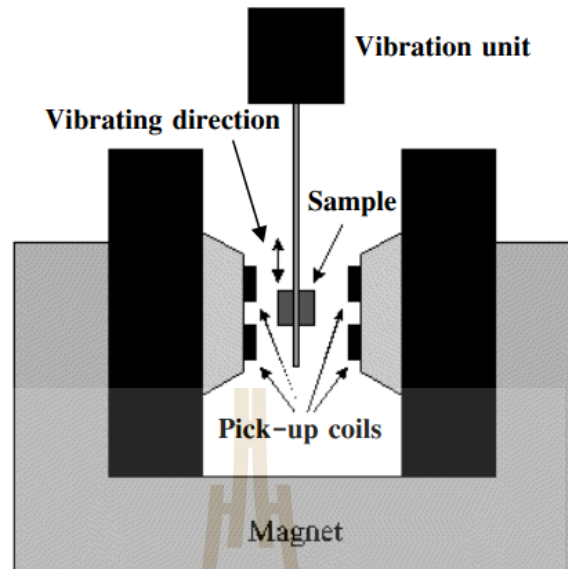
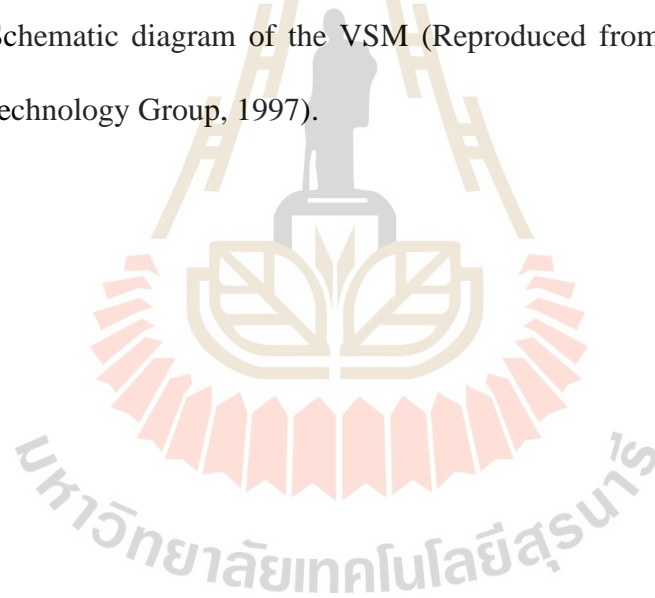


Figure 3.6 Schematic diagram of the VSM (Reproduced from Information Storage Technology Group, 1997).



CHAPTER IV

RESULTS AND DISCUSSION

This chapter presents the experimental results (XRD, FE-SEM, TEM, HRTEM, UV-vis, XANES and VSM) and discussion for pure and TM (Mn, Co) doped-CeO₂ samples. The origin of ferromagnetism in the synthesized samples is discussed.

4.1 CeO₂ nanoparticles

This part presented pure CeO₂ nanoparticles on structural characterization, morphology, absorption, and magnetic properties.

4.1.1 Structural characterization, morphology, and absorption of CeO₂ nanoparticles

The structure and phase composition of the samples were determined by XRD measurements. Figure 4.1 shows the XRD patterns of the undoped CeO₂ prepared at 500, 600 and 700 °C for 2h in air. The precursor sample shows no XRD peaks, indicating its amorphous nature, whereas all calcined samples exhibited XRD peaks that correspond to the (111), (200), (220), (311), and (222) planes of consistent with the face-centered cubic fluorite structure of CeO₂ in the standard data from JCPDS 34-0394 (vertical lines below the patterns). It is clearly seen that the reflection peak become sharper and narrower with increasing calcination temperature, indicating that the crystal size increases and the crystallinity of CeO₂ become better define during the calcination

process. The average crystallite size D of the CeO_2 samples were calculated from X-ray line broadening of the reflections of (111) using Scherrer's equation (equation 4.1)

$$(D = K\lambda/(\beta \cos\theta)) \quad (4.1)$$

where λ is the wavelength of the X-ray radiation, K is a constant taken as 8.9, θ is the diffraction angle and β is the full width at half-maximum (*fwhm*) and were found to be 10.0 ± 3.2 , 21.7 ± 4.6 and 35.4 ± 2.8 nm for the CeO_2 samples calcined at 500, 600 and 700 °C, respectively. The values of lattice parameter a calculated from the XRD spectra were 0.54071 ± 0.00018 , 0.54146 ± 0.00017 and 0.54149 ± 0.00024 nm for the CeO_2 samples calcined at 500, 600 and 700 °C, respectively. The crystallite size and cubic lattice parameter are also summarized in Table 4.1. It is noted that the values of the lattice parameter a for the CeO_2 sample calcined at 500 °C is lower than that reported for CeO_2 ($a = 0.54113$ nm) in the standard data JCPDS 34-0394, whereas the values for the CeO_2 samples calcined at 600 and 700 °C are close to that of the standard data.

Table 4.1 Summary of crystallite size and cubic lattice parameter of CeO_2 calcined samples.

Samples	Crystallite sizes	Cubic lattice
CeO_2	from XRD (nm)	parameter,
		a (nm)
500 °C	10.0 ± 3.2	0.54071 ± 0.00018
600 °C	21.7 ± 4.6	0.54146 ± 0.00017
700 °C	35.4 ± 2.8	0.54149 ± 0.00024

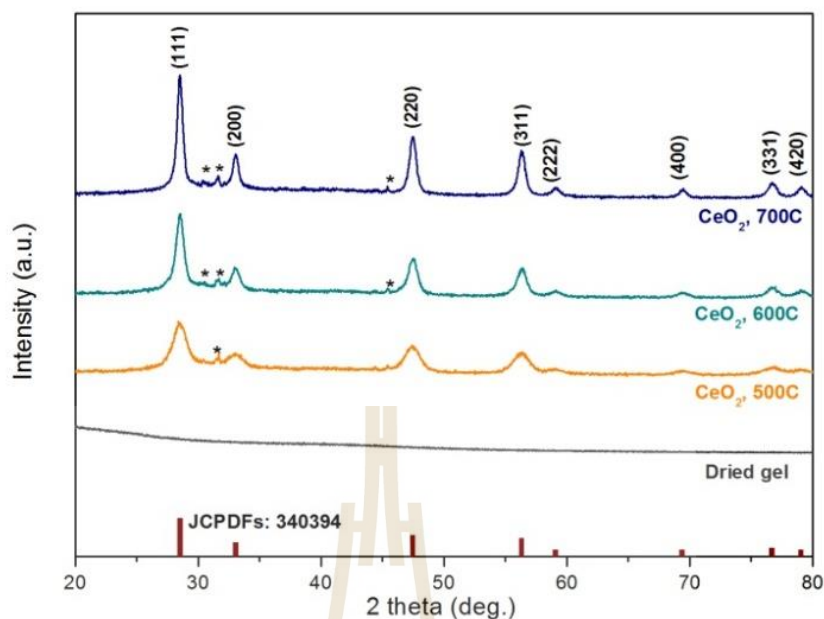


Figure 4.1 XRD patterns of CeO₂ nanoparticles calcined in air at 500, 600 and 700 °C for 2h.

The morphology and structure of the CeO₂ samples were investigated by TEM. Figure 4.2 shows all overview TEM images with corresponding selected area electron diffraction (SAED) patterns of thin platelike clusters of nanocrystalline CeO₂ sample calcined at 500, 600 and 700 °C for 2h. These platelike cluster consist of networked nanocrystalline particles. Increasing calcination temperature results in more intense spots in the electron diffraction patterns and the CeO₂ samples calcined at 700 °C shown a strong spotty-ring pattern indicating a larger particle size that is highly crystalline compared to the samples calcined at 500 and 600 °C. Measured interplanar spacings (d_{hkl}) from selected area electron diffraction pattern in Figure 4.3 are a good agreement with the values in the standard data JCPDS 34-0394. The size of CeO₂ nanoparticles increase with increasing calcined temperature. The 500 °C calcined sample contains networked nanoparticles of ~ 5 - 10 nm in size, whereas the 600 °C

calcined sample contain network nanoparticles of ~ 15 - 30 nm. As expected, the 700 °C calcined sample consists of network nanoparticles with the largest particle sizes of 40-60 nm (see summary particle sizes from TEM in Table 4.2).

Table 4.2 Particle sizes from TEM bright field images and band gap energy (E_g) from UV-vis spectra of CeO₂ calcined samples.

Samples	Particle sizes from TEM (nm)	Band gap E_g (eV)
CeO ₂		
500 °C	5 - 10	3.63
600 °C	15 - 30	3.60
700 °C	40 - 60	3.59

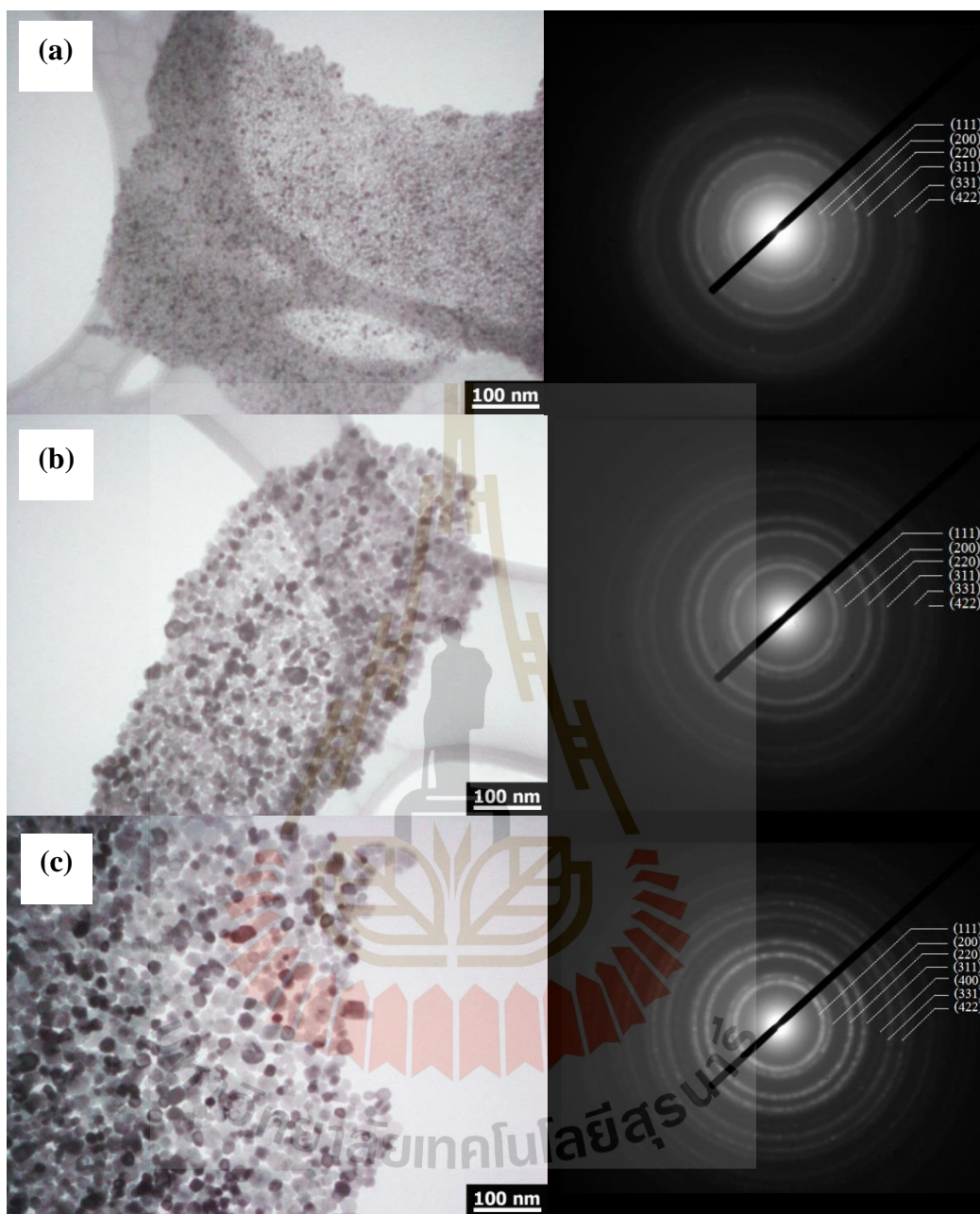


Figure 4.2 TEM bright field images with corresponding SAED patterns of CeO₂ nanoparticles prepared at (a) 500 °C, (b) 600 °C, (c) 700 °C for 2h.

The UV-vis absorption spectra of the CeO₂ nanospheres are shown in Figure 4.3. All samples showed a strong absorption in the ultraviolet region centered at 285 nm (4.35 eV), close to the visible light region. The direct band gap energy (E_g) was determined by fitting the absorption data to the direct transition as equation 4.2,

$$\alpha hv = A(hv - E_g)^{1/2} \quad (4.2)$$

where α is the optical absorption coefficient, hv is the photon energy, E_g is the direct band gap, and A is a constant (Ziegler et al., 1981). The extrapolation of the linear portions of the curves toward absorption equal to zero ($y = 0$) gives E_g for direct transitions (see Figure 4.4). The estimated direct band gaps of all samples are shown in Table 4.2. We have observed that there is a decrease in the band gap with increasing calcination temperature.

The band edge absorption of nanometer-sized semiconductor materials is mainly related to two factors: a quantum size effect and a surface and interface effect. Generally, the quantum size effect leads to the blueshift of E_g with decrease of particle size down to less than a few nanometers, while the surface and interface effect induces the redshift (Barreca et al., 2003). In our work, since the crystallite size is in the range of 10 - 35 nm, the difference of the absorption band edge due to the quantum size effect is not observable. Obviously, the surface and interface effect should be responsible for the variation of the absorption band edge. Similar results have been obtained in some other systems Chen and Chang (2005) have reported direct band gap values ranging from 3.56 to 3.71 eV for CeO₂ nanoparticles synthesized by precipitation method. Maensiri et al. (2007) have reported direct band gap values ranging from 3.57 to 3.61 eV for CeO₂ nanoparticles synthesized by sol-gel method using egg white, due to the

quantum size effect (Tsunekawa et al., 2003). This behavior is interesting for the CeO₂-based nanospherical materials for efficient application in semiconductor devices.

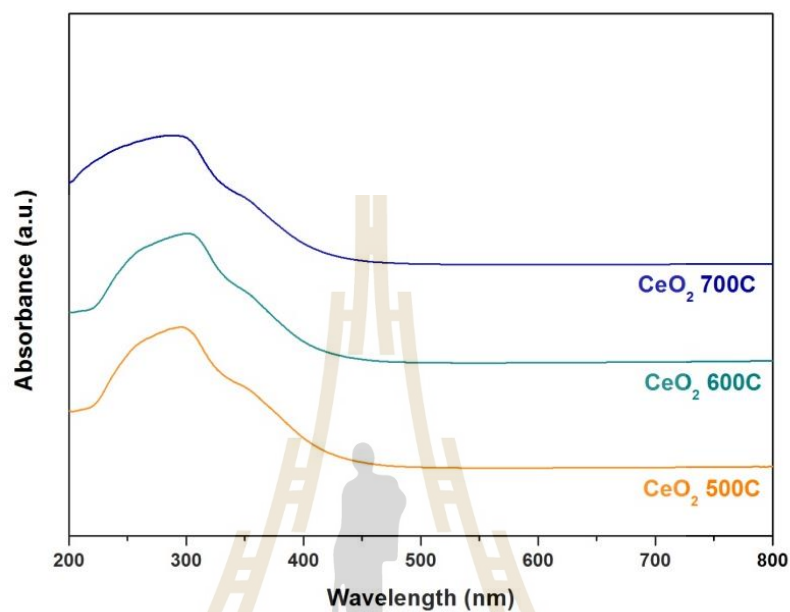


Figure 4.3 Room temperature optical absorbance spectra of the CeO₂ (a) calcined in air at 500, 600 and 700 °C for 2h.

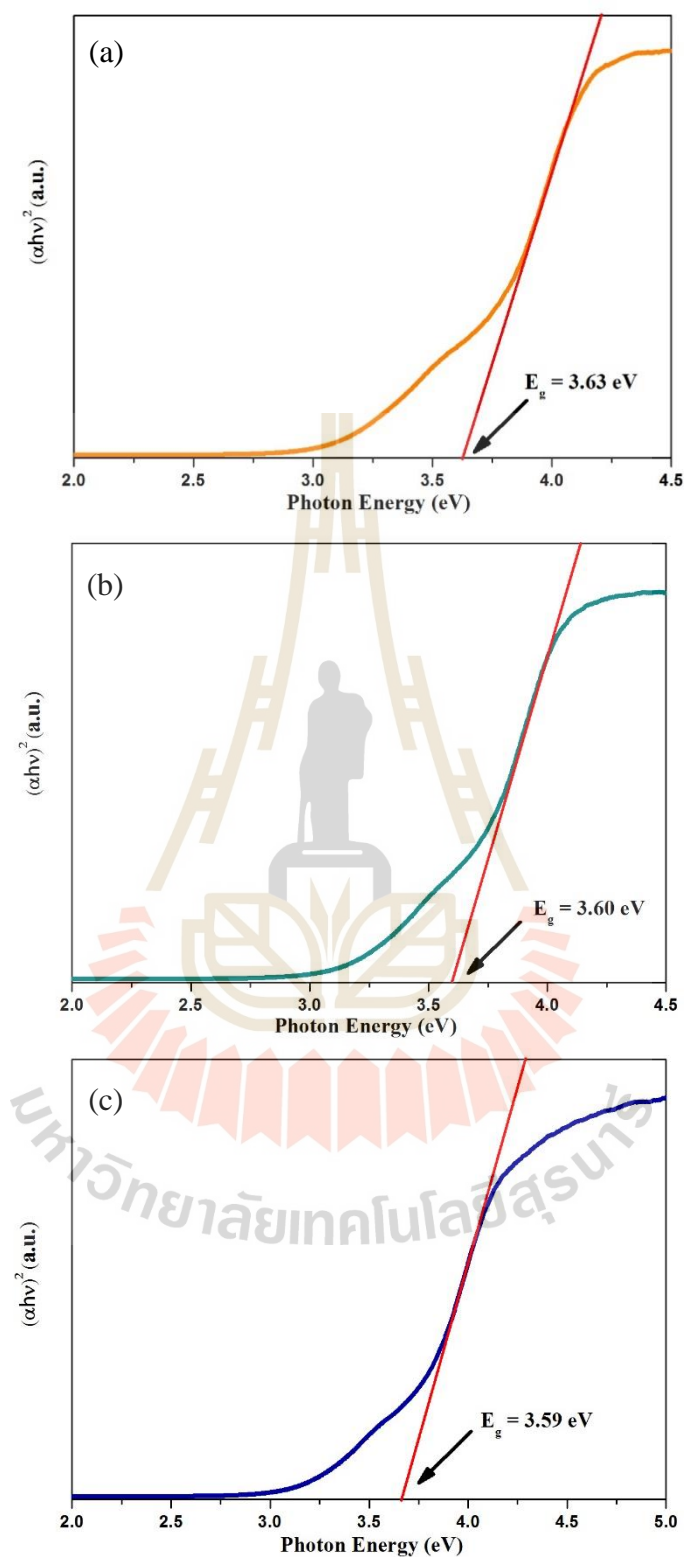


Figure 4.4 The correlated band gaps are 3.63, 3.60 and 3.59 eV for the CeO₂ samples calcined at 500 (b), 600 (c) and 700 °C (d), respectively.

For the CeO₂, a lower valent cation replaces a higher valence site by which creating V_O to account for the local charge balance (Janisch, Gopal, and Spaldin, 2005). Therefore, to confirm the formation of the V_O in all samples and valence state of CeO₂, XANES experiments were performed. The XANES spectra at Ce L₃ edge were measured in transmission mode, at the BL5 station. Figure 4.5 shows the edge energies of the Ce(NO₃)₃ (Ce³⁺) standard, CeO₂ (Ce⁴⁺) standard and CeO₂ samples at different calcined temperature prepared for 2h for comparison. The standard Ce(NO₃)₃ has a single peak illustrated by one intense white line at approximately 5728.8 eV represented with 2p4f¹5d_gL, where L denotes an oxygen ligand 2p hole. It is the characteristic of the Ce³⁺ valence state (Hormes et al., 2000). In the standard CeO₂, all the spectra are shifted to higher energies, and the white line is split into two peaks with nearly the same intensities at approximately 5732.8 and 5739.8 eV represented with 2p4f¹ 5d_{t_g} L and 2p4f⁰5d, no electron in the 4^f state, respectively, corresponding to the Ce⁴⁺ valence state (Hormes et al., 2000). The three Ce peak positions of all the samples are close to the values of the Ce(NO₃)₃ and CeO₂ standards. This result indicated that the Ce ions in our samples are in a mixed valence state of Ce³⁺ and Ce⁴⁺. The mixed percentage between Ce(NO₃)₃ and CeO₂ of samples were calculated by linear combination fitting of Athena program which (Figure 4.6-4.8) are also shown in Table 4.3. Daengsakul et al. reported, the semi-qualitative analysis of the valence state of Ce in each of samples was determined using an empirical calculation (Ou et al., 2010). These edge energies are consistent with coupling valence state of Ce³⁺ and Ce⁴⁺. The percentages of Ce³⁺ and Ce⁴⁺ of samples could be calculated form Eq. 4.3, 4.4 and 4.5.

$$(\text{Ce oxidation state}) = \left(4 \times \frac{\Delta E \text{ of samle}}{\Delta E \text{ of Ce}^{3+} \text{ and Ce}^{4+}}\right) + \left(3 \times \left(1 - \frac{\Delta E \text{ of sample}}{\Delta E \text{ of Ce}^{3+} \text{ and Ce}^{4+}}\right)\right) \quad (4.3)$$

$$\% \text{ of Ce}^{3+} = \left(1 - \frac{\Delta E \text{ of sample}}{\Delta E \text{ of Ce}^{3+} \text{ and Ce}^{4+}}\right) \times 100\% \quad (4.4)$$

$$\% \text{ of Ce}^{4+} = \left(\frac{\Delta E \text{ of sample}}{\Delta E \text{ of Ce}^{3+} \text{ and Ce}^{4+}}\right) \times 100\% \quad (4.5)$$

From these results, we can obtain the valence state of Ce atoms according to the edge energy shift position as shown in Table 4.4.

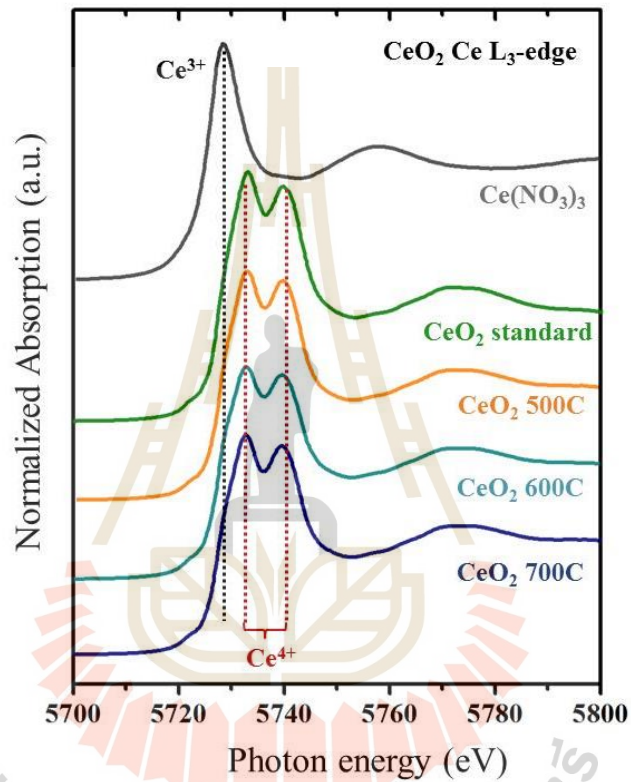


Figure 4.5 XANES spectra at the Ce L_3 absorption edge for $\text{Ce}(\text{NO}_3)_3$, CeO_2 standard and CeO_2 samples.

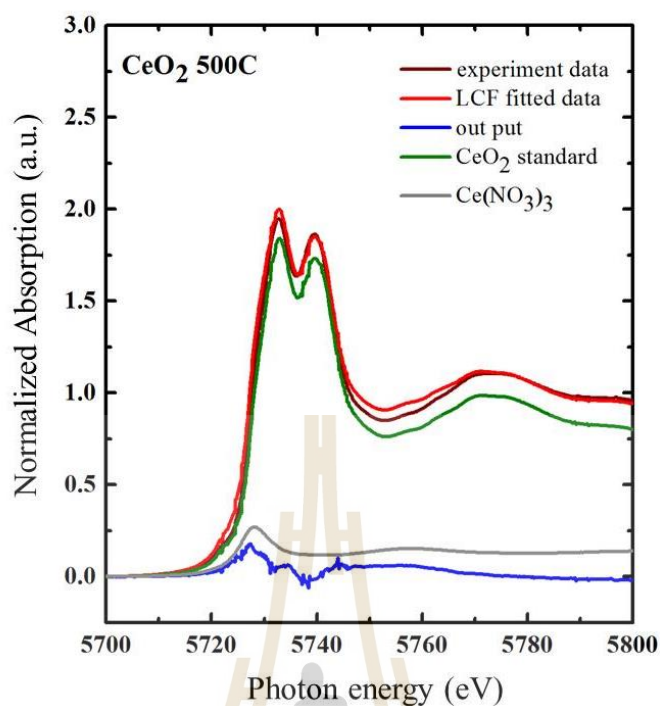


Figure 4.6 XANES spectra and linear combination fit of CeO₂ 500 °C, Ce(NO₃)₃/ CeO₂ standard reference metal and compound at L-edge.

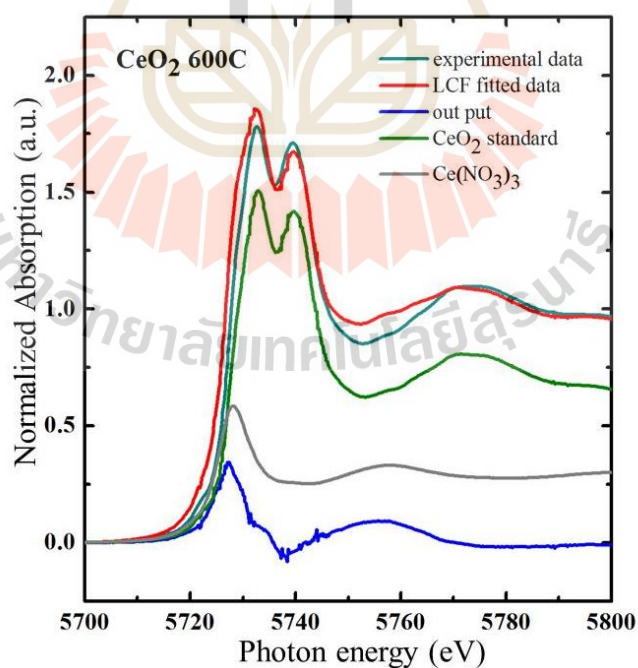


Figure 4.7 XANES spectra and linear combination fit of CeO₂ 600 °C, Ce(NO₃)₃/ CeO₂ standard reference metal and compound at L-edge.

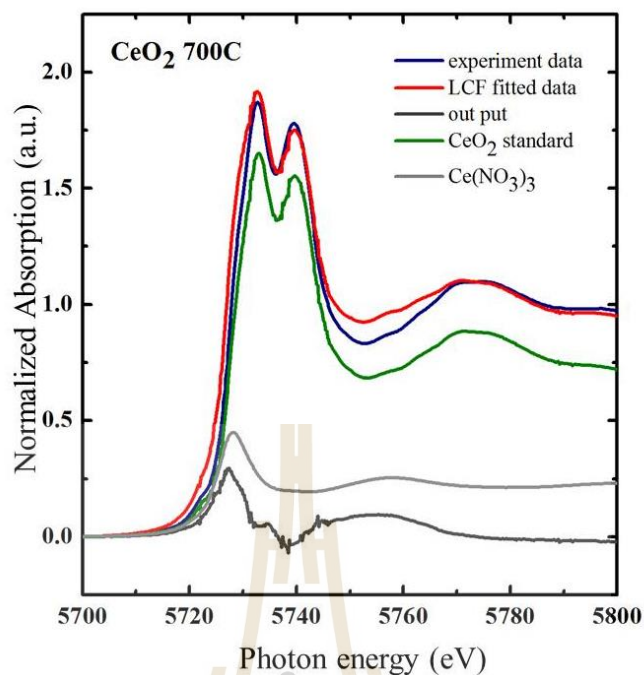


Figure 4.8 XANES spectra and linear combination fit of CeO_2 700 °C, $\text{Ce}(\text{NO}_3)_3/\text{CeO}_2$ standard reference metal and compound at L-edge.

Table 4.3 The mixed percentage between $\text{Ce}(\text{NO}_3)_3$ and CeO_2 of CeO_2 samples were calculated by linear combination fitting of Athena program.

Samples	Peak position (eV)	Percentage of $\text{Ce}(\text{NO}_3)_3$	Percentage of CeO_2	R factor values
500 °C	5727.36	12.4 %	87.6 %	0.0128
600 °C	5727.21	15.2 %	84.8 %	0.0149
700 °C	5726.80	13.2 %	86.8 %	0.0142

Table 4.4 Calculated valence state of Ce according to the edge energy shift positions of CeO₂ samples.

Samples	Peak position (eV)	ΔE of sample (eV)	Ce oxidation state	Percentage of Ce ³⁺	Percentage of Ce ⁴⁺
500 °C	5727.36	2.86	3.82	2.2 %	97.8 %
600 °C	5727.21	2.74	3.94	4.8 %	95.2 %
700 °C	5726.80	2.82	3.84	2.9 %	97.1 %

4.1.2 Magnetic properties of CeO₂ samples

Figure 4.9 shows the field dependence of the specific magnetization (M - H curve) of undoped CeO₂ samples, obtained from VSM measurements at RT. The magnetic component corresponding to the samples holder was subtracted from all the presented data. We observed diamagnetism in all calcined CeO₂ samples at an applied field of 10 kOe. The lowest specific magnetization value (M_s) was observed for CeO₂ calcined at 500 °C sample with value of approximately 0.0002 emu/g. Whereas, the highest specific magnetization value (M_s) was observed for CeO₂ calcined at 500 °C sample with value of approximately 0.000225 emu/g. This diamagnetism result is interesting because of the electrons of ionic charge Ce⁴⁺ are allied together to f⁰ induce net magnetic moment in the opposite direction to the external magnetic field. Therefore, this sample exhibits the diamagnetic behavior.

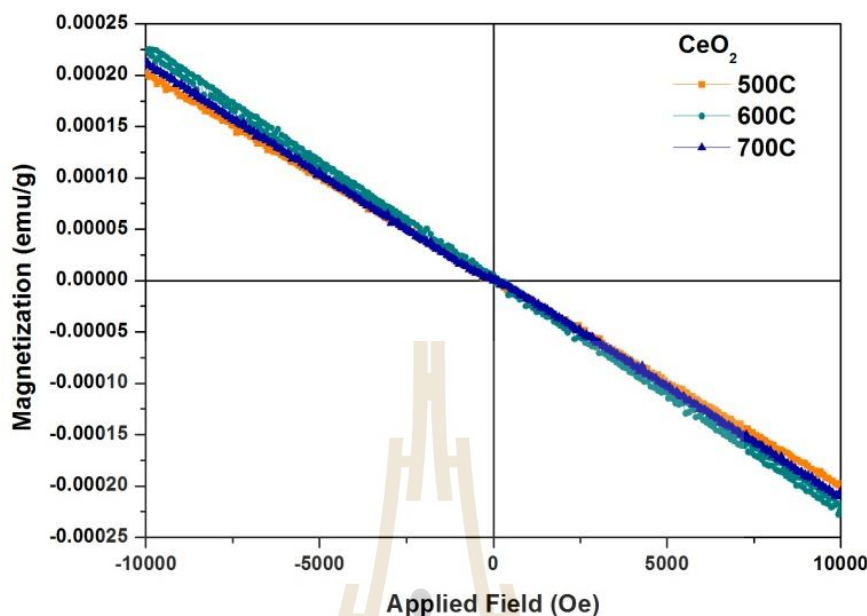


Figure 4.9 Magnetic properties of CeO₂ nanoparticles calcined at various temperatures for 2h in air.

4.2 Mn - doped CeO₂ nanoparticles

This part presented TM dopant type of Mn on structural characterization, morphology, absorption, and magnetic properties.

4.2.1 Structural characterization, morphology, and absorption of Mn-doped CeO₂ nanoparticles

TGA/DSC curves of the gel precursor in flowing air are shown in Figure 4.10. The TGA curve shows three steps of weight loss: the first weight loss step (~10 %) between ~ 50 and 200 °C, the second step (~ 8 %) between ~ 200 and 250 °C and the third step (~ 70 %) between ~ 250 and 550 °C. The first and second steps (50 - 250 °C) are related to the losses of moisture, trapped solvent (water and carbon dioxide) and nitrate, whereas the final weight loss (250 - 550 °C) is due to the combustion of organic

residues. Almost no weight loss could be observed above 550 °C suggesting the formation of crystalline CeO₂ as a decomposition product, as confirm by XRD result show in Figure 4.11. On the DSC curve of Figure 4.10, two peak of exothermic peaks were observed to have maximum at ~ 267 and ~ 450 °C, respectively. The sharp, strong exothermic peak at 450 °C confirms the combustion of organic residues, whereas another small exothermic peak at 267 °C with minor weight loss may be attributed to the losses of cerium nitrate.

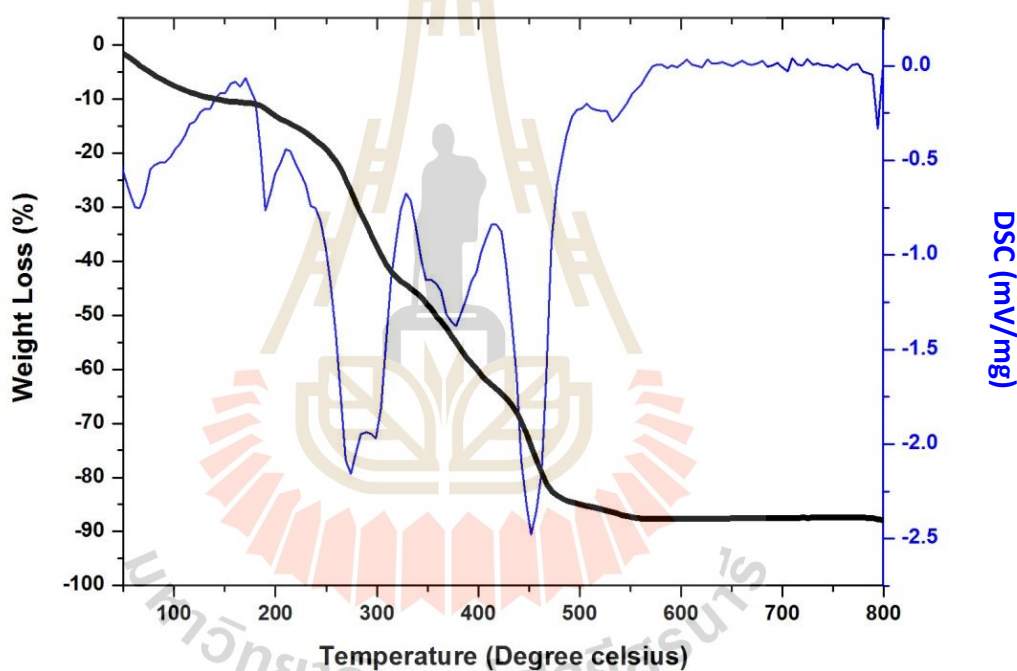


Figure 4.10 TGA/DSC curves of thermal decomposition of Mn-doped CeO₂ powder precursor at a heating rate of 10 °C/min in static air.

The XRD patterns of dried precursor and Mn-doped CeO₂ powders after calcination in air at 600 °C for 2h are shown Figure 4.11. The precursor sample shows no XRD peaks, indicating its amorphous nature, whereas the calcined samples exhibit XRD peaks, main peaks correspond to the (111), (200), (220), (311), (222), (400), (331)

and (420) planes, which are consistent with the face-center cubic fluorite structure of CeO_2 in the standard data form JCPDS 34-0394, and there are two secondary phases that are Mn_3O_4 , MnO_2 in the standard data JCPDS 1-086-2337 and JCPDS 44-0142, respectively. The values of crystallites of Mn-doped CeO_2 less than undoped CeO_2 , indicating that Mn ions might have been substituted into the CeO_2 lattice. The values of lattice parameter a of the samples calculated from the XRD spectra are shown in Table 4.5.

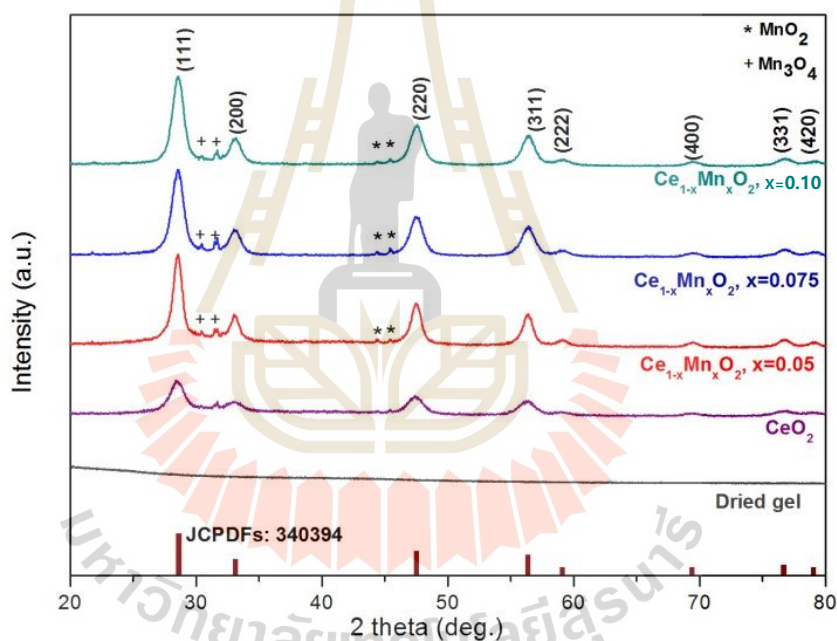


Figure 4.11 XRD patterns of CeO_2 and Mn-doped CeO_2 with content 0.05, 0.075 and 0.10 nanoparticles calcined in air at 600 °C.

Table 4.5 Summary of crystallite size and cubic lattice parameter of Mn-doped CeO₂ nanoparticles calcined in air at 600 °C.

Samples Ce_{1-x}Mn_xO₂	Crystallite sizes from XRD (nm)	Cubic lattice parameter, a (nm)
CeO ₂	21.7 ± 4.6	0.54146 ± 0.00017
x = 0.05	16.0 ± 3.2	0.53854 ± 0.00052
x = 0.075	16.7 ± 2.4	0.54065 ± 0.00096
x = 0.10	17.5 ± 4.3	0.53940 ± 0.00025

The lattice parameter change is possibly due to the replacement of larger Ce⁴⁺ ions by smaller Mn²⁺ or Mn³⁺ ions, introducing Ce³⁺ ions into the crystal lattice. Ce³⁺ have been a higher ionic radius compared to Ce⁴⁺, and these ions can introduce oxygen vacancies to achieve the charge balance in structure. It is observed that the distortion, which is in good agreement with earlier reports on the Mn-doped CeO₂ nanoparticles (Ge et al., 2008; Nagai et al., 2001). Those reports indicated that doping causes a change in the Ce-O bond length and the overall lattice parameter. The variations in intensity of peaks and lattice parameters can be attributed to the incorporation of the dopant in the crystal.

The morphology and structures of Mn-doped nanoparticles were investigated by TEM as shown in Figure 4.12 and SEM as shown in Figure 4.13. TEM bright field images show that the samples are thin platelike structure which consist of networked nanocrystalline particles with particle size of 15 - 35 nm. (see summary particle sizes from TEM in Table 4.6). The average particle size is nearly crystallite size obtain from XRD patterns. Measured interplanar spacing (d_{hkl}) from SAED patterns inset Figure

4.12 are in good agreement with the values in standard data JCPDS 34-0394, which is in agreement with XRD result. The high-resolution TEM images (inset Figure 4.12) reveal the details of Mn-doped CeO₂ nanoparticles with the measured spacing of the lattice fringes of ~ 0.29-0.32 nm corresponding to the (111) plane. These are in agreement with the standard data JCPDS 34-0394.

Table 4.6 Particle sizes from TEM bright field images and E_g from UV-vis spectra of Mn-doped CeO₂ calcined samples.

Samples	Particle sizes	Band gap E_g
Ce_{1-x}Mn_xO₂	from TEM (nm)	(eV)
CeO ₂	15 - 30	3.60
x = 0.05	15 - 20	3.50
x = 0.075	20 - 35	3.53
x = 0.10	10 - 15	3.61

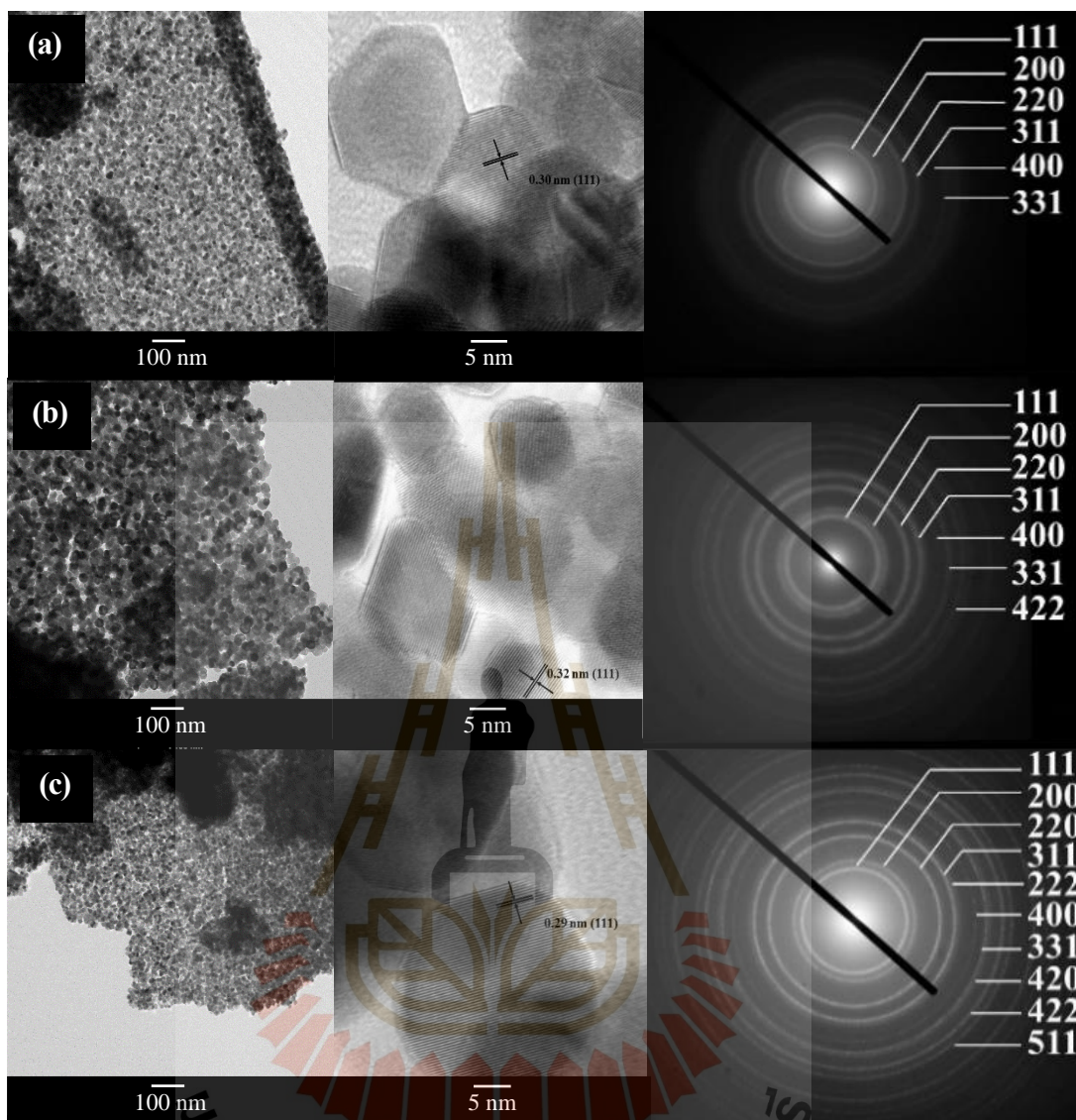


Figure 4.12 TEM and HRTEM bright field images with corresponding SAED patterns of the $\text{Ce}_{1-x}\text{Mn}_x\text{O}_2$ ($x = 0.05$ (a), $x = 0.075$ (b), $x = 0.10$ (c)) samples calcined in air at $600\text{ }^\circ\text{C}$ for 2h.

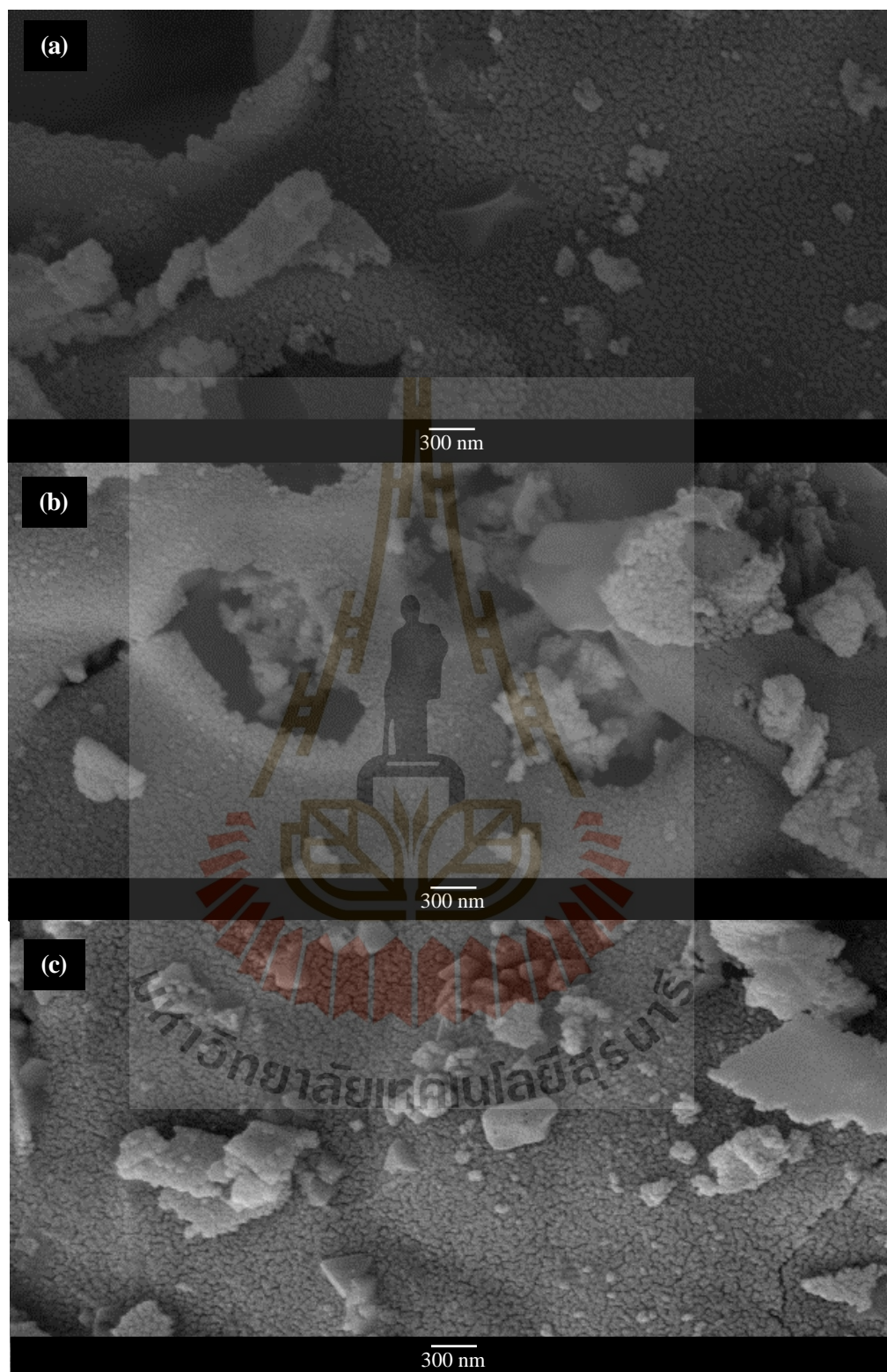


Figure 4.13 SEM images of $\text{Ce}_{1-x}\text{Mn}_x\text{O}_2$ ($x = 0.05$ (a), $x = 0.075$ (b), $x = 0.10$ (c)) calcined in air at $600\text{ }^\circ\text{C}$ for 2h.

The UV-visible absorption spectra of the pure CeO_2 and Mn-doped CeO_2 samples are shown in Figure 4.14. All samples show a strong absorption below 400 nm (3.10 eV) with a well-defined absorbance peak at approximately 285 nm (4.35 eV). The band gap can be determined by fitting the absorption data to the direct transition equation by extrapolating of the linear portions of the curves to absorption equal to zero (Figure 4.15(a-d)).

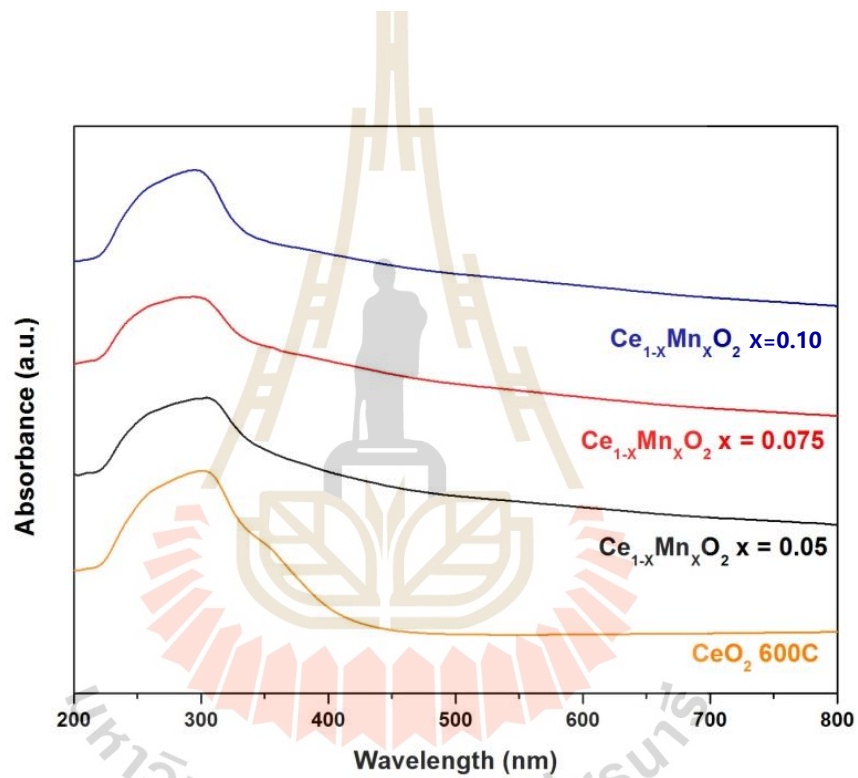


Figure 4.14 Room temperature optical absorbance spectra of CeO_2 and $\text{Ce}_{1-x}\text{Mn}_x\text{O}_2$ ($x = 0.05$, $x = 0.075$, $x = 0.10$) samples calcined in air at 600 °C for 2h.

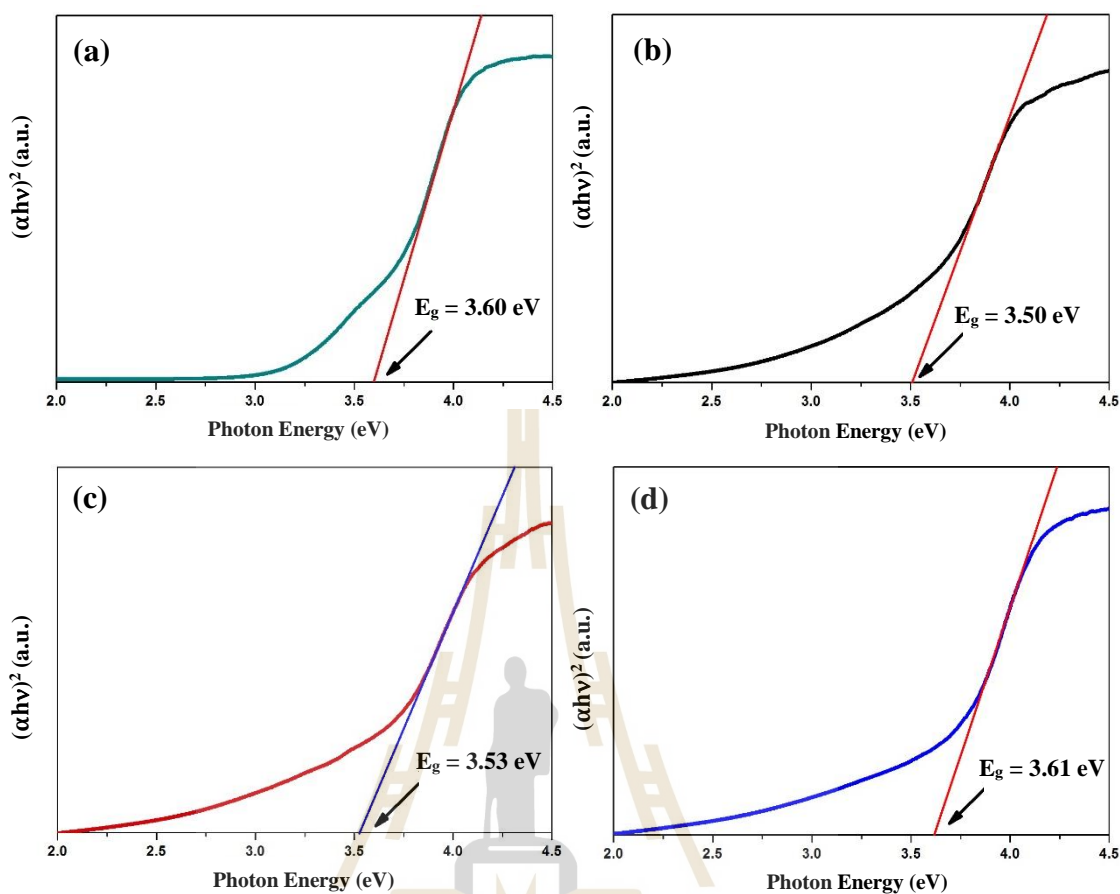


Figure 4.15 The correlated band gaps are 3.60, 3.50, 3.53 and 3.61 eV for the CeO_2 (a) and $\text{Ce}_{1-x}\text{Mn}_x\text{O}_2$ ($x = 0.05$ (b), $x = 0.075$ (c), $x = 0.10$ (d)), respectively.

The estimated direct band gaps of all samples are shown in Table 4.6. We have observed that there is an increase in the band gap with increasing Mn content calculated for Mn-doped CeO_2 prepared at 600 °C for 2h, which exhibit blue shifts in the absorption spectra. The band gap E_g energy shows blue shifts of 3.50, 3.53 and 3.61 eV for samples with Mn content 0.05, 0.075 and 0.10, respectively, compared to that of the pure CeO_2 nanoparticles.

The band gap of CeO_2 reported in this work is lower than that reported in the literature. Chen and Chang reported direct band gap values ranging from 3.56 to 3.71

eV for CeO₂ nanoparticles synthesized by the precipitation method (Ohno et al., 1998). Masui et al. reported the band gaps of 4.1 and 2.6 nm of CeO₂ nanoparticle prepared using reverse micelles to be 3.38 and 3.44 eV, respectively (Ohno et al., 2000). Meansiri et al. have reported direct band gap values of 3.57 to 3.61 eV for CeO₂ nanoparticles prepared by egg whites (Maensiri et al., 2009), due to quantum confinement effect (Ohno et al., 2002). This phenomenon has been well explained for particle sizes down to less than a few nanometers, but for our results, the band gap values increased with increasing crystal size, which exhibit blue shifts in UV absorption spectra inferred from the band gap calculated for Mn-doped CeO₂ nanoparticles. This blueshift has been reported to be an electrostatic potential effect due to a cerium valence change when the particle size is larger than a few nanometers (e.g., ≤ 8 nm). The Ce⁴⁺ ions coexist with Ce³⁺ ions, and these ions can be attributed to oxygen vacancies at the surface (Oiwa et al., 2001). Therefore, in our work, the band gaps increased with increasing crystal size. The crystallite size is in the range of 16.0 to 17.5 nm as indicated by the existence of the blue shift for our Mn-doped CeO₂ samples.

The valence state of Ce ions in undoped CeO₂ and Mn-doped CeO₂ nanoparticles and valence state of Mn ions were determined by XANES. The XANES spectra at Ce L₃ edge were measured in transmission mode, and the Mn K edge XANES spectra of the samples were measured in fluorescent mode at RT at BL5.2 station. Figure 4.16 shows the edge energies comparison of the Ce(NO₃)₃(Ce³⁺) standard, CeO₂ (Ce⁴⁺) standard, pure CeO₂ sample and Mn-doped CeO₂ samples. The edge energies are found at 5727.21, 5727.8, 5728.1 and 5727.4 eV for pure CeO₂ sample and Mn-doped with content 0.05, 0.075 and 0.10, respectively. This result indicated that the valence state of Ce ions in samples are a mixed valence state of Ce³⁺ and Ce⁴⁺ ions. The

mixed percentage between $\text{Ce}(\text{NO}_3)_3$ and CeO_2 in samples were calculated by linear combination fitting of Athena program (Figure 4.17 - 4.19) are also shown in Table 4.7. The percentages of Ce^{3+} and Ce^{4+} of samples could be calculated from Eq. 4.3, 4.4 and 4.5. From these results, we can obtain the valence state of Ce atoms according to the edge energy shift position as shown in Table 4.8.

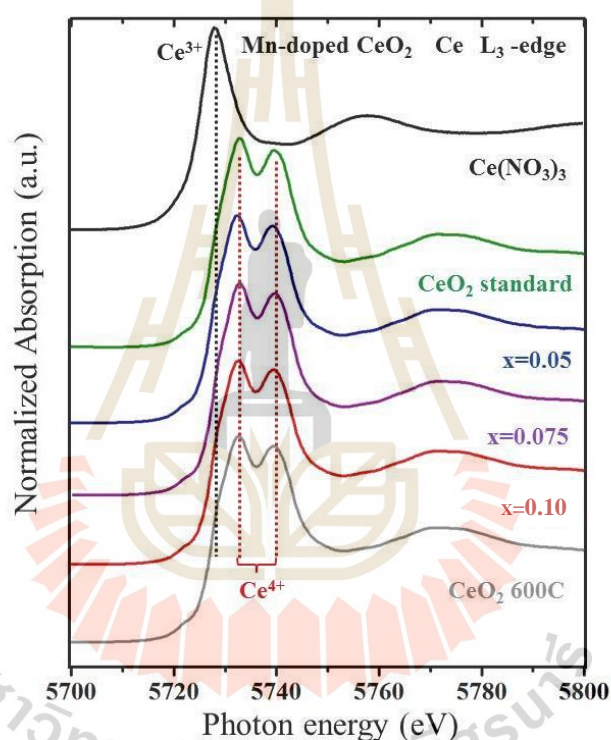


Figure 4.16 XANES spectra at Ce L_3 absorption edge for CeO_2 , Cerium nitrate standard and XANES spectra of CeO_2 , Mn-doped CeO_2 samples.

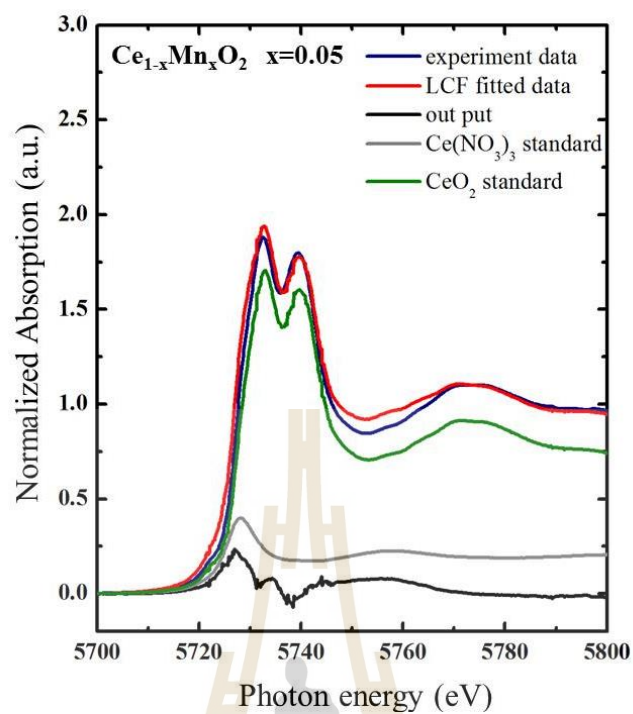


Figure 4.17 XANES spectra and linear combination fit of Mn-doped CeO_2 $x = 0.05$, $\text{Ce}(\text{NO}_3)_3/\text{CeO}_2$ standard.

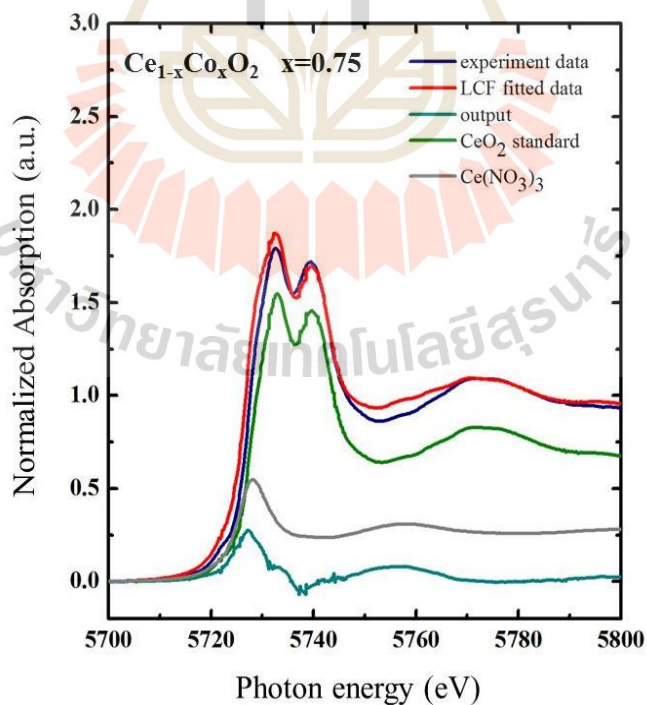


Figure 4.18 XANES spectra and linear combination fit of Mn-doped CeO_2 $x = 0.075$, $\text{Ce}(\text{NO}_3)_3/\text{CeO}_2$ standard.

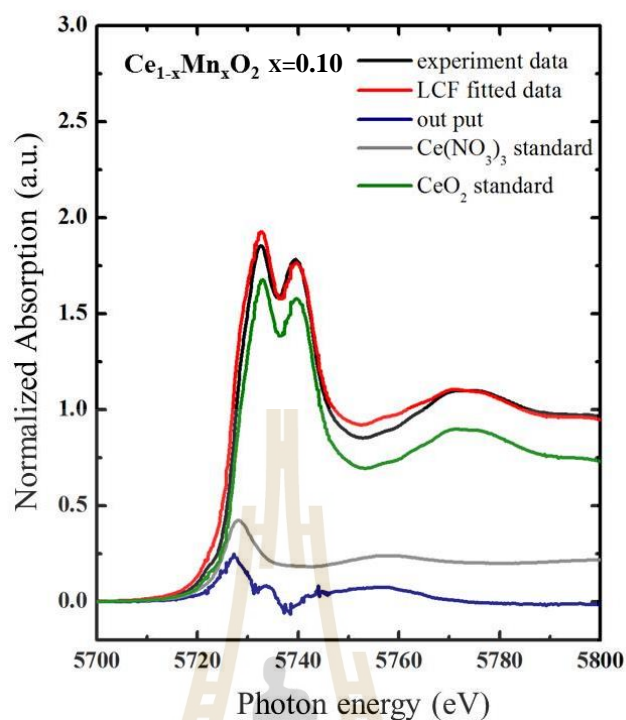


Figure 4.19 XANES spectra and linear combination fit of Mn-doped CeO_2 $x = 0.10$, $\text{Ce}(\text{NO}_3)_3/\text{CeO}_2$ standard.

Table 4.7 The mixed percentage between $\text{Ce}(\text{NO}_3)_3$ and CeO_2 standard of Mn-doped CeO_2 samples were calculated by linear combination fitting of Athena program.

Samples	Peak	Percentage	Percentage	R factor
$\text{Ce}_{1-x}\text{Mn}_x\text{O}_2$	position (eV)	of $\text{Ce}(\text{NO}_3)_3$	of CeO_2	values
$x = 0.00$	5727.21	15.2 %	84.8 %	0.0149
$x = 0.05$	5727.8	3.4 %	96.6 %	0.016
$x = 0.075$	5728.1	4.8 %	95.2 %	0.014
$x = 0.10$	5727.4	5.2 %	94.8 %	0.020

Table 4.8 Calculated valence state of Ce according to the edge energy shift positions of Mn-doped CeO₂ samples.

Samples	Peak	ΔE of	Ce	Percentage	Percentage
Ce _{1-x} Mn _x O ₂	position (eV)	sample	oxidation	of Ce ³⁺	of Ce ⁴⁺
		(eV)	state		
x = 0.00	5727.21	2.74	3.94	4.8 %	95.2 %
x = 0.05	5727.8	2.79	3.24	1.2 %	98.8 %
x = 0.075	5728.1	2.53	3.78	1.8 %	98.2 %
x = 0.10	5727.4	2.60	3.04	2.8 %	97.2 %

It is observed that the highest percentage of Ce³⁺ is 2.8 % for Mn-doped CeO₂ sample with content 0.10.

Figure 4.20 shows the K-edge energies of Mn₃O₄ (Mn²⁺ and Mn³⁺) standard, MnO₂ (Mn⁴⁺) standard and Mn-doped CeO₂ samples at different concentrations for comparison. The edge energies imply a coupling of MnO₂ and Mn₃O₄ in samples. The mixed percentage between MnO₂ and Mn₃O₄ of samples were calculated by linear combination fitting of Athena program (Figure 4.21 - 4.23) are also shown in Table 4.9. Similarly, with the Eq. 4.3, 4.4 and 4.5, we could be calculated the percentages of Mn²⁺, Mn³⁺ and Mn⁴⁺ of samples. From these results, we can obtain the mixed valence states of Mn atoms and edge energy values are also shown in Table 4.10.

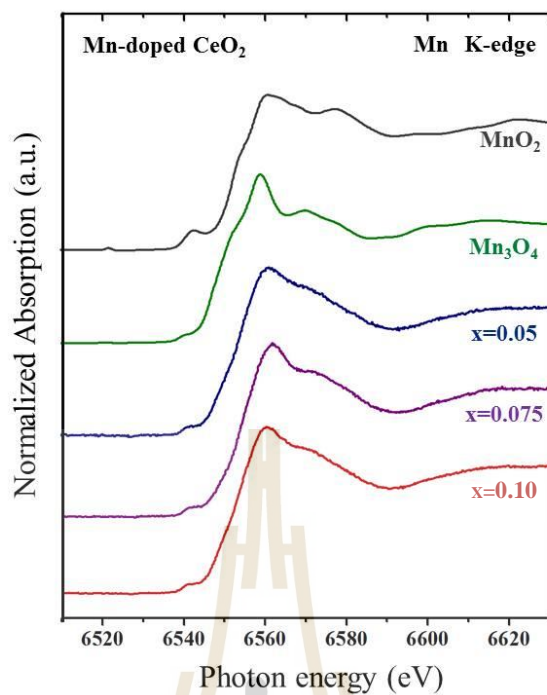


Figure 4.20 XANES spectra at Mn K absorption edge for Mn₃O₄, MnO₂ standard and XANES spectra of Mn-doped CeO₂ nanoparticles samples.

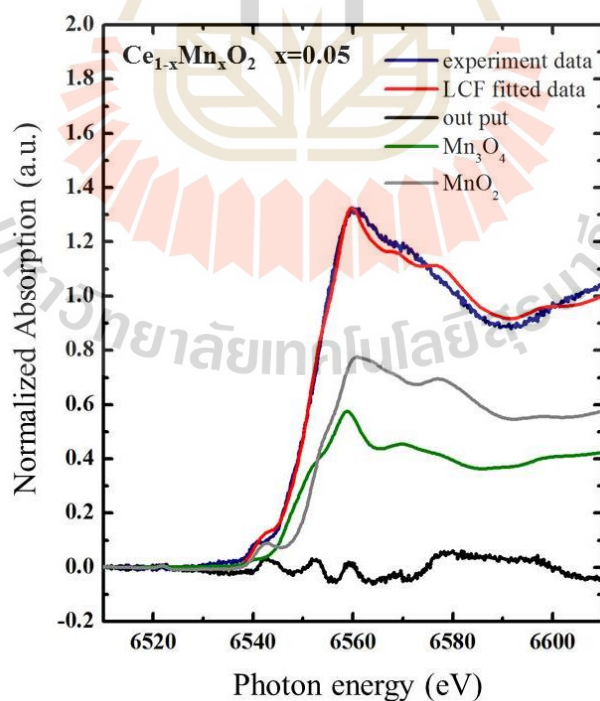


Figure 4.21 XANES spectra and linear combination fit of Mn-doped CeO₂ x = 0.05, Mn₃O₄/ MnO₂, reference metal and compound at K-edge.

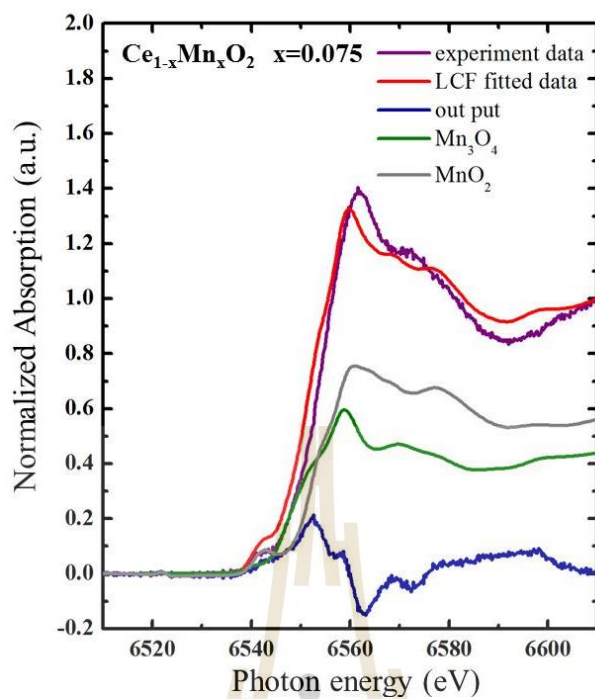


Figure 4.22 XANES spectra and linear combination fit of Mn-doped CeO₂ x = 0.075, Mn₃O₄/ MnO₂, reference metal and compound at K-edge.

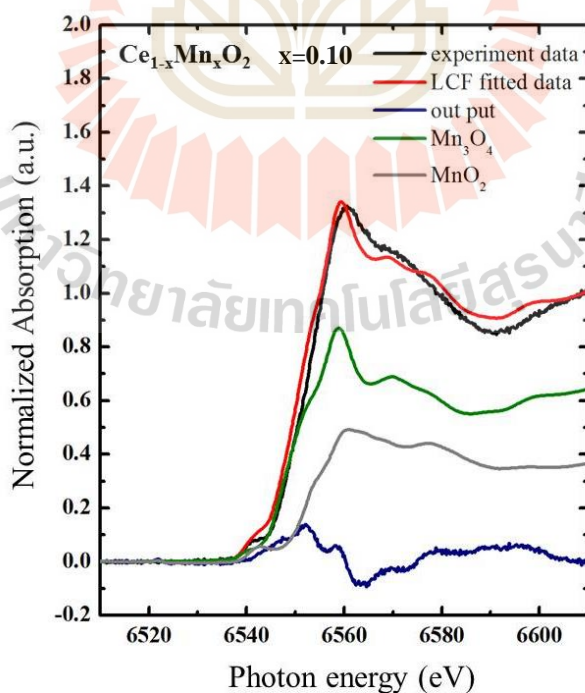


Figure 4.23 XANES spectra and linear combination fit of Mn-doped CeO₂ x = 0.10, Mn₃O₄/ MnO₂, reference metal and compound at K-edge.

Table 4.9 The mixed percentage between Mn_3O_4 and MnO_2 of Mn-doped CeO_2 samples were calculated by linear combination fitting of Athena program.

Samples	Peak	Percentage	Percentage	R factor
$\text{Ce}_{1-x}\text{Mn}_x\text{O}_2$	position (eV)	of MnO_2	of Mn_3O_4	values
x = 0.05	6549.0	66.3 %	33.7 %	0.008
x = 0.075	6551.2	65.6 %	34.4 %	0.010
x = 0.10	6550.6	41.6 %	58.4 %	0.005

Table 4.10 Calculated valence state of Mn according to the edge energy shift positions of Mn-doped CeO_2 samples.

Samples	Peak	ΔE of	Mn	Percentage	Percentage	Percentage
$\text{Ce}_{1-x}\text{Mn}_x\text{O}_2$	position (eV)	sample (eV)	oxidation state	of Mn^{2+}	of Mn^{3+}	of Mn^{4+}
x = 0.05	6549.0	3.32	3.24	12.2 %	30.1 %	58.7 %
x = 0.075	6551.2	3.44	3.78	5.4 %	34.2 %	60.4 %
x = 0.10	6550.6	3.15	3.04	16.8 %	40.4 %	42.8 %

The highest percentage of Mn^{3+} are approximate 40.4 % in Mn-doped CeO_2 with content 0.10.

4.2.2 Magnetic properties of Mn-doped CeO_2 nanoparticles

Magnetic behavior of Mn-doped CeO_2 nanoparticles has been studied using field cooled (FC) magnetization and magnetic hysteresis loop measurements. Figure 4.24 shows typical magnetization (M) versus field curves of Mn-doped CeO_2

with different concentration nanoparticles measured at RT. All samples exhibit behaviors of weak ferromagnetism and paramagnetism having small hysteresis loops at low field (inset Figure 4.24).

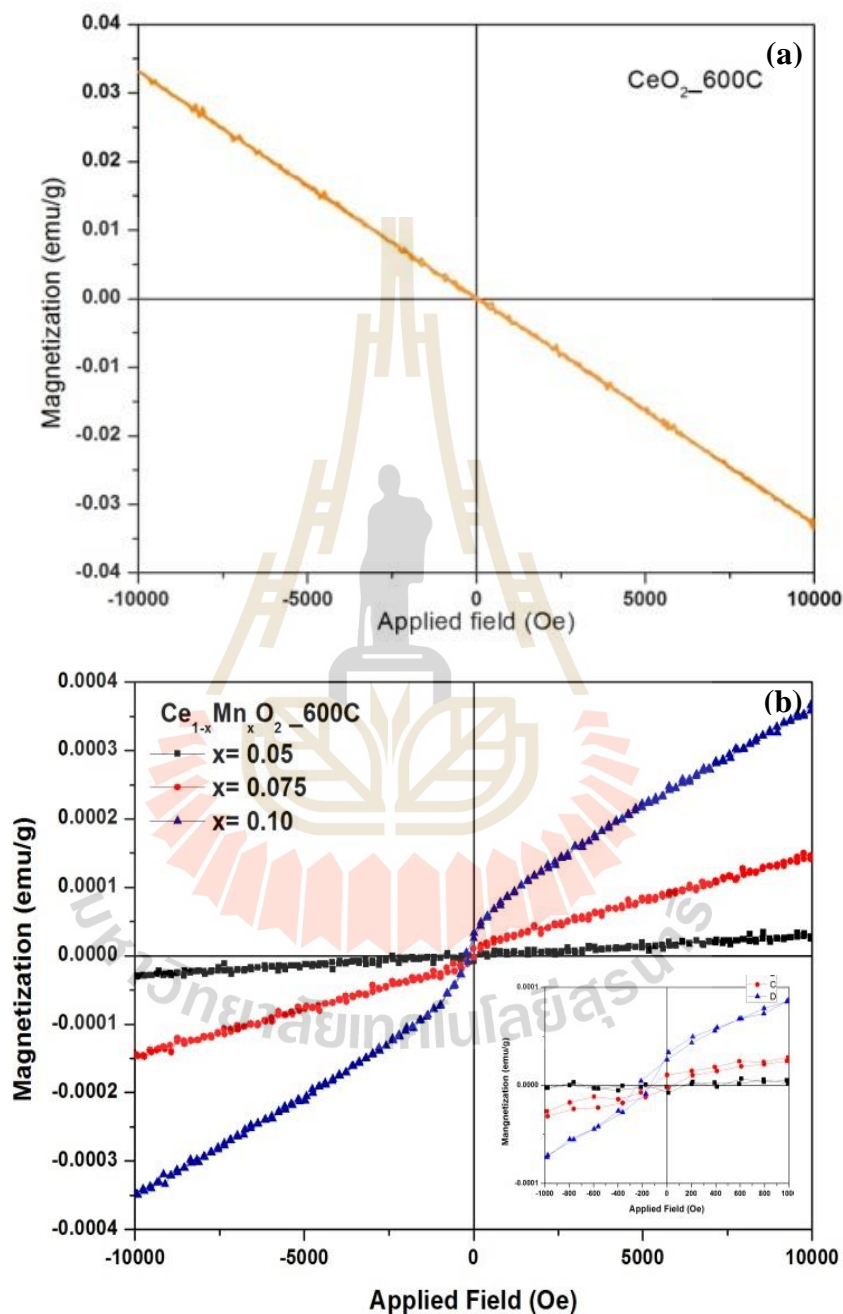


Figure 4.24 Magnetic properties of CeO_2 (a) and Mn-doped CeO_2 (b) nanoparticles calcined at various temperatures for 2h in air at 600 °C.

The samples that were prepared with different concentration of 0.05, 0.075 and 0.10 are showed weak RT-FM with saturation magnetization (M_s) of approximately 0.00003, 0.00015 and 0.00035 emu/g, respectively (as shown listed in Table 4.11).

Table 4.11 Summary of magnetization (M) of CeO₂ and Mn-doped CeO₂ nanoparticles calcined at 600 °C for 2h.

Samples Ce _{1-x} Mn _x O ₂	M at 10 kOe (emu/g)
CeO ₂	diamagnetic
x = 0.05	0.00003
x = 0.075	0.00015
x = 0.10	0.00035

To explain the origin of ferromagnetic contribution in the Mn-doped CeO₂ nanoparticles, it is worth nothing that cerium can have both variable valence state (Ce³⁺ and Ce⁴⁺) and oxygen vacancies on the surface of the CeO₂ nanoparticles. It is possible that oxygen vacancies can create magnetic moments on neighboring Ce ions (Pearton et al., 2004). In our work, ferromagnetic possibly due to the replacement of lager Ce⁴⁺ by smaller Mn³⁺ and Mn⁴⁺. The calcination with high temperature (600 °C) could possibly increase the number of oxygen vacancies and Ce³⁺ ions in the samples. The magnetic properties were also performed to confirm the effect of oxygen vacancies. The observed ferromagnetism can be explained by FCE (Coey, 2005; Paula et al., 2010; Patterson et al., 2005; Pearton et al., 2003). The XANES spectra show the evidence of Mn³⁺ and Mn⁴⁺ substitution in CeO₂, and the Ce ions of 3+ state (with 4f¹

configuration), which can be attributed to V_O in Mn-doped CeO_2 samples. Therefore, the ferromagnetic in these samples was suggested according to the FCE of Mn^{3+} - V_O - Mn^{4+} (see in Figure 4.25) complex in the structure.

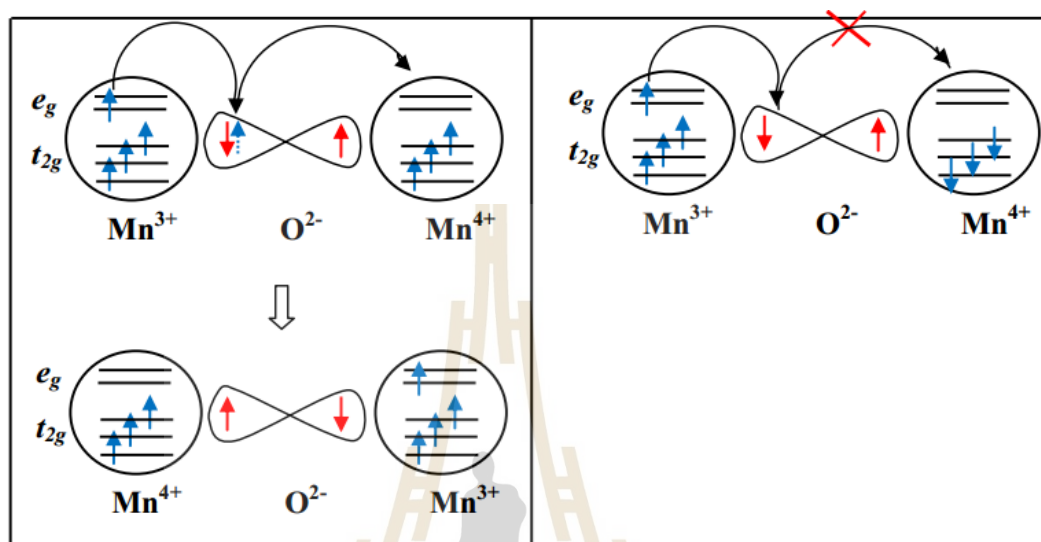


Figure 4.25 Ferromagnetic coupling of nearby Mn^{3+} - O - Mn^{4+} ions via double exchange interaction (Anderson, 1950).

This FCE forms BMP and neighboring BMPs can overlap and result in the long-rang Mn-Mn ferromagnetic coupling in CeO_2 . Moreover, we believe that the origin of ferromagnetism in Mn-doped CeO_2 nanoparticles is due to Mn^{3+} and Mn^{4+} substitution in CeO_2 and oxygen vacancies.

4.3 Co-doped CeO_2 nanoparticles

This part presents the TM-dopant type of Co on structural characterization, morphology, absorption and magnetic properties.

4.3.1 Structural characterization, morphology, and absorption of Co-doped CeO₂ nanoparticles

The simultaneous TGA/DSC curves of the gel precursor in flowing air are shown in Figure 4.26. The TGA curve shows three steps of weight loss: the first weight loss step (~ 10 %) between ~ 50 and 200 °C, the second step (~ 8 %) between ~ 200 and 250 °C and the third step (~ 70 %) between ~ 250 and 550 °C. The first and second steps (50 - 250 °C) are related to the losses of moisture, trapped solvent (water and carbon dioxide) and nitrate, whereas the final weight loss (250 - 550 °C) is due to the combustion of organic residues. Almost no weight loss could be observed above 550 °C, suggesting the formation of crystalline CeO₂ as a decomposition product, as confirm by XRD result show in Figure 4.27. On the DSC curve of Figure 4.25, two peak of exothermic peaks were observed to have maximum at ~ 295 and ~ 475 °C, respectively. The sharp, strong exothermic peak at 450 °C confirms the combustion of organic residues, whereas another small exothermic peak at 267 °C with minor weight loss may be attributed to the losses of cerium nitrate.

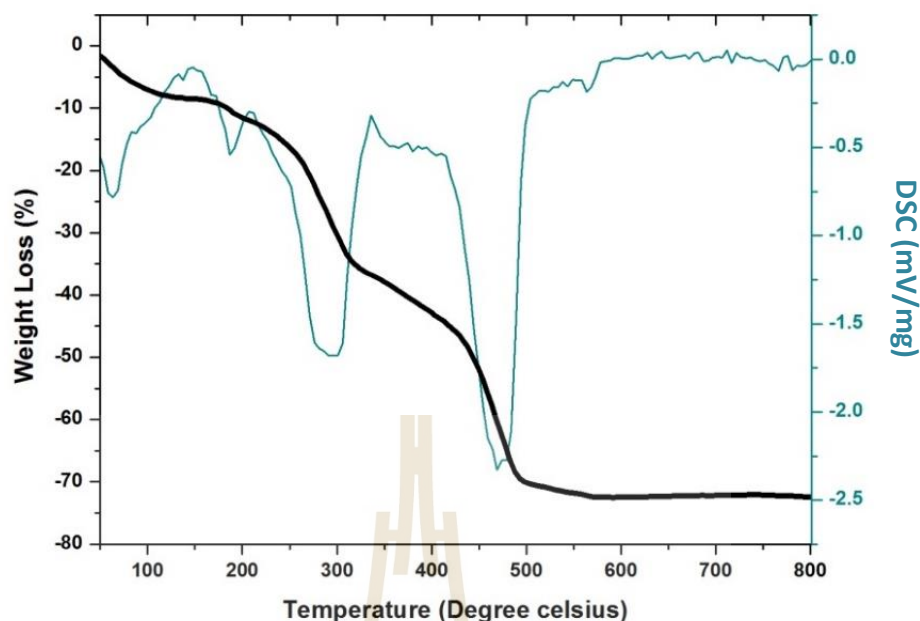


Figure 4.26 TGA/DSC curves of thermal decomposition of Co-doped CeO₂ powder precursor at a heating rate of 10 °C/min in static air.

The XRD patterns of dried precursor and Co-doped CeO₂ powders after calcination in air at 600 °C for 2h are shown Figure 4.27. The precursor sample shows no XRD peaks, indicating its amorphous nature, whereas the calcined samples exhibit XRD peaks, main peaks correspond to the (111), (200), (220), (311), (222), (400), (331) and (420) planes, which are consistent with the face-center cubic fluorite structure of CeO₂ in the standard data form JCPDS 34-0394, and there are two secondary phases that are Co₃O₄ and Co(NO₃)₂ in the standard data JCPDS 1-086-2337 and JCPDS 44-0142, respectively. The values of crystallites of Co-doped CeO₂ less than undoped CeO₂, indicating that Co ions might have been substituted into the CeO₂ lattice. The values of lattice parameter *a* of all the samples calculated from the XRD spectra are shown in Table 4.12.

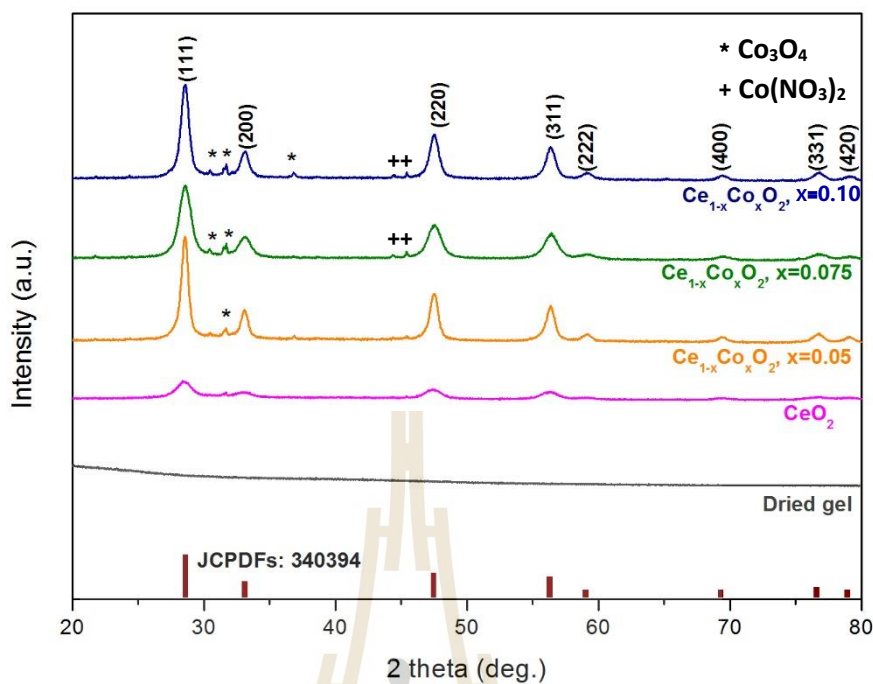


Figure 4.27 XRD patterns of CeO_2 and Co-doped CeO_2 with content 0.05, 0.075 and 0.10 nanoparticles calcined for in air at $600\text{ }^\circ\text{C}$.

Table 4.12 Summary of crystallite size and cubic lattice parameter of Co-doped CeO_2 nanoparticles calcined in air at $600\text{ }^\circ\text{C}$.

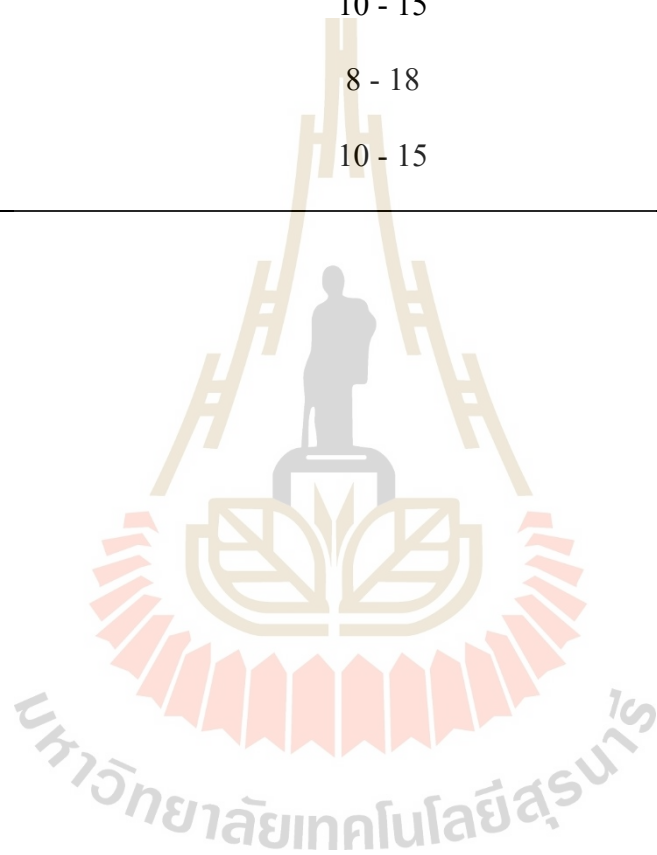
Samples	Crystallite sizes	Cubic lattice parameter, a
$\text{Ce}_{1-x}\text{Co}_x\text{O}_2$	from XRD (nm)	(nm)
CeO_2	21.7 ± 4.6	0.54146 ± 0.00017
$x = 0.05$	23.0 ± 4.0	0.53835 ± 0.00014
$x = 0.075$	12.7 ± 2.2	0.54065 ± 0.00035
$x = 0.10$	19.4 ± 3.6	0.53151 ± 0.00026

The lattice parameter change is possibly due to the replacement of larger Ce^{4+} ions by smaller Co^{2+} ions or Co^{3+} ions, introducing Ce^{3+} ions into the crystal lattice. Ce^{3+} ions have a higher ionic radius compared with Ce^{4+} ions, and these ions introduce oxygen vacancies. It is observed that the distortion, which is in good agreement with earlier reports on the Mn-doped CeO_2 nanoparticles (Ge et al., 2008; Nagai et al., 2001). Those reports indicated that doping causes a change in the Ce-O bond length and the overall lattice parameter. The variations in intensity of peaks and lattice parameters can be attributed to the incorporation of the dopant in the crystal.

The morphology and structures of Co-doped nanoparticles were investigated by TEM as shown in Figure 4.28 and SEM as shown in Figure 4.29. TEM bright field images show that the samples are thin platelike structure which consist of networked nanocrystalline particles with particle size of 8-18 nm. (see summary particle sizes from TEM in Table 4.13). The average particle size is nearly crystallite size obtain from XRD patterns. Measured interplanar spacing (d_{hkl}) from SAED inset Figure 4.28 are in good agreement with the values in standard data JCPDS 34-0394, which is in agreement with XRD result. The high-resolution TEM images (inset Figure 4.28) reveal the details of Co-doped CeO_2 nanoparticles with the measured spacing of the lattice fringes of ~ 0.29 - 0.32 nm corresponding to the (111) plane. These are in agreement with the standard data JCPDS 34-0394.

Table 4.13 Particle sizes from TEM bright field images and E_g from UV-vis spectra of Co-doped CeO_2 calcined samples.

Samples $\text{Ce}_{1-x}\text{Co}_x\text{O}_2$	Particle sizes from TEM (nm)	Band gap E_g (eV)
CeO_2	15 - 30	3.60
x = 0.05	10 - 15	3.45
x = 0.075	8 - 18	3.52
x = 0.10	10 - 15	3.57



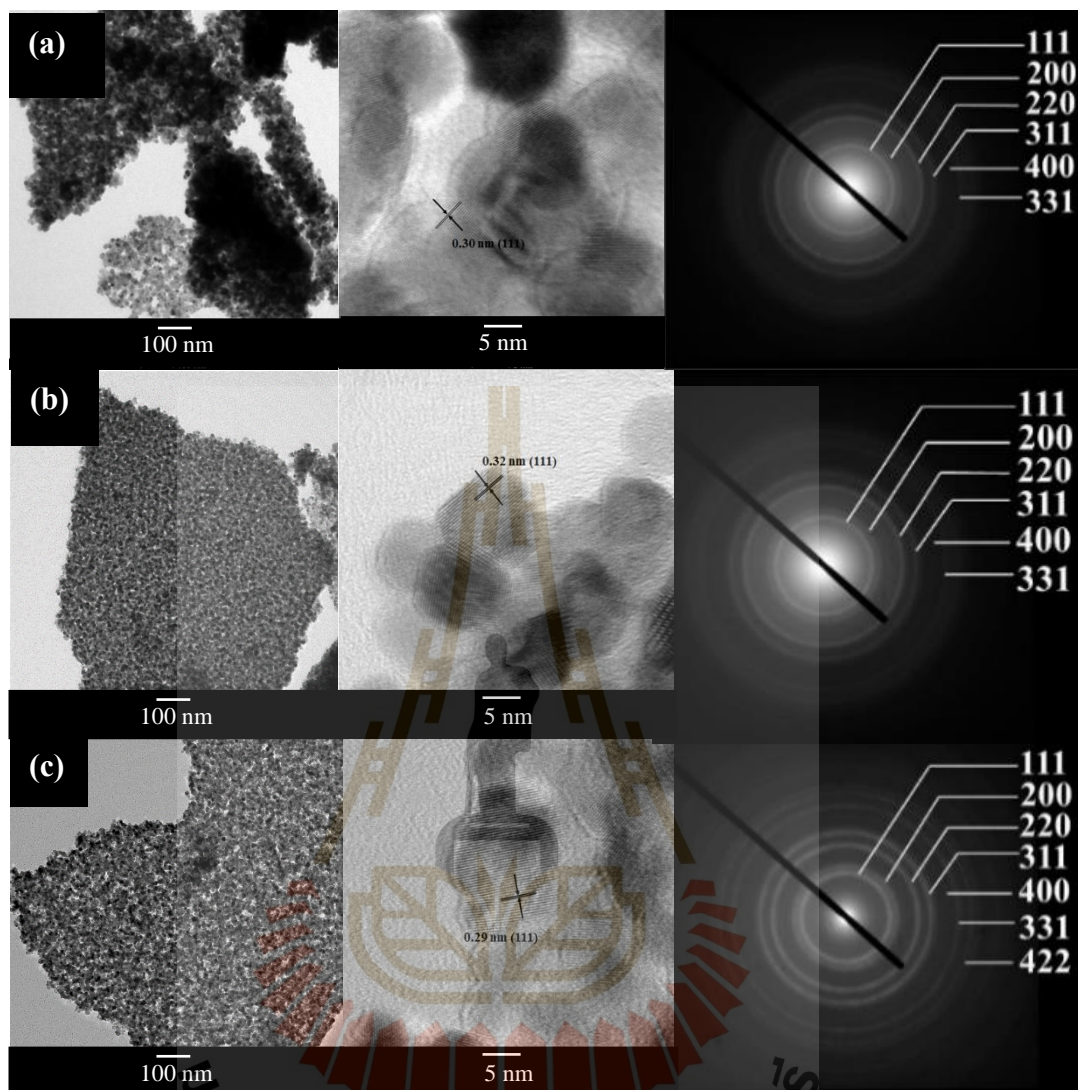


Figure 4.28 TEM and HRTEM bright field images with SAED patterns of the $\text{Ce}_{1-x}\text{Co}_x\text{O}_2$ ($x = 0.05$ (a), $x = 0.075$ (b), $x = 0.10$ (c)) samples calcined in air at $600\text{ }^\circ\text{C}$ for 2h.

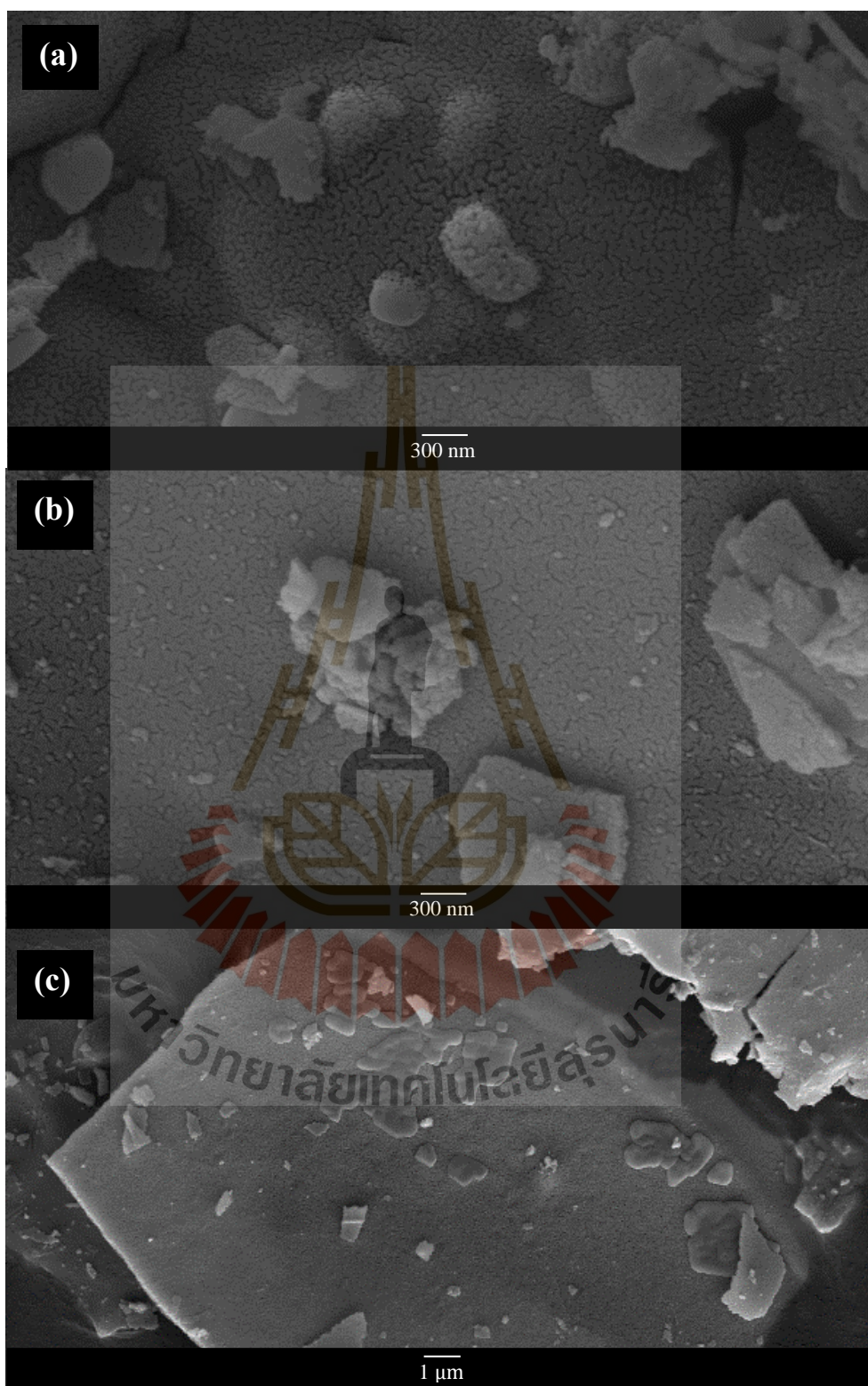


Figure 4.29 SEM images of $\text{Ce}_{1-x}\text{Co}_x\text{O}_2$ ($x = 0.05$ (a), $x = 0.075$ (b), $x = 0.10$ (c)) calcined in air at 600 °C for 2h.

The UV-visible absorption spectra of the pure CeO_2 and Co-doped CeO_2 samples are shown in Figure 4.30. All samples show a strong absorption below 400 nm (3.10eV) with a well-defined absorbance peak at approximately 285 nm (4.35 eV). The band gap can be determined by fitting the absorption data to the direct transition equation by extrapolating of the linear portions of the curves to absorption equal to zero (Figure 4.31(a-d)).

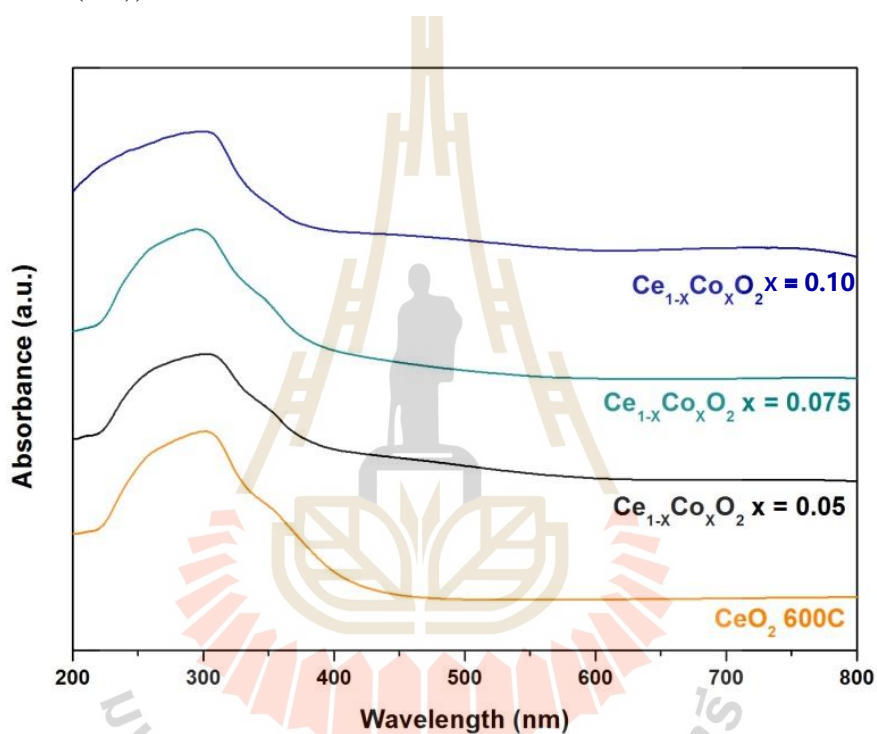


Figure 4.30 Room temperature optical absorbance spectra of CeO_2 and $\text{Ce}_{1-x}\text{Co}_x\text{O}_2$ ($x = 0.05$, $x = 0.075$, $x = 0.10$) samples calcined in air at 600 °C for 2h.

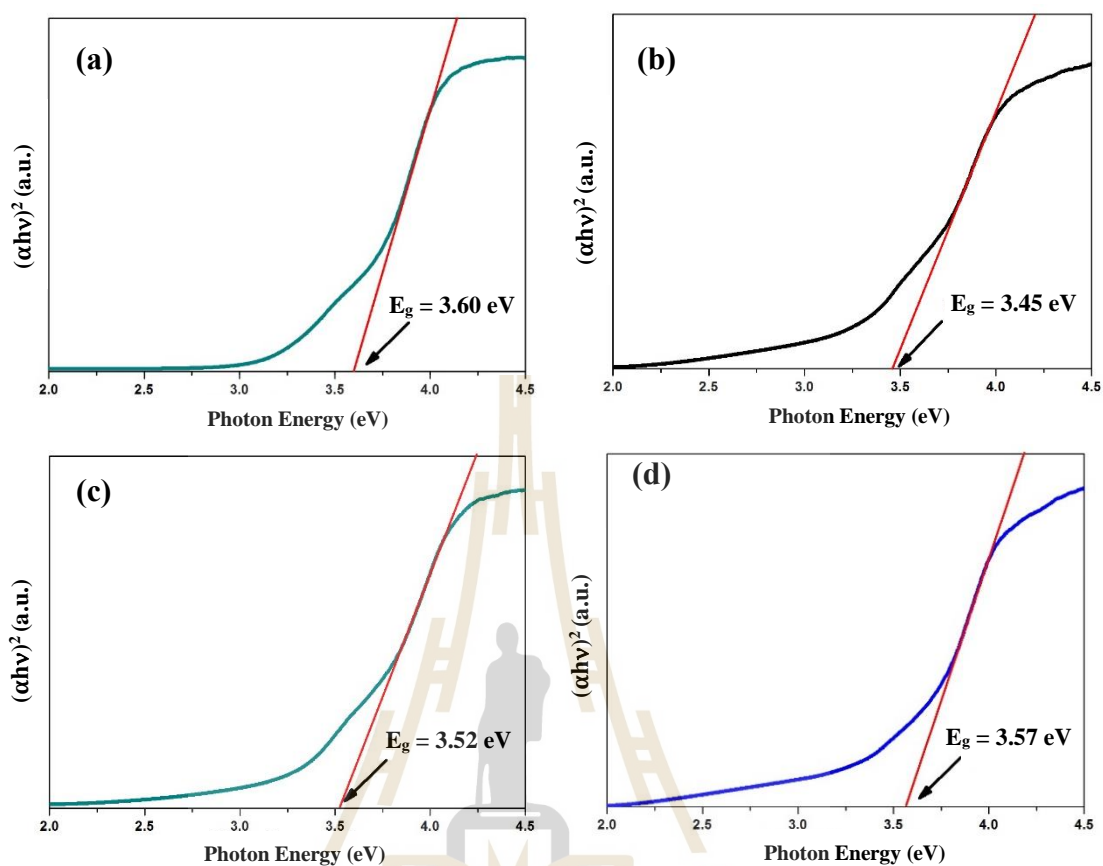


Figure 4.31 The correlated band gaps are 3.60, 3.45, 3.52 and 3.57 eV for the CeO_2 (a) and $\text{Ce}_{1-x}\text{Co}_x\text{O}_2$ ($x = 0.05$ (b), $x = 0.075$ (c), $x = 0.10$ (d)), respectively.

The estimated direct band gaps of all samples are shown in Table 4.13. We have observed that there is an increase in the band gap with increasing Co content calculated for Co-doped CeO_2 prepared at $600\text{ }^\circ\text{C}$ for 2h, which exhibit blue shifts in the absorption spectra. The band gap energy, E_g shows blue shifts of 3.45, 3.52 and 3.57 eV for samples with Co content 0.05, 0.075 and 0.10, respectively, compared with the pure CeO_2 nanoparticles.

In our work, since the crystallite size is in the range of 12.7 - 23.0 nm, the difference of the absorption band edge due to the quantum size effect is not observable.

Obviously, the surface and interface effect should be responsible for the variation of the absorption band edge. Similar results have been obtained in some other systems. Chen and Chang (2005) have reported direct band gap values ranging from 3.56 to 3.71 eV for CeO₂ nanoparticles synthesized by precipitation method. Maensiri et al. (2007) have reported direct band gap values ranging from 3.57 to 3.61 eV for CeO₂ nanoparticles synthesized by sol-gel method using egg white, due to the quantum size effect (Tsunekawa et al., 2003). This behavior is interesting for the CeO₂-based nanospherical materials for efficient application in semiconductor devices.

The valence state of Ce ions in undoped CeO₂ and Co-doped CeO₂ nanoparticles and valence state of Mn ions were determined by XANES. The XANES spectra at Ce L₃ edge were measured in transmission mode, and the Co K edge XANES spectra of the samples were measured in fluorescent mode at BL5.2 station. Figure 4.32 shows the edge energies of the CeO₂ (Ce⁴⁺) standard, pure CeO₂ sample and Co-doped CeO₂ comparison. The edge energies are found at 5727.21, 5727.3, 5727.8 and 5727.39 eV for pure CeO₂ sample and Co-doped with content 0.05, 0.075 and 0.10, respectively. This result indicated that the valence state of Ce ions in our samples consist of Ce³⁺ and Ce⁴⁺ ions. The mixed percentage between Ce(NO₃)₃ and CeO₂ phase in samples were calculated by linear combination fitting of Athena program as shown in Figure 4.33-4.35 and Table 4.14. The percentages of Ce³⁺ and Ce⁴⁺ ions in samples could be calculated from Eq. 4.3, 4.4 and 4.5, respectively. From these results, we can obtain the valence state of Ce atoms according to the edge energy shift position as shown in Table 4.15.

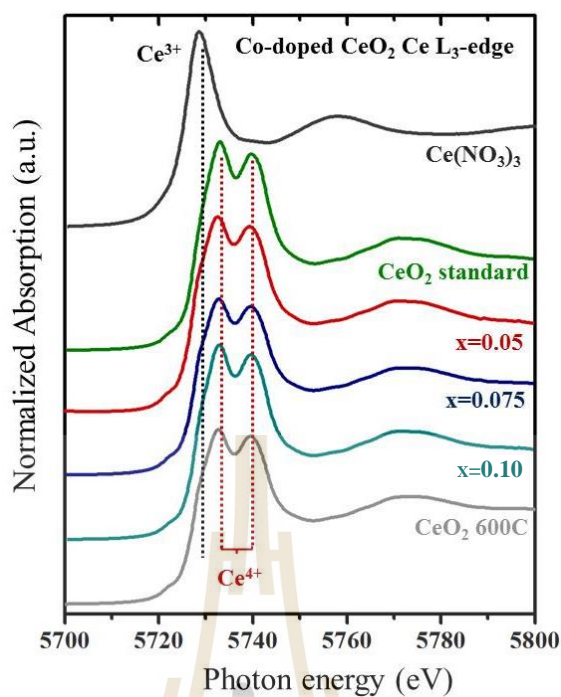


Figure 4.32 XANES spectra at Ce L₃ absorption edge for CeO₂, Cerium nitrate standard and XANES spectra of CeO₂, Co-doped CeO₂ nanoparticles samples.

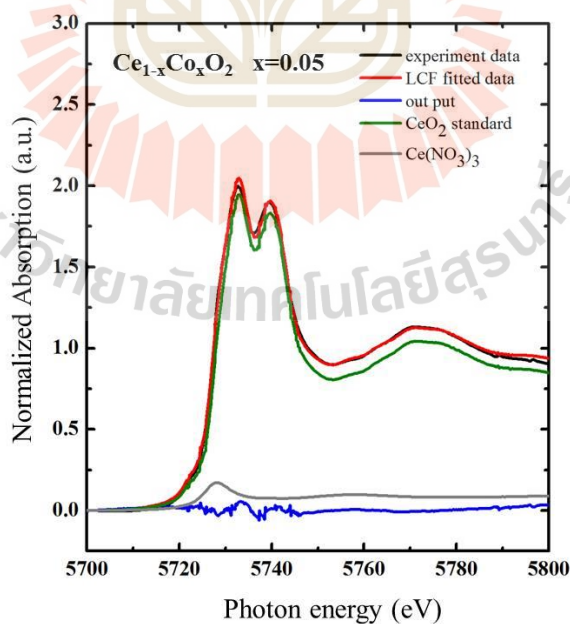


Figure 4.33 XANES spectra and linear combination fit of Co-doped CeO₂ x = 0.05, Ce(NO₃)₃/CeO₂ standard.

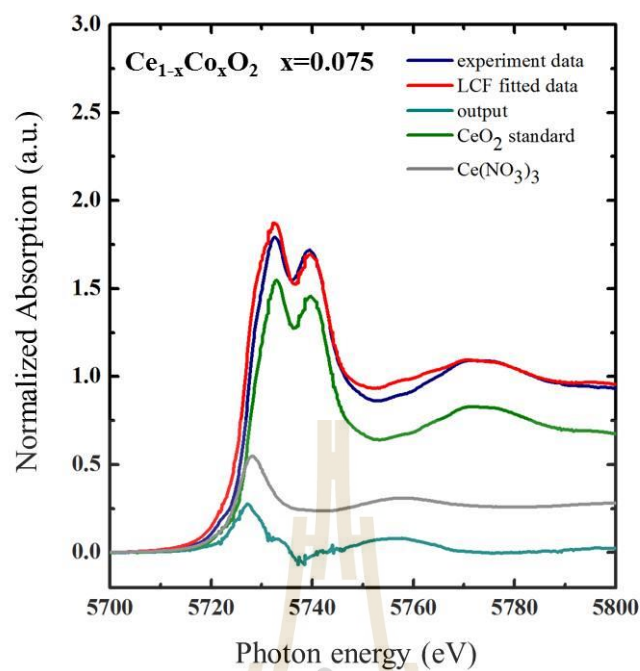


Figure 4.34 XANES spectra and linear combination fit of Co-doped CeO_2 $x = 0.075$, $\text{Ce}(\text{NO}_3)_3/\text{CeO}_2$ standard.

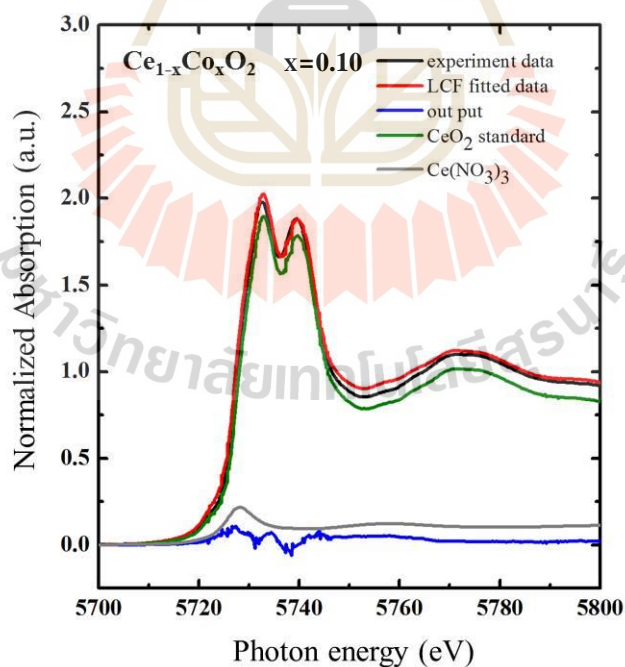


Figure 4.35 XANES spectra and linear combination fit of Co-doped CeO_2 $x = 0.10$, $\text{Ce}(\text{NO}_3)_3/\text{CeO}_2$ standard.

Table 4.14 The mixed percentage between $\text{Ce}(\text{NO}_3)_3$ and CeO_2 standard of Co-doped CeO_2 samples were calculated by linear combination fitting of Athena program.

Samples $\text{Ce}_{1-x}\text{Co}_x\text{O}_2$	Peak position (eV)	Percentage of $\text{Ce}(\text{NO}_3)_3$	Percentage of CeO_2	R factor values
x = 0.00	5727.21	15.2 %	84.8 %	0.0149
x = 0.05	5727.3	1.4 %	98.6 %	0.005
x = 0.075	5727.8	10.3 %	89.7 %	0.002
x = 0.10	5727.39	2.2 %	97.8 %	0.003

Table 4.15 Calculated valence state of Ce according to the edge energy shift positions of Co-doped CeO_2 samples.

Samples $\text{Ce}_{1-x}\text{Co}_x\text{O}_2$	Peak position (eV)	ΔE of sample (eV)	Ce oxidation state	Percentage of Ce^{3+}	Percentage of Ce^{4+}
x = 0.00	5727.3	2.74	3.94	4.8 %	95.2 %
x = 0.05	5727.21	2.88	3.97	3.7 %	96.3 %
x = 0.075	5727.8	2.96	3.99	1.1 %	98.9 %
x = 0.10	5727.39	2.54	3.92	5.4 %	94.6 %

It is observed that the highest percentage of Ce^{3+} is 5.4% for Co-doped CeO_2 sample with content 0.10.

Figure 4.36 shows the edge energies of Co_3O_4 (Co^{2+} and Co^{3+}) standard, $\text{Co}(\text{NO}_3)_2$ (Co^{2+}) standard Co-doped CeO_2 samples at different concentrations for comparison. The edge energies imply a coupling of Co_3O_4 and $\text{Co}(\text{NO}_3)_2$ in samples. The mixed percentage between Co_3O_4 and $\text{Co}(\text{NO}_3)_2$ of samples were calculated by linear combination fitting of Athena program (Figure 4.37 - 4.39) are also shown in Table 4.16. Similarly, with the Eqs. 4.3, 4.4 and 4.5, we could be calculated the percentages of Co^{2+} and Co^{3+} of samples. From these results, we can obtain the mixed valence states of Co atoms and edge energy values are also shown in Table 4.17.

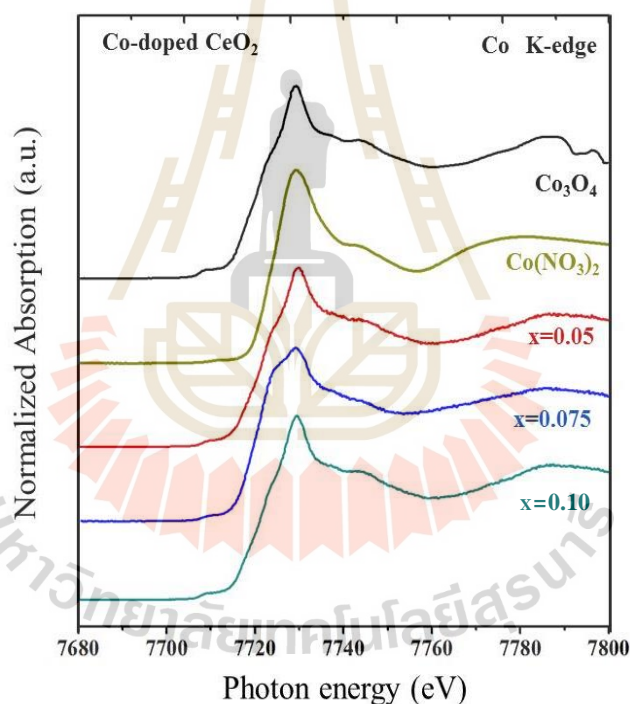


Figure 4.36 XANES spectra at Co K absorption edge for Co_3O_4 , $\text{Co}(\text{NO}_3)_2$ standard and XANES spectra of Co-doped CeO_2 nanoparticles samples.

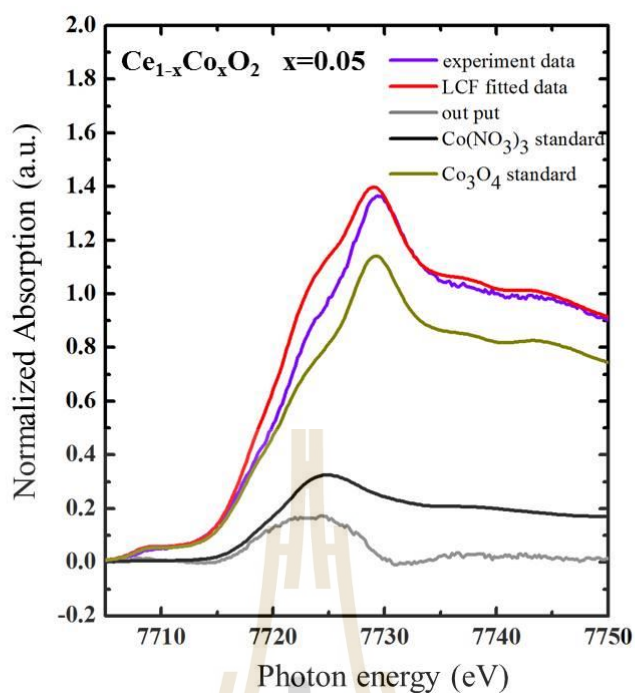


Figure 4.37 XANES spectra and linear combination fit of Co-doped CeO_2 $x = 0.05$, $\text{Co}_3\text{O}_4/\text{Co}(\text{NO}_3)_2$, reference metal and compound at K-edge.

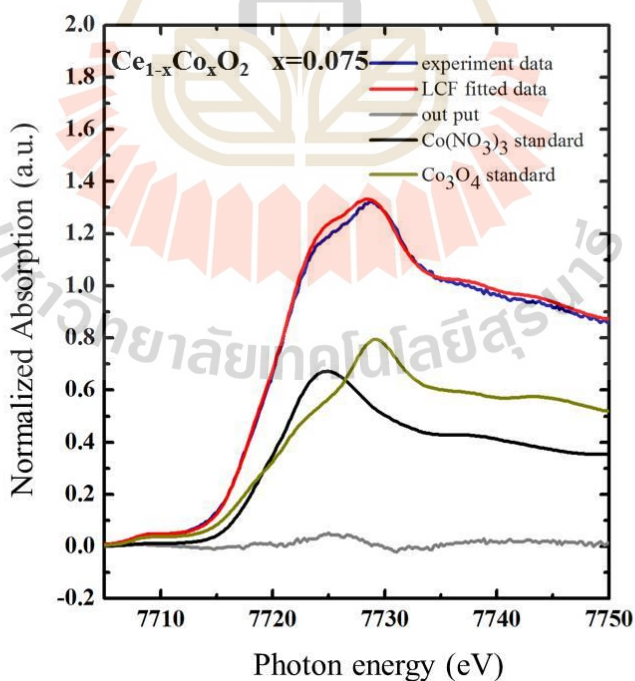


Figure 4.38 XANES spectra and linear combination fit of Co-doped CeO_2 $x = 0.075$, $\text{Co}_3\text{O}_4/\text{Co}(\text{NO}_3)_2$, reference metal and compound at K-edge.

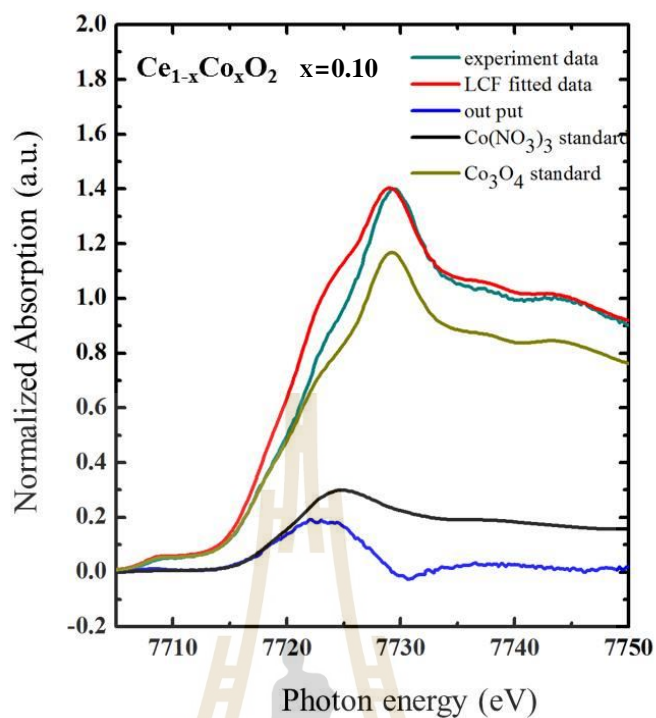


Figure 4.39 XANES spectra and linear combination fit of Co-doped CeO_2 $x = 0.10$, $\text{Co}_3\text{O}_4/\text{Co}(\text{NO}_3)_2$, reference metal and compound at K-edge.

Table 4.16 The mixed percentage between Co_3O_4 and $\text{Co}(\text{NO}_3)_2$ of Co-doped CeO_2 samples were calculated by linear combination fitting of Athena program.

Samples	Peak position (eV)	Percentage of Co_3O_4	Percentage of $\text{Co}(\text{NO}_3)_2$	R factor values
$x = 0.05$	7721.5	69.2 %	31.8 %	0.003
$x = 0.075$	7720.1	50.8 %	49.2 %	0.007
$x = 0.10$	7721.7	62.8 %	31.2 %	0.009

Table 4.17 Calculated valence state of Co according to the edge energy shift positions of Co-doped CeO₂ samples.

Samples	Peak	ΔE of	Co	Percentage	Percentage
Ce _{1-x} Co _x O ₂	position	sample	oxidation	of Co ²⁺	of Co ³⁺
	(eV)	(eV)	state		
x = 0.05	7721.5	3.40	3.24	56.5 %	43.5 %
x = 0.075	7720.1	3.48	3.78	73.9 %	26.1 %
x = 0.10	7721.7	3.20	3.04	61.4 %	38.6 %

The highest percentage of Co²⁺ are approximate 73.9 % in Co-doped CeO₂ with content 0.075.

4.3.2 Magnetic properties of Co-doped CeO₂ nanoparticles

Magnetic behavior of Co-doped CeO₂ nanoparticles has been studied using FC magnetization and magnetic hysteresis loop measurements. Figure 4.40 shows typical magnetization (M) versus field curves of Co-doped CeO₂ with different concentration nanoparticles measured at RT. The samples that were prepared with different content 0.05, 0.075 and 0.10. Samples Ce_{1-x}Co_xO₂ with content x = 0.05, x = 0.10 are shown diamagnetism, whereas sample Ce_{1-x}Co_xO₂ with content x = 0.075 is shown weak ferromagnetism and paramagnetism with magnetization value (M) of approximately 0.00015 emu/g, respectively (as listed in Table 4.18).

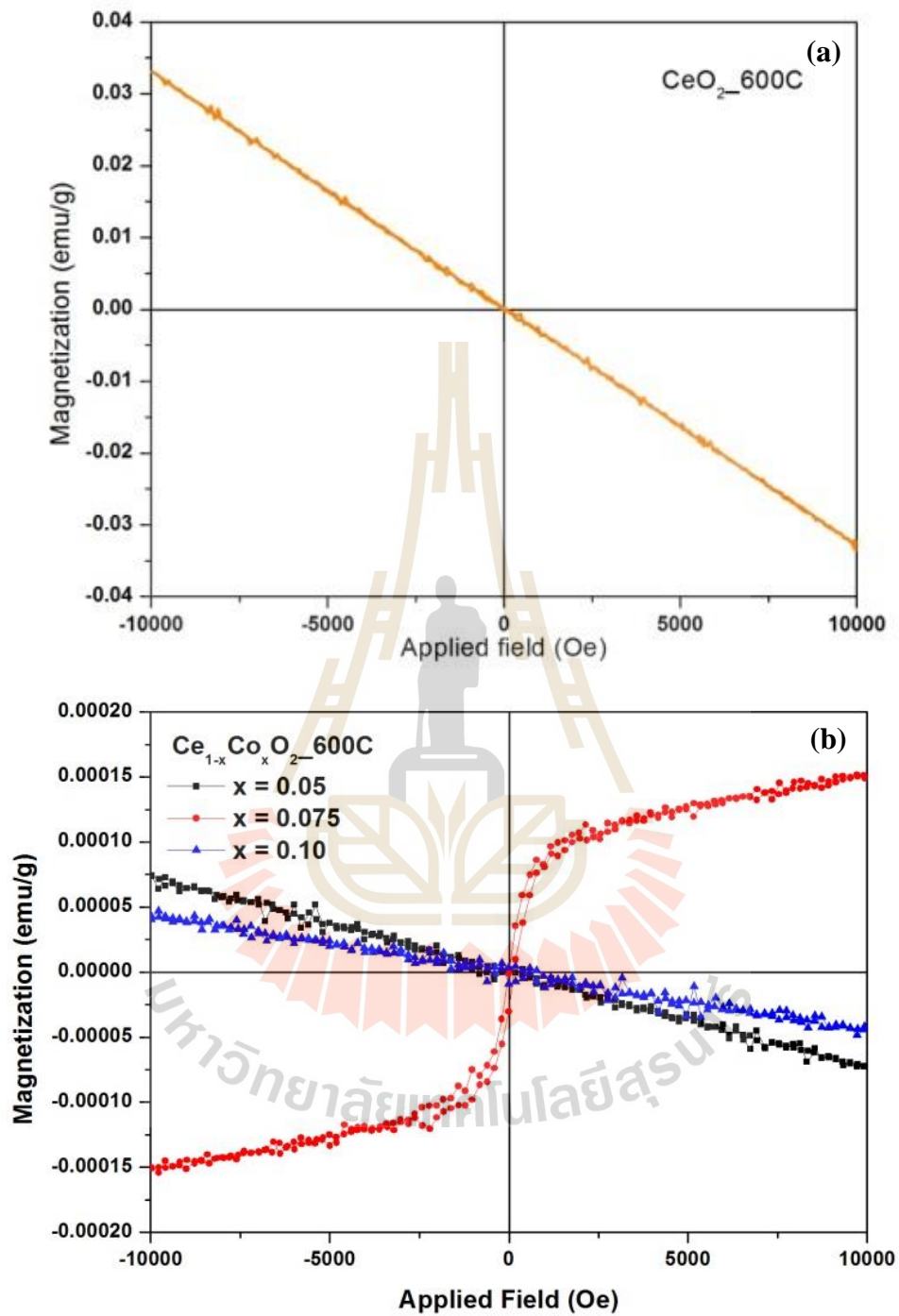


Figure 4.40 Magnetic properties of CeO_2 (a) and Co-doped CeO_2 (b) nanoparticles calcined at various temperatures for 2h in air at 600 °C.

Table 4.18 Summary of magnetization (M) of CeO₂ and Co-doped CeO₂ nanoparticles calcined at 600 °C for 2h.

Samples	M_s at 10 kOe (emu/g)
Ce_{1-x}Co_xO₂	
CeO ₂	diamagnetic
x = 0.05	diamagnetic
x = 0.075	0.00015
x = 0.10	diamagnetic

Samples Ce_{1-x}Co_xO₂ with content x = 0.05, x = 0.10 exhibited diamagnetism. It is possible that of the electrons of ionic charge Ce⁴⁺ are allied together to f⁰ induce net magnetic moment in the opposite direction to the external magnetic field. Therefore, the diamagnetic out. Sample Ce_{1-x}Co_xO₂ with content x = 0.075 exhibit weak ferromagnetism and paramagnetism with magnetization value (M) of approximately 0.00015 emu/g possibly due to the replacement of larger Ce⁴⁺ ions by smaller Co²⁺ ions (73.9 %, confirm by XANES). The calcination with high temperature (600 °C) could possibly increase the number of oxygen vacancies and Ce³⁺ ions in the samples. The magnetic properties were also performed to confirm the effect of oxygen vacancies. The observed ferromagnetism can be explained by FCE (Coey, 2005; Paula et al., 2010; Patterson et al., 2005; Pearton et al., 2003). The XANES spectra show the evidence of Co²⁺ ions substitution in CeO₂, and the Ce ions of 3+ state (with 4f¹ configuration), which can be attributed to V_O in Co-doped CeO₂ samples. Therefore, the ferromagnetic in these samples was suggested according to the FCE of Co²⁺-V_O-Co²⁺ (see in Figure 4.41) complex in the structure.

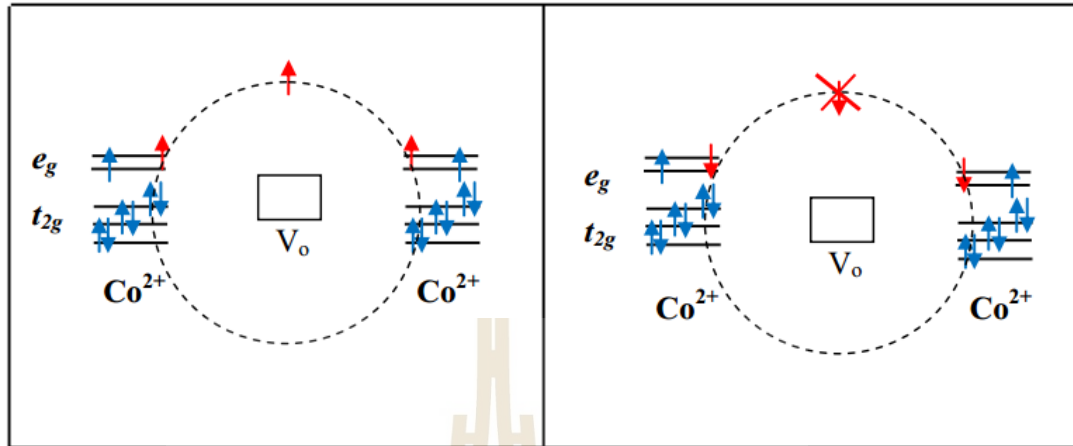


Figure 4.41 A schematic energy level diagram for a ferromagnetic coupling between Two Co ions via a donor electron trapped in the oxygen vacancy (Reproduced from Patterson, 2005).

This FCE forms BMP and neighboring BMPs can overlap and result in the long-rang Co-Co ferromagnetic coupling in CeO₂. Moreover, we believe that the origin of ferromagnetism in Co-doped CeO₂ nanoparticles is due to Co²⁺ ions substitution in CeO₂ and oxygen vacancies.

CHAPTER V

CONCLUSION AND SUGGESTIONS

5.1 Conclusion

The CeO_2 and $\text{Ce}_{1-x}\text{TM}_x\text{O}_2$ (TM = Mn, Co) nanostructures have been successfully prepared by egg white solution route. The XRD and SEAD results indicate that all the samples have a face-centered cubic structure, and 4 secondary phase were detected, indicating that TM ions were substituted in Ce^{4+} sites. The average crystallite sizes were obtained to be (10.0 ± 3.2) to (35.4 ± 2.8) nm. The lattice constants did change with the concentration of the dopants except for TM doped as observed on XRD result. The morphology of the samples shown thin platelike clusters of nanoparticles with particle size of ~ 5 -60 nm, which were built from small nanoparticles as investigated by TEM, HRTEM and SEM results. UV-vis spectra shown a blueshift of band gap energy that originates from defects/oxygen vacancy caused by TM substitution. The TM substitution was confirmed by XANES measurements, which revealed that most of the TM ions were in the Mn^{2+} , Mn^{3+} , Mn^{4+} , Co^{2+} , and Co^{3+} state, and mixed valence state of Ce^{3+} and Ce^{4+} . This Ce^{3+} and TM spin electrons induced weak ferromagnetic and strong paramagnetic component at higher field. The highest of M_S was 0.00035, and 0.00015 emu/g for Mn ($x = 0.10$) and Co ($x = 0.075$) doped CeO_2 nanoparticles, respectively, obtained from VSM measurements at 10 kOe. The ferromagnetism due to effect of TM (Mn, Co) doping and oxygen vacancy. The smaller

magnetization observed in particles of Mn, Co-doped CeO₂ were investigated by the effect of size as compared to nanoparticles observed in the recent literatures.

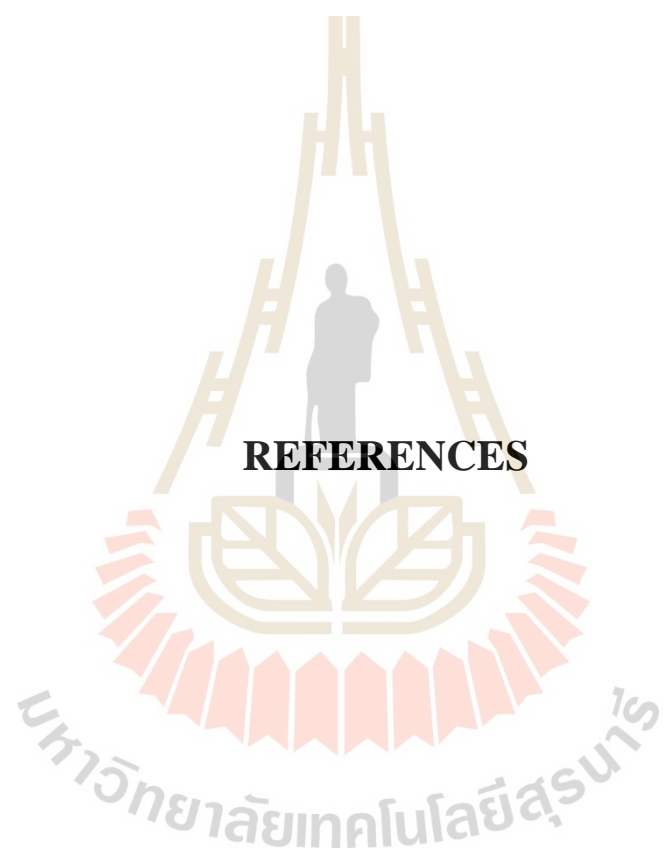
Finally, the nature of RT-FM in TM-doped CeO₂ samples were observed in both magnetic and nonmagnetic ions doping that depended on the oxygen vacancies based on *F*-center exchange interaction. Its properties can apply with new devices in electronic technology.

5.2 Suggestions for future work

The findings in this research suggest the future works as follows:

- (i) Investigation of the stoichiometry of Ce_{1-x}TM_xO₂ (TM = Mn and Co) using Energy Dispersive Spectroscopy (EDS) is required to confirm the fraction of constituent elements of Ce, O, Mn and Co ions in the prepared samples.
- (ii) Local structures using EXAFS are important to confirm the substitution of dopants in ferromagnetic metal-doped CeO₂ system.

Because of their interesting properties of Mn and Co-doped CeO₂ such as nanostructures, surface area and defect in structure, these Mn and Co-doped CeO₂ nanostructures appear to be promising active materials for supercapacitive, thermoelectric and photocatalytic applications in the future.



REFERENCES

REFERENCES

- Akdogan, N., Nefedov, A., Westphalen, A., Zabel, H., Khaibullin, R. I., and Tagirov, L. R. (2007). Dose dependence of magnetism in Co-doped TiO₂. **Superlattices and Microstructures**. (41): 132-137.
- Barreca, D., Bruno, G., Gasparotto, A., Losurdo, M., and Tondello, E. (2003). Nanostructure and optical properties of CeO₂ thin films obtained by plasma-enhanced chemical vapor deposition. **Materials Science and Engineering: C**. (23): 1013-1016.
- Coey, J. M. D. (2005). High-temperature ferromagnetism in dilute magnetic oxides. **Journal of Applied Physics**. (97): 10D313.
- Coey, J. M. D., Venkatesan, M., and Fitzgerald, C. B. (2005). Donor impurity band exchange in dilute ferromagnetic oxides. **Nature Materials**. 4(2): 173-179.
- Coey, J. M. D. (2006). Dilute magnetic oxides. **Current Opinion in Solid State and Materials Science**. 10: 83.
- Chu, X., Chung, W., and Schmidt, L. D. (1993). Sintering of Sol-Gel Prepared Submicrometer Particles Studied by Transmission Electron Microscopy. **Journal of the American Ceramic Society**. (76): 2115-2118.
- Chen, S.Y., Lu Y. H., Huang, T. W., Yan, D. C., and Dong, C. L. (2010). Oxygen vacancy dependent magnetism of CeO₂ nanoparticles prepared by thermal decomposition method. **The Journal of Physical Chemistry C**. 114: 19576-19581.

- Dietl, T., Ohno, H., Matsukura, F., Cibert, J., and Ferrand, D. (2000). Zener Model Description of Ferromagnetism in Zinc-Blende Magnetic Semiconductors. **Science**. (287): 1019-1022.
- Fernandes, V., Klein, J. J., Mattoso, N., Mosca, D. H., Silveira, E., Ribeiro, E., Schreiner, W. H., Varalda, J., and de Oliveira, A. J. A. (2007). Room temperature ferromagnetism in Co-doped CeO₂ films on Si (001). **Physical Review B**. 75: 121304R.
- Ge, M. Y., Wang, H., Liu, E. Z., Liu, J. F., Jiang, J. Z., Li, Y. K., Xu, Z. A., and Li, H. Y. (2008). On the origin of ferromagnetism in CeO₂ nanocubes. **Applied Physics Letters**. 93: 062505.
- Hayashi, T., Tanaka, M., Seto, K., Nishinaga, T., and Ando, K. (1997). III–V based magnetic(GaMnAs)/nonmagnetic(AlAs) semiconductor superlattices. **Applied Physics Letters**. (71): 1825.
- Kim, D. H., Yang, J. S., Lee, K. W., Bu, S. D., and Noh, T. W. (2002). Formation of Co nanoclusters in epitaxial Ti_{0.96}Co_{0.04}O₂ thin films and their ferromagnetism. **Applied Physics Letters**. (81): 2421.
- Liu, C., Yun, F., and Morkoc, H. (2005). Ferromagnetism of ZnO and GaN: A Review. **Journal of Materials Science: Materials in Electronics**. (16): 555-597.
- Liu, Y., Lockman, Z., Aziz, A., and Macmanus, D. J. (2008). Size dependent ferromagnetism in cerium oxide (CeO₂) nanostructures independent of oxygen vacancies. **Journal of Physics: Condensed Matter**. 20: 165201.

- Matsumoto, Y., Murakami, M., Shono, T., Hasegawa, T., Fukumura, T., Kawasaki, M., Ahmet, P., Chikyow, T., Koshihara, Sh., and Koinuma, H. (2001). Room-temperature ferromagnetism in transparent transition metal- doped titanium dioxide. **Science**. (291): 854-856.
- Maensiri, S., Masingboon, C., Laokul, P., and Jareonboon, W. (2007). Egg white synthesis and photoluminescence of platelike clusters of CeO₂ nanoparticles. **Crystal Growth and Design**. (7): 950-955.
- Maensiri, S., Phokha, S., Laokul, P., and Seraphin, S. (2009). Room temperature ferromagnetism in Fe-doped CeO₂ nanoparticles. **Journal of Nanoscience and Nanotechnology**. 9: 6415-6420.
- Munekata, H., Ohno, H., von Molnar, S., Segmuller, A., Chang, L. L., and Esaki, L. (1989). Diluted magnetic III-V semiconductors. **Physical Review Letters**. (63): 1849-1852.
- Nagai, Y., Kurimoto, T., Nagasaka, K., Nojiri, H., Motokawa, M., Matsukura, F., Dietl, T., and Ohno, H. (2001). Spin Polarization Dependent Far Infrared Absorption in Ga_{1-x}Mn_xAs. **Japanese Journal of Applied Physics**. (40): 6231-6234.
- Ohno, H., Shen, A., Matsukura, F., Oiwa, A., Endo, A., Katsumoto, S., and Iye, y. (1996). (Ga,Mn)As: A new diluted magnetic semiconductor based on GaAs. **Applied Physics Letters**. (69): 363.
- Ohno, H. (1998). Making nonmagnetic semiconductors ferromagnetic. **Science**. (281): 951-6.

- Ohno, H. (2000). Ferromagnetic III–V heterostructures. **Journal of Vacuum Science and Technology B**. (18): 2039-2043.
- Ohno, H., Matsukura, F., and Ohno, Y. (2002). General Report : Semiconductor Spin Electronics. **Japan Society of Applied Physics International**. (5): 4.
- Oiwa, A., Slupinski, T., and Munekata, H. (2001). Control of magnetization reversal process by light illumination in ferromagnetic semiconductor heterostructure p-(In,Mn)As/GaSb. **Applied Physics Letters**. (78): 518-520.
- Ou, Y. N., Li, G. R., Liang, J. H., Feng, Z. P., and Tong, Y. X. (2010). Ce_{1-x}Co_xO_{2-δ} nanorods grown by electrochemical deposition and their magnetic properties. **The Journal of Physical Chemistry C**. 114: 13509-13514.
- Paula, C. A. B., Daniel, A. A. S., Jose, G. S. D., and Marcelo, A. M. (2010). Structural and magnetic study of Fe-doped CeO₂. **Physica B**. 405: 1821-1825.
- Patterson, C. H. (2005). Magnetic defects promote ferromagnetism in Zn_{1-x}Co_xO. **Journal of Physics : Condensed Matter**. (1): 0512101.
- Pearton, S. J., Abernathy, C. R., Norton, D. P., Hebart, A. F., Park, Y. D., Boatner, L. A., and Budai, J. D. (2003). Advances in wide band gap materials for semiconductor spintronics. **Materials Science and Engineering**. (R40): 137-168.
- Pearton, S. J., Heo, W. H., Ivill, M., Norton, D. P., and Steiner, T. (2004). Dilute magnetic semiconducting oxides. **Semiconductor Science and Technology**. 19: R59.

- Phokha, S. (2008). Dilute magnetic oxide of CeO₂-based nanoparticles: synthesis, characterization and magnetic properties. Master of Science Thesis Program in Physics, Faculty of Science, Khon Kaen University.
- Prellier, W., Fouchet, A., and Mercey, B. (2003). Oxide-diluted magnetic semiconductors: a review of the experimental status. **Journal of Physics: Condensed Matter**. 15: R1583.
- Ramachandran, S., Tiwari, A., and Narayan, J. (2004). Zn_{0.9}Co_{0.1}O-based diluted magnetic semiconducting thin films. **Applied Physics Letters**. (84): 5255-5257.
- Rameev, B. Z., Yildiz, F., Tagirov, L. R., Aktas, B., Park, W. K., and Moodera, J. S. (2003). ESR study of Co-doped TiO₂ thin films. **Journal of Magnetism and Magnetic Materials**. (258): 361-364.
- Sato, K., and Katayama-Yoshida, H. (2000). Material Design for Transparent Ferromagnets with ZnO-Based Magnetic Semiconductors. **Japanese Journal of Applied Physics**. (39): L555-L558.
- Song, Y. Q., Zhang, H. W., Wen, Q. Y., Li, Y. X., and Xiao, J. Q. (2007). Room-temperature ferromagnetism of Co-doped CeO₂ thin films on Si(111) substrates. **Chinese Physics Letters**. 24: 218.
- Thurber, A., Reddy, K. M., Shutthanandan, V., Engelhard, M. H., Wang, C., Hays, J., and Punnoose, A. (2007). Ferromagnetism in chemically synthesized CeO₂ nanoparticles by Ni doping. **Physical Review B**. 76: 165206.
- Tiwari, A., Bhosle, V. M., Ramachandran, S., Sudhakar, N., Narayan, J., Budak, S., and Gupta, A. (2006). Ferromagnetism in Co doped CeO₂: observation of a

- giant magnetic moment with a high Curie temperature. **Applied Physics Letters**. 88: 142511.
- Ueda, K., Tabata, H., and Kawai, T. (2001). Magnetic and electric properties of transition-metal doped ZnO films. **Applied Physics Letters**. (79): 988-990.
- Vodungbo, B., Zheng, Y., Vidal, F., Demaille, D., Etgens, V. H., and Mosca, D. H. (2007). Room temperature ferromagnetism of Co doped $\text{CeO}_{2-\delta}$ diluted magnetic oxide: Effect of oxygen and anisotropy. **Applied Physics Letters**. 90: 062510.
- Wang, C. M., Shutthanandan, V., Thevuthasan, S., Droubay, T., and Chambers, S. A. (2005). Microstructure of Co-doped TiO_2 (110) rutile by ion implantation. **Journal of Applied Physics**. (97): 073502.
- Wen, Q. Y., Zhang, H. W., Song, Y. Q., Yang, Q. H., Zhu, H., and Xiao, J. Q. (2007). Room-temperature ferromagnetism in pure and Co doped CeO_2 powders. **Journal of Physics: Condensed Matter**. 19: 246205.
- Zhang, J., Li, X. Z., Lu, Y. F., and Sellmyer, D. J. (2007). Structure and magnetic properties of Mn-doped ZnO thin films. **Journal of Physics : Condensed Matter**. (19): 036210.

CURRICULUM VITAE

Name Panwit Sangkhaoartyon

Date of Birth 9 November 1990

Place of Birth Sisaket, Thailand

Education

10 April 2013 Mahasarakham University, Mahasarakham, Thailand. Bachelor of Science (Physics)

MSc. Thesis:

Structure and magnetic properties of CeO_2 and $\text{Ce}_{1-x}\text{TM}_x\text{O}_2$ (TM = Mn and Co) nanostructures prepared by egg-white solution route.

Conferences:

Sangkhaoartyon, P., Pinitsoontorn, S., Maensiri, S. Structure and magnetic properties of Co-doped CeO_2 nanostructures prepared by egg-white solution route. The First Materials Research Society of Thailand International Conference (1st MRS Thailand International Conference), **October 31 – November 3, 2017**, The Empress Convention Center, Chiangmai, Thailand.

Academic Experience:

Teaching Assistant at Laboratory, School of Physics, Suranaree University of Technology, Thailand.